FERMILAB-THESIS-2022-14

The Dissertation Committee for Beatriz Tapia Oregui
certifies that this is the approved version of the following dissertation:

Towards a Measurement of Neutral Pion Production in Neutral Current Interactions with the NOνA Near Detector

Committee:

Karol Lang, Supervisor

Jack Ritchie

Tim Andeen

Pawan Kumar

Towards a Measurement of Neutral Pion Production in Neutral Current Interactions with the NOνA Near Detector

by

Beatriz Tapia Oregui

DISSERTATION

Presented to the Faculty of the Graduate School of

The University of Texas at Austin

in Partial Fulfillment

of the Requirements

for the Degree of

DOCTOR OF PHILOSOPHY

THE UNIVERSITY OF TEXAS AT AUSTIN

August 2022

Dedicated to my family and friends.

Acknowledgments

My PhD has been an adventure through the experimental physics jungle, the Texas desert, and the roller coaster of 6 years in "America, Fievel!"[1]. First and foremost, this journey would not have started, if it wasn't for my husband, who suggested applying to PhD programs in the US. I am grateful to Sebastian not just for being by my side, but for helping and supporting me every step of the way. My family has been a constant source of inspiration to fight for my dreams and Freud knows what. My friends, scattered throughout Spain, Germany and the US, have always been there for me, helped me laugh it off and been able to deal with the ensuing, characteristic sound waves.

I am indebted to my advisor, Karol Lang, who taught me how to do and enjoy research. His temper and passion for physics reminded me of my Spanish roots, while his knowledge and resilience lightened my darkest hours. The many members of his research group (UTKL) have been an immense source of joy, wisdom and support without which I would have never been able to accomplish this endeavor. Finally, I am extremely thankful to my NOνA collaborators: mentors, colleagues and friends, for their help, time and patience.

[1] Just like the mice in Steven Spielberg's "An American Tail", I also came to the promised land, met despair, and found a new home.

Towards a Measurement of Neutral Pion Production in Neutral Current Interactions with the NOνA Near Detector

Publication No. _____

Beatriz Tapia Oregui, Ph.D.
The University of Texas at Austin, 2022

Supervisor: Karol Lang

This dissertation reports the steps towards a cross-section measurement of the neutral-current producing at least one neutral pion above detection threshold in the NOvA near detector. Neutral pions decay into two photons 99% of the time, so the signature for this analysis is two electromagnetic showers slightly away from the vertex. This neutrino cross-section measurement is very important in the context of electron neutrino appearance, since one or both of the two gammas can mistakenly be reconstructed as an electron.

The event selection requires two fully contained reconstructed showers with a minimum number of hits, whose reconstructed vertex is within the fiducial volume. To reduce the charged-current background with a muon in the final state, the analysis includes a cut on a muon identifier (trained on simulated single particles). Several reconstructed variables like the invariant

mass, widths and distances between the vertex and the start of the showers are fed to a boosted decision tree (BDT), which also contains an electromagnetic shower identifier.

The plan is to perform a fit to data for each bin within the phase-space grid, such that signal and background templates vary in normalization. A BDT event classifier output is the distribution chosen for the fit and templates. Signal and background templates predicted from simulation help extract the actual signal component for data in several π^0 kinematic bins of reconstructed energy and angle with respect to the beam direction. This template fit should account for bin-to-bin correlations of systematic uncertainties via a covariance matrix. The final result is the amount of simulated events for the phase-space proposed binning, which accounts for a total of 8,970 events.

Table of Contents

List of Tables

List of Figures

Chapter 1

Introduction

Neutrinos are elusive, very light elementary particles that surround us in our everyday life. As one of the most abundant particles in the Universe, 65 billion neutrinos coming from nuclear reactions inside the Sun traverse the small surface of a human thumb every second. For more than a century physicists have tried to better understand their oscillatory behavior, interactions, mass origin and nature. Even though advancements have been achieved, there are still mysteries to be solved. In this chapter the current knowledge is summarized [1, 2], and several experiments that contribute to answering some of the open questions are introduced [3].

1.1 The Discovery and History of the Neutrino

In the early 19th century physicists noticed puzzling behavior of the electrons measured from beta decays

$$ {}^{A}_{Z}X \rightarrow {}^{A-1}_{Z+1}X' + e^{-}, $$

where a neutron inside the nucleus decays into a proton by emitting an electron. The differences in nuclear masses, Q, would be the energy carried away by the electron. Nevertheless, the measured spectrum of electrons is instead a

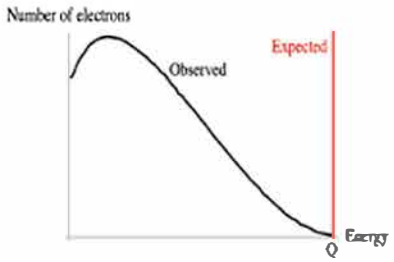

Figure 1.1: Electron spectrum of β-decay from [4].

continuum with an end-point at Q, see fig 1.1. Physicists were so baffled about this conundrum that they were even considering giving up on the principle of energy conservation.

It was not until the year 1930 that a solution was found, when the Austrian physicist Wolfgang Pauli wrote a letter [5] proposing a *desperate remedy*: in the β-decay, a neutral and relatively light spin 1/2 particle was being emitted together with the electron and escaped undetected carrying away the missing energy. The proposition of this new particle, initially called *neutron*, was at the time revolutionary, and the physics community was not too fond of it. Enrico Fermi, though, took it seriously, incorporated it into his beta decay theory [6], and renamed it *neutrino* (funny Italian diminutive of *neutral one*) since the now known neutron (a neutral particle very close in mass to the proton) had recently been discovered [7].

In 1956 Frederick Reines and Clyde Cowan detected the neutrino for the first time [8] using the anti-neutrino flux from the fission reactor at the Savanah River Plant of the United States Atomic Energy Commission. Cowan and Reines measured anti-electron-neutrinos interacting with protons in half

a cubic meter of water,

$$\bar{\nu}_e + p \rightarrow e^+ + n.$$

The first pulse was two coincident, back-to-back, 511 keV photons originating from the annihilation of the outcoming positron with an electron from the liquid scintillator. The second pulse was delayed and came from the capture of the slow neutron by the cadmium mixed in the water.

The muon-neutrino was first detected in 1962 using the Alternating Gradient Synchrotron (AGS) particle accelerator at Brookhaven National Laboratory [9]. The 15 GeV proton beam slammed into a fixed beryllium target produced pions, which in flight decayed into muons and neutrinos,

$$\pi^+ \rightarrow \mu^+ + \nu_\mu,$$
$$\pi^- \rightarrow \mu^- + \bar{\nu}_\mu.$$

A steel wall of 13.5 m thickness located after the target stopped all remaining particles except for the rarely interacting neutrinos. These made it to a spark chamber consisting of 90 1-inch-thick aluminum plates separated by gas-filled gaps. Traversing neutrinos would occasionally interact with a proton in an aluminum nucleus producing a neutron and a charged lepton. The charged particle ionized the gas, creating a visible spark track. If the neutrinos were muon neutrinos, they would produce muons while detection of electrons would be correlated with electron neutrino interactions. The characteristic electromagnetic showers of electrons vs the long tracks of muons made it possible to distinguish between them.

The tau-neutrino was detected by the "Direct Observation of Nu Tau" (DONUT) collaboration at the Fermi National Accelerator Laboratory (Fermilab) [10] in the year 2000. The interaction of the 800 GeV proton beam in a meter long tungsten beam dump produced a beam of tau-neutrino from the decay of charmed mesons.

1.2 Neutrinos in the Standard Model

The Standard Model (SM) [11–13] of particle physics unites the strong, weak and electromagnetic forces of nature and their relation with the elementary particles into one quantum field theory. Photons γ are the mediators of the electromagnetic force, gluons g the carriers of the strong force and massive vector bosons W^+, Z the representatives of the weak force, see fig. 1.2, but gravity is not part of this mathematical description.

The Standard Model is a gauge theory based on the group

$$G_{SM} = SU(3)_C \times SU(2)_L \times U(1)_Y. \tag{1.1}$$

In addition, the SM contains a single Higgs boson which is uncharged under the electromagnetic and strong forces, and forms a doublet under $SU(2)_L$. Consequently, its non-zero vacuum expectation value breaks the gauge symmetry:

$$G_{SM} \to SU(3)_C \times U(1)_{EM} =: G'_{SM}. \tag{1.2}$$

Neutrinos are fermions that have neither strong nor electromagnetic interactions and therefore are singlets under the symmetry group G'_{SM}. The La-

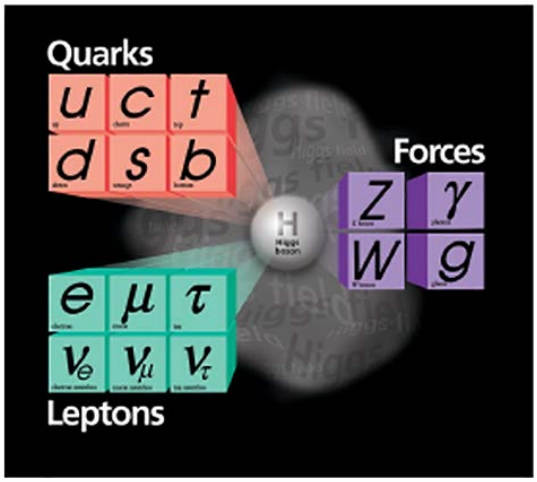

Figure 1.2: The SM contains fermions, which are spin 1/2 particles subcategorized into leptons and quarks, and bosons, which are spin 1 particles and force carriers. The Higgs particle has not intrinsic spin and couples to all the massive particles giving them mass.

grangian of the SM contains two terms describing all possible neutrino interactions: the charged current (CC):

$$\mathcal{L}_{CC} = \frac{-g}{\sqrt{2}} j^{\mu}_{CC} W_{\mu} + h.c. \quad \text{with} \quad j^{\mu}_{CC} = \bar{f}_{\alpha} \gamma^{\mu} P_L f'_{\alpha}, \tag{1.3}$$

and the neutral current (NC):

$$\mathcal{L}_{NC} = \frac{-g}{2\cos\theta_W} j^{\mu}_{NC} Z_{\mu} \quad \text{with} \quad j^{\mu}_{NC} = \bar{f}_{\alpha} \gamma^{\mu} P_L f_{\alpha}, \quad \text{and} \quad P_L = \frac{\mathbb{1} - \gamma^5}{2}, \tag{1.4}$$

where α stands for the flavor of the fermion field f, W_{μ} and Z_{μ} are the W-boson and Z^0-boson fields, g is the weak coupling constant associated with $SU(2)_L$ and θ_W is the Weinberg angle. Equation 1.4 determines the decay width of the Z^0-boson into light active ($m_{\nu} \leq m_{Z^0}/2$) neutrinos. The precise measurement

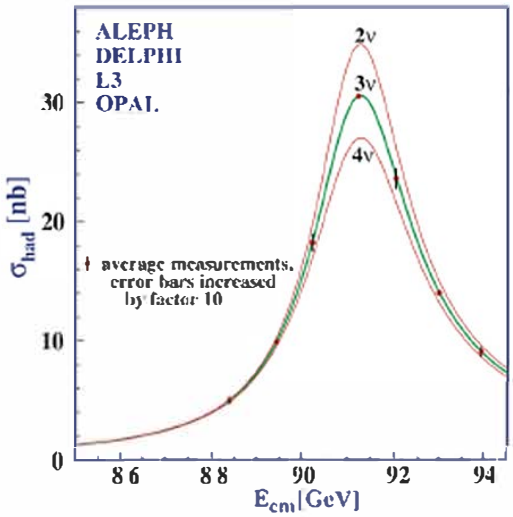

Figure 1.3: Combined data from the ALEPH, DELPHI, L3, and OPAL Collaborations for the cross section in $e^+ + e^-$ annihilation into hadronic final states as a function of the center-of-mass energy near the Z pole. The curves show the predictions of the Standard Model with two, three, and four species of light neutrinos. Note that the error bars have been increased by a factor of ten for display purposes. From [?].

of the decay width of the Z^0, which can be seen in fig. 1.3, indicates that there are three, and only three, flavors of active neutrinos.

The mass of any fermion is generated via a Yukawa coupling of the scalar Higgs doublet ϕ to the right-handed singlet and left-handed doublet of the fermion. For leptons this Yukawa coupling can be written as

$$\mathcal{L}_Y = Y^{\ell}_{\alpha\beta} \bar{L}_\alpha \phi E_\beta + h.c., \tag{1.5}$$

where $E_\beta = (e_R, \mu_R, \tau_R)$ are the right-handed singlets, and L_α are the left-

handed doublets

$$L_e = \begin{bmatrix} \nu_{eL} \\ e_L \end{bmatrix}, \quad L_\mu = \begin{bmatrix} \nu_{\mu L} \\ \mu_L \end{bmatrix}, \quad L_\tau = \begin{bmatrix} \nu_{\tau L} \\ \tau_L \end{bmatrix}. \tag{1.6}$$

After spontaneous symmetry breaking these terms lead to charged lepton masses

$$m_{ij}^{\ell} = Y_{\alpha\beta}^{\ell} \frac{v}{\sqrt{2}}, \tag{1.7}$$

where v is the vacuum expectation value of the Higgs field. However, since the model does not contain right-handed neutrinos, no such Yukawa interaction can be built for neutrinos, which are consequently massless.

1.3 Neutrino Oscillation

Neutrino oscillation [14] is a quantum mechanical phenomenon which was first introduced by Bruno Pontecorvo in 1957. It describes the process by which any neutrino type (ν_e, ν_μ, or ν_τ) can change its flavor after traveling a certain distance. The evidence of oscillations has accumulated over the years from the observation of solar, atmospheric, reactor and beam neutrinos. Sudbury Neutrino Observatory (SNO) and Super-Kamiokande provided decisive results for the existence of oscillations, which was recognized by the Nobel Prize committee in 2015; however, the number of experiments that have made significant contributions in measuring neutrino oscillations is much larger.

The most relevant implication of neutrino oscillations is the necessity of finite mass, as will be explained in more detail below. This is currently the only experimentally verified deviation from the SM and requires a modification

thereof. Because of their distinct non-zero masses, the neutrino flavor eigenstates can be expressed as a superposition of three different mass eigenstates. The mixing between

$$\text{flavor} \quad |\nu_\alpha\rangle = \sum_i U^*_{\alpha i} |\nu_i\rangle \quad \text{and mass eigenstates} \quad |\nu_i\rangle = \sum_\alpha U_{\alpha i} |\nu_\alpha\rangle$$

with $\alpha = e, \mu, \tau$ and $i = 1, 2, 3$, is given by the Pontecorvo-Maki-Nakagawa-Sakata (PMNS) matrix:

$$U = \begin{bmatrix} 1 & 0 & 0 \\ 0 & c_{23} & s_{23} \\ 0 & -s_{23} & c_{23} \end{bmatrix} \begin{bmatrix} c_{13} & 0 & s_{13}e^{-i\delta_{CP}} \\ 0 & 1 & 0 \\ -s_{13}e^{-i\delta_{CP}} & 0 & c_{13} \end{bmatrix} \begin{bmatrix} c_{12} & s_{12} & 0 \\ -s_{12} & c_{12} & 0 \\ 0 & 0 & 1 \end{bmatrix} \mathcal{P} \quad (1.8)$$

where $c_{ij} = \cos\theta_{ij}$, $s_{ij} = \sin\theta_{ij}$ and δ_{CP} is the CP-violating phase. In the case of Dirac neutrinos, $\mathcal{P} = \mathbb{1}_3$, and for Majorana neutrinos, $\mathcal{P} = diag(e^{i\alpha_1}, e^{i\alpha_2}, 0)$, more details can be found in [15, 16]. The oscillation probability of a neutrino of flavor α to be detected with flavor β is:

$$P_{\nu_\alpha \to \nu_\beta} = |\langle \nu_\beta | \nu_\alpha \rangle|^2 = \sum_{i,k} U^*_{\alpha i} U_{\beta i} U_{\alpha k} U^*_{\beta k} e^{i(E_k - E_i)L} \quad (1.9)$$

where L is the baseline or distance between creation of ν_α and detection of ν_β. For relativistic neutrinos ($m_k << p_k$), the energy can be approximated as

$$E_k = \sqrt{p_k^2 + m_k^2} \simeq p_k + \frac{m_k^2}{2p_k}. \quad (1.10)$$

Setting all momenta of the propagating neutrino mass eigenstates $\mathrm{p}_k = \mathrm{E}$ yields $\mathrm{E}_k \simeq E + \frac{m_k^2}{2E}$, so that $E_i - E_k = \frac{\Delta m_{ik}^2}{2E}$, with $\Delta m_{ik}^2 = m_i^2 - m_k^2$, simplifies

eq. (1.9) to:

$$P_{\nu_\alpha \to \nu_\beta} = \delta_{\alpha\beta} - 4\sum_{i>k} Re(U^*_{\alpha i}U_{\beta i}U_{\alpha k}U^*_{\beta k}) \sin^2\left(\frac{\Delta m^2_{ik}L}{4E}\right) + 2\sum_{i>k} Im(U^*_{\alpha i}U_{\beta i}U_{\alpha k}U^*_{\beta k}) \sin\left(\frac{\Delta m^2_{ik}L}{2E}\right), \quad (1.11)$$

which shows that $P_{\nu_\alpha \to \nu_\beta} = 1$ for $m_i = m_k$ or $m_i = 0$ for all i. Notice also that one of the three active neutrinos is allowed to have zero mass. The neutrino oscillation probability only depends on the differences between the neutrino masses-squared, Δm^2_{ik}, and on the mixing matrix elements, U_{ik}. But it is insensitive to the absolute mass scale of neutrinos and provides no information on whether they are Dirac or Majorana particles, since the Majorana phases, $\alpha_{1,2}$, do not enter the oscillation probabilities. Therefore, neutrino oscillation experiments set constraints on the values of the six parameters that govern the neutrino mixing, namely the mixing angles $(\theta_{12}, \theta_{13}, \theta_{23})$, mass splittings $(\Delta m^2_{21}, \Delta m^2_{32} \simeq \Delta m^2_{31})$, δ_{CP}, and the neutrino mass hierarchy.

Since the position of the oscillation maximum depends on the neutrino energy E and the travelled distance L, accelerator long-baseline neutrino oscillation experiments are in a unique position to make high precision measurements of the oscillation parameters because they have a handle on the energy E of their neutrino beam and on the distance to the detection site L.

This type of experiment usually consists of a pair of detectors, near and far, that measures the neutrino flux spectrum and flavor composition before and after oscillations, respectively. The location and energy of their beam as

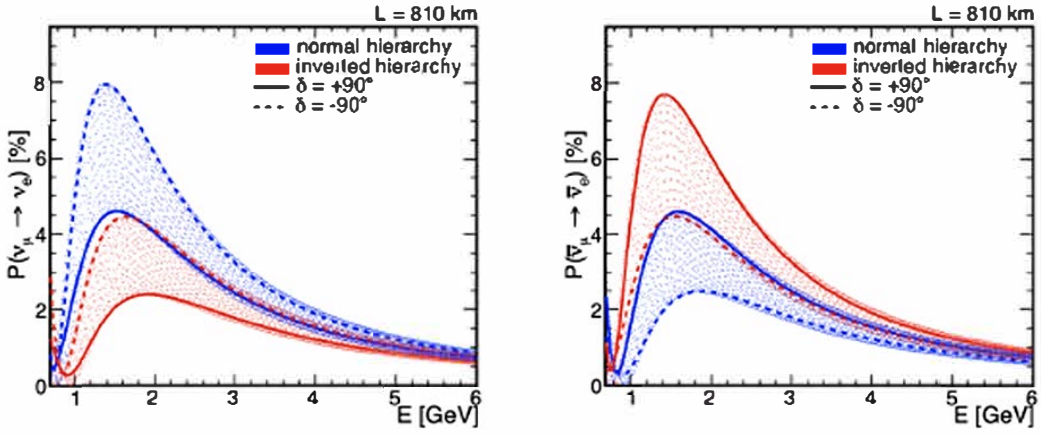

Figure 1.4: Appearance probability of $P(\nu_\mu \rightarrow \nu_e)$ (left) and $P(\bar{\nu}_\mu \rightarrow \bar{\nu}_e)$ (right) as a function of energy E. From [17].

well as the location of the far detector are chosen such that the appearance or disappearance probabilities show a maximum or a minimum respectively. Figure 1.4 shows the probability of oscillation for the NOνA experiment (at $L = 810$ km) which is almost maximal for neutrinos from the NuMI beam with energies ~ 2 GeV.

While the absolute values of the Δm^2_{ik} have been measured, the sign of the mass-squared difference is only known for Δm^2_{12} and the values of the three active neutrino masses remain unknown. This leads to two possible mass orderings for neutrinos: the normal ordering with $m_1 < m_2 < m_3$ and the inverted ordering $m_3 < m_1 < m_2$, see fig. 1.5.

In order to measure the δ_{CP} phase, accelerator long-baseline neutrino experiments can make use of the two beam polarities to explore the differences in matter effects on the oscillations in the $\nu_\mu \rightarrow \nu_e$ and $\bar{\nu}_\mu \rightarrow \bar{\nu}_e$ chan-

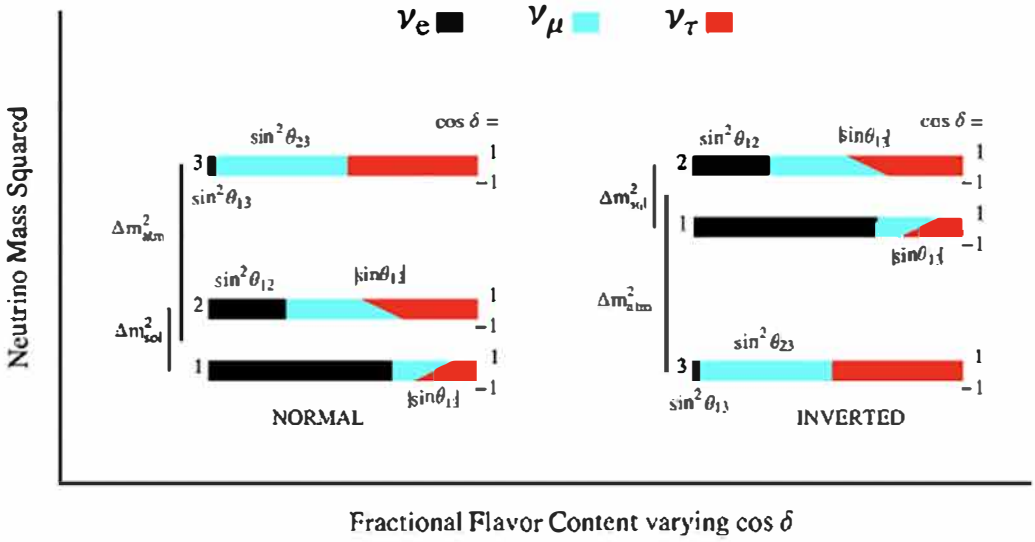

Figure 1.5: The range of probability of finding the α-flavor in the i-th mass eigenstate for the two different mass hierarchies. The best fit values of the solar and atmospheric mixing parameters were used as δ_{CP} is varied from -1 to 1. From [18].

nels. The NOνA, MINOS and T2K [19–21] experiments have measured the δ_{CP} phase, but not yet with enough accuracy to provide a definite value and their results are in slight tension with each other. The next generation experiments, The Deep Underground Neutrino Experiment (DUNE) [22] and Hyper-Kamiokande [23], will be in a better position to definitely answer this question. This measurement is crucial to tackle the question of how a Universe initially equally composed of matter and anti-matter evolved to a matter dominated one. The baryon-sector (quark-sector) also has a CP-violating phase, but its small value is not able to account for the imbalance. A sufficient large value of the δ_{CP} from neutrino mixing might be able to resolve the mystery through a process called leptogenesis.

1.4 Neutrino Masses

As explained in the previous section, experiments indicate that neutrinos oscillate and hence at least two of the three have non-zero masses, which contradicts the Standard Model. To accommodate this finding, a Dirac mass term for neutrinos, similar to the one for charged leptons and quarks, see eq. (1.5), could be added to the SM Lagrangian. This would require the existence of right-handed neutrinos, sterile neutrino eigenstates that do not participate in weak interactions but contribute to the mass term, and the Yukawa coupling would have to be very small compared to the other Yukawa couplings from charged leptons and quarks, see fig. 1.6. The individual lepton numbers L_e, L_μ and L_τ would be violated while the total lepton number would

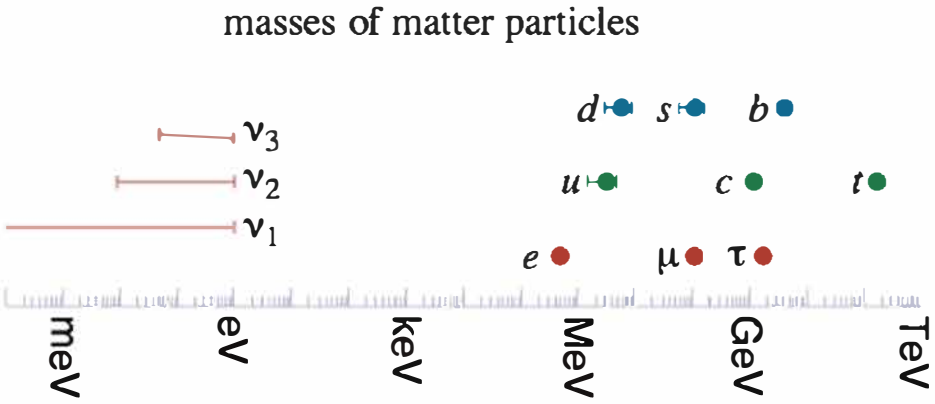

Figure 1.6: Masses of fundamental particles in the Standard Model. Neutrino masses are anomalously small when compared to other particles. This difference in mass scale is similar to that of the weight of an ant (the neutrino) vs an elephant (the electron). From [3].

be conserved.

A more elegant way of introducing neutrino masses would be through a Majorana term, which violates the lepton number by two units. Neutrinos are the only known fermions that could possibly be their own anti-particles (i.e. Majorana fermions with $\nu = \bar{\nu}$) because they have no electromagnetic charge. The see-saw mechanism introduces right-handed neutrinos with very large Majorana masses, which induce a reciprocally small mass for the left-handed neutrinos. In contrast to the Dirac mass term approach, the latter provides a natural explanation for the smallness of the neutrino masses and may also explain baryon asymmetry via leptogenesis, since the two additional Majorana phases are also CP-violating.

The detection of neutrinoless double beta decay would point towards a

Majorana nature of neutrinos and their mass scale. This process is a radioactive decay happening inside a nucleus in which two neutrons are simultaneously transformed into two protons, or vice versa, and instead of emitting two electrons (positrons) and two anti-neutrinos (neutrinos), the nucleus only emits two electrons (positrons) because the two (anti-)neutrinos have annihilated each other (Majorana style). Experiments like GERDA (for GERmanium Detector Array) at Gran Sasso Underground Laboratory in Italy [24] and the future LEGEND experiment [25] explore neutrinoless double beta decay of ^{76}Ge. KamLAND-Zen 800 located in a drift mine shaft in the Japanesse Alps uses ^{136}Xe as an isotope and is currently the most sensitive experiment running [26].

A model-independent, direct method to probe the neutrino mass scale with sub-eV precision is being pursued by the Karlsruhe Tritium Neutrino Experiment (KATRIN), an enormous spectrometer aiming to examine the spectrum of electrons emitted from the beta decay of tritium [27]. Project 8 is similarly searching for endpoint kinematic distortions by measuring the frequency of cyclotron radiation emitted from decay electrons with the potential to reach sensitivities down to $\lesssim 0.4$ meV [28].

1.5 Neutrino Interactions

In theory, as seen in eq. 1.3 and 1.4, there are only two types of interactions: charged current (CC) and neutral current (NC), see fig. 1.7. In a CC interaction a neutrino enters and a charged lepton leaves through the

exchange of a charged $W^{\pm}$-boson. The flavor of the outgoing lepton reveals the flavor of the incoming neutrino, and the charge of the outgoing lepton determines whether it is a neutrino or an anti-neutrino. In the NC process both the incoming and the outgoing particle are neutrinos since the mediator is a neutral Z^0-boson. In this case it is impossible to reconstruct kinematics of the incoming neutrino from the final state particles.

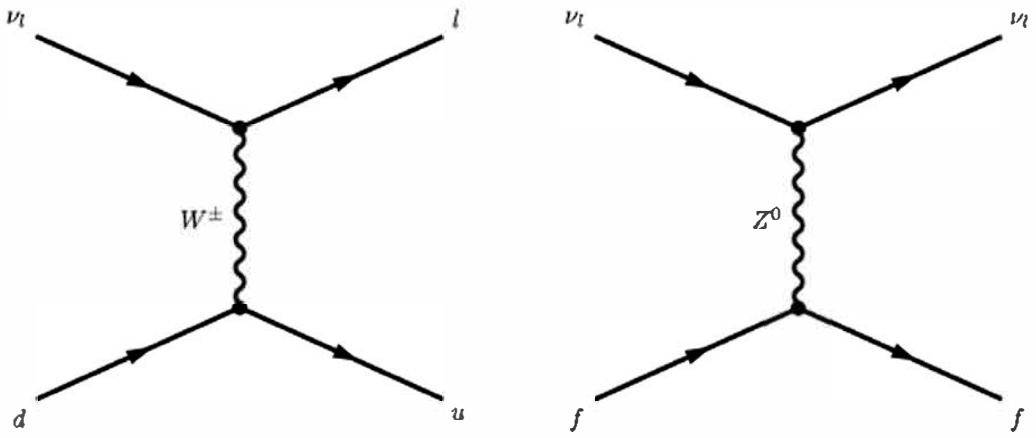

Figure 1.7: Charged (left) and neutral current (right) neutrino-nucleus interaction process.

Nevertheless, in most experiments like NOνA, the interaction of the neutrino may not be with just an isolated elementary particle or a single nucleon. Rather, it interacts with particles bounded in atomic nuclei, which leads to nuclear effects impacting the interaction cross section as well as the observed final states. The higher the energy of the neutrino, the smaller is the length scale of the interaction with its partner: the nucleus, the nucleons, and the quarks. Below $E_\nu \sim 1$ GeV, a nucleus is effectively a collection of point-

like nucleons, whereas for higher energies $E_\nu \gtrsim 5$ GeV, the four-momentum transfer is large enough to probe the nucleon structure, and interactions with partons dominate the total cross section.

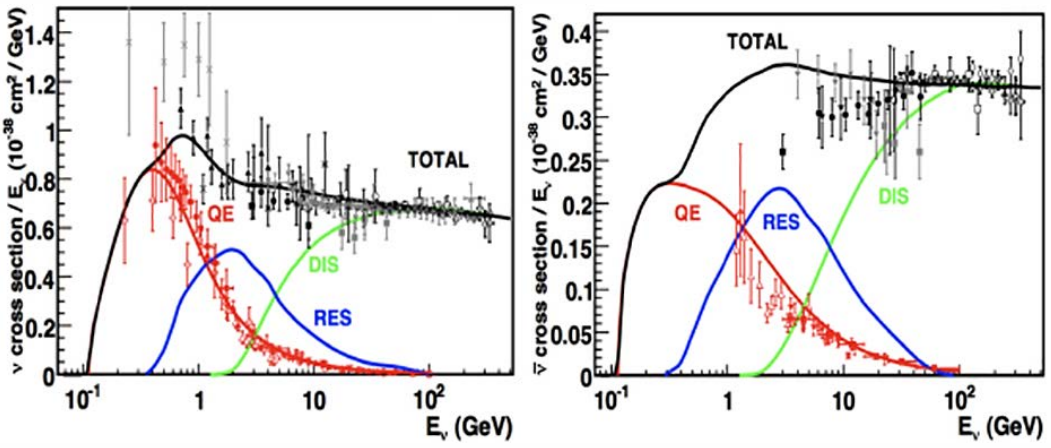

Figure 1.8: Total neutrino (left) and antineutrino (right) per nucleon CC cross sections (for an isoscalar target) divided by neutrino energy and plotted as a function of energy, from [29]. The three processes Quasi-Elastic Scattering (QE), Resonant Production (RES) and Deep Inelastic Scattering (DIS) are explained in the following.

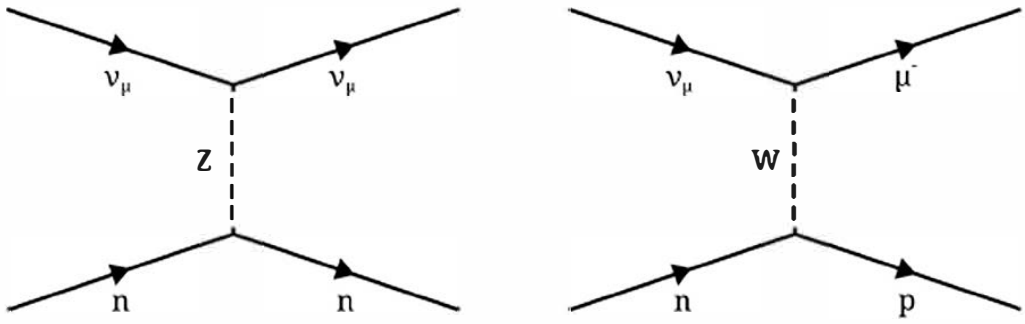

Figure 1.9: Feynman diagram for a NC elastic (left) and CC quasi-elastic process (right).

The transition energy range with $E_\nu \sim 0.1 - 20$ GeV presents a mix of processes contributing to the total cross section, see fig 1.8. The variety of neutrino scattering mechanisms playing a role within this intermediate energy range can be organized into three categories:

- **(Quasi-)Elastic Scattering (QE):** Neutrinos elastically scattering off an entire nucleon releasing a single baryon from the target, see fig. 1.9. For neutral currents this process is called "elastic scattering"

$$\nu\, p \to \nu\, p, \quad \bar{\nu}\, p \to \bar{\nu}\, p,$$
$$\nu\, n \to \nu\, n, \quad \bar{\nu}\, n \to \bar{\nu}\, n,$$

  since the initial nucleon does not change, whereas for charged currents

$$\nu_\mu\, n \to \mu^-\, p, \quad \bar{\nu}_\mu\, p \to \mu^+\, n,$$

  this process requires a transition of the nucleon from a neutron to a proton or vice versa, and is therefore traditionally referred to as "quasi-elastic scattering".

- **Resonant Production (RES):** Neutrinos can excite the target nucleon to a resonance state, see left diagram in fig. 1.10. The resultant baryonic resonance decays into a variety of combinations of nucleons and mesons. For intermediate neutrino energies this is the most common process for

single pion production with different final states for charge current

$$\nu_\mu\, p \to \mu^-\, p\, \pi^+, \quad \bar{\nu}_\mu\, p \to \mu^+\, p\, \pi^-,$$
$$\nu_\mu\, n \to \mu^-\, p\, \pi^0, \quad \bar{\nu}_\mu\, p \to \mu^+\, n\, \pi^0,$$
$$\nu_\mu\, n \to \mu^-\, n\, \pi^+, \quad \bar{\nu}_\mu\, n \to \mu^+\, n\, \pi^-,$$

and for neutral current

$$\nu_\mu\, p \to \nu_\mu\, p\, \pi^0, \quad \bar{\nu}_\mu\, p \to \bar{\nu}_\mu\, p\, \pi^0,$$
$$\nu_\mu\, p \to \nu_\mu\, n\, \pi^+, \quad \bar{\nu}_\mu\, p \to \bar{\nu}_\mu\, n\, \pi^+,$$
$$\nu_\mu\, n \to \nu_\mu\, n\, \pi^0, \quad \bar{\nu}_\mu\, n \to \bar{\nu}_\mu\, n\, \pi^0,$$
$$\nu_\mu\, n \to \nu_\mu\, p\, \pi^-, \quad \bar{\nu}_\mu\, n \to \bar{\nu}_\mu\, p\, \pi^-.$$

- **Deep Inelastic Scattering (DIS):** For high enough energies, the neutrino can directly interact with the individual quarks inside the nucleon, see right diagram in fig. 1.10. This is called deep inelastic scattering and leads to hadronic showers in the final state.

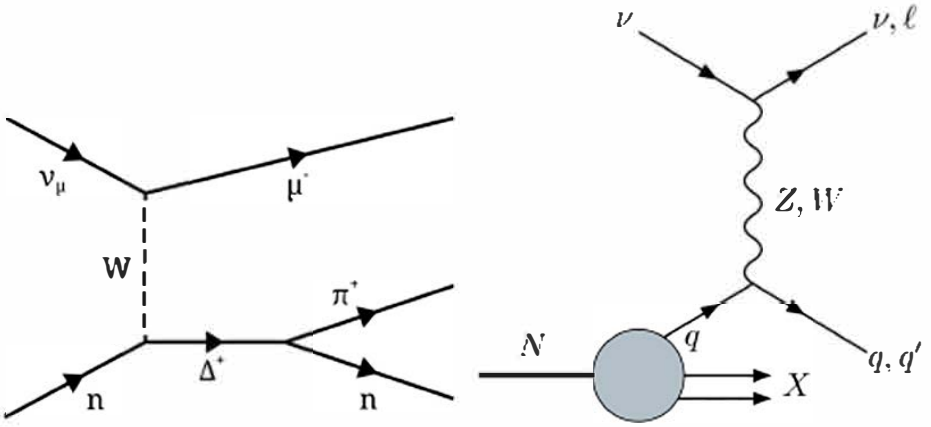

Figure 1.10: Feynman diagram for CC resonant process (left) and a deep inelastic process (right). In the latter the neutrino interacts with a quark q inside the nucleon N.

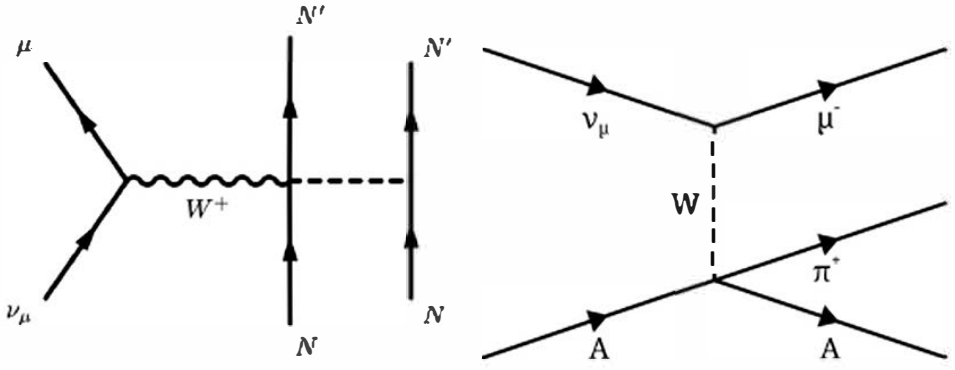

Figure 1.11: Feynman diagram for a CC meson exchange (left) and CC coherent process (right), where the neutrino interacts with the whole nucleus A.

By 2020 it became evident that the QE picture used to describe neutrino scattering off hydrogen in bubble chamber data was insufficient in a nuclear medium [30–33] . It turns out that the meson exchange current (MEC) is the missing piece of the puzzle. MEC is an interaction between an incoming neutrino and a correlated pair of nucleons, a 2-body current mediated by a pion field, see left diagram in fig. 1.11. The weak boson from the leptonic current is exchanged by a pair of nucleons, which leads to a 2-nucleon emission, hence explaining the name of the "2 particle-2 hole (2p-2h)" effect.

Rarely, neutrinos also interact coherently with a target nucleus and produce an outgoing pion via either neutral-current (NC) or charged-current (CC) interactions, see right diagram in fig. 1.11. Coherent interactions are characterized by a very small momentum transfer to the target nucleus with no exchange of quantum numbers, and the target nucleus remains in its ground state. The characteristic signal topology of NC coherent π^0 production

$$\overset{(-)}{\nu} A \rightarrow \overset{(-)}{\nu} A \pi^0 \tag{1.12}$$

is a single, forward-going neutral pion, with no other hadrons in the final state.

This section on neutrino interactions is a summary of information presented in the following sources [34–37].

Chapter 2

The NOνA Experiment

The NOνA experiment (NuMI Off-axis ν_e Appearance) is an accelerator long-baseline neutrino oscillation experiment consisting of two detectors measuring neutrinos from the NuMI (Neutrinos at the Main Injector) beam. Both detectors are functionally identical, but of different size, to facilitate cancellation of systematic errors due to beam flux and cross-section uncertainties. The 300 ton Near Detector (ND) is located 105 m underground in Fermilab, 1 km away from the NuMI target, and the 14 kt Far Detector (FD) is 810 km away from the source on the surface at a site near Ash River, Minnesota, see fig. 2.1. NOνA's main physics goal is to measure neutrino oscillation in different channels:

Disappearance:	$\nu_\mu \to \nu_\mu$ and $\bar{\nu}_\mu \to \bar{\nu}_\mu$,
Appearance:	$\nu_\mu \to \nu_e$ and $\bar{\nu}_\mu \to \bar{\nu}_e$

by comparing the energy spectra of neutrino interactions in both detectors. The most recent NOνA measurements of Δm^2_{32}, $sin^2\theta_{23}$ and δ_{CP} can be found in [20]. Besides the oscillation results, NOνA has a rich physics program among which are sterile neutrinos [39], slow magnetic monopoles [40], neutron-antineutron oscillations [41], supernova [42] and multi-messenger signals [43],

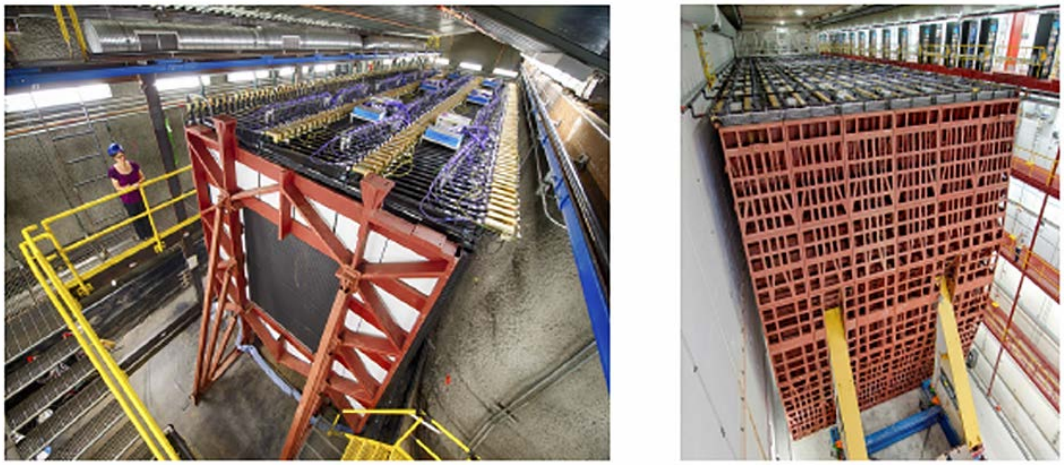

Figure 2.1: Near Detector (left) and Far Detector (right) with humans for scale, from [38].

which are being studied in the Far Detector. The Near Detector provides a great opportunity for various neutrino-nucleus interaction cross sections [44, 45]. The cross section analysis described in this thesis is an expansion on a previous neutral current π^0 production analysis done by Daisy Kalra [37, 46].

After some years of running experience, NOνA finally embarked on a test beam challenge placing a third detector in MC7 at the Fermilab Test Beam Facility in an attempt to improve their detector systematics. More about this project can be found in appendix C.

2.1 NuMI Beam

The NuMI beam (Neutrinos at the Main Injector) facility at Fermilab, which was originally constructed for the MINOS experiment [47], is the source of muon neutrinos and anti-muon neutrinos for NOνA. Over the course of

several years (beginning of the MINOS era to date), it has undergone a series of upgrades to the target and the accelerator complex that have increased the beam power from 320 kW to 700 kW, elevating it to the category of the world's most intense source of neutrinos.

The Fermilab accelerator complex, see fig. 2.2, is comprised of four particle accelerators: Linac, Booster, Recycler and Main Injector (MI). The

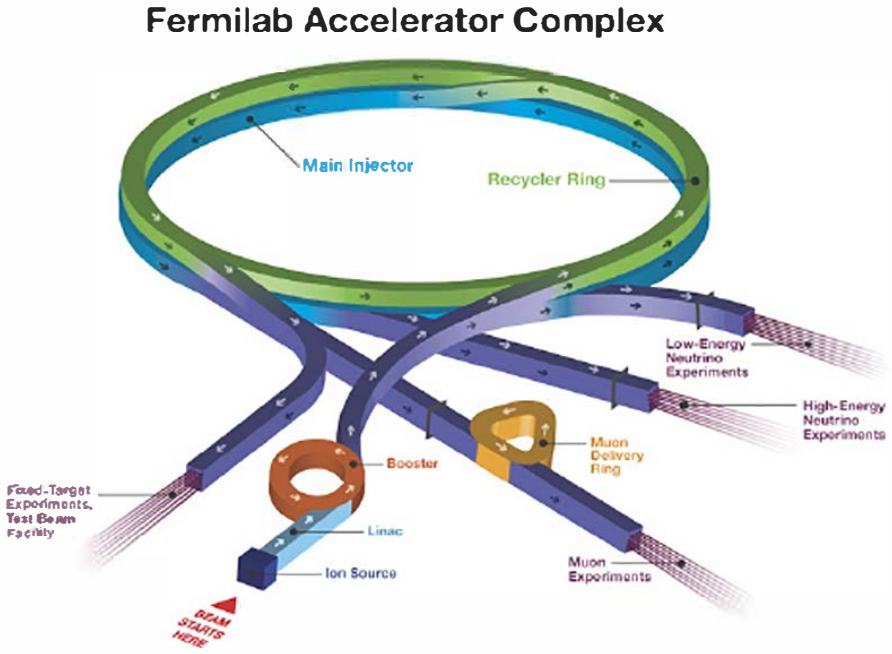

Figure 2.2: Schematic of Fermilab Accelerator Complex showing the starting point of the beam along with the four particle accelerators (LINAC, Booster, Recycler and the Main Injector) from [38].

beam starts with an ion source, which is a radio-frequency quadrupole (RQF) that feeds 35-750 keV H^- ions to the linear accelerator (Linac), where they get accelerated to 400 MeV. At the end of the latter a carbon foil transforms the negative ions into a H^+ beam before they enter the Booster, where their energy gets increased to 8 GeV. After the Booster, the beam enters into the Recycler, a staging area that combines batches of protons into a more intense beam. The Main Injector, situated under the Recycler, is the last stage where the beam gets further accelerated to 120 GeV. The NuMI beamline extracts six batches of the 120 GeV protons from the MI. Each proton extraction is 10 μs long, and is called a spill, which gets delivered every 1.33 s and amounts to $4.9 \cdot 10^{13}$ protons.

2.1.1 NuMI Beamline

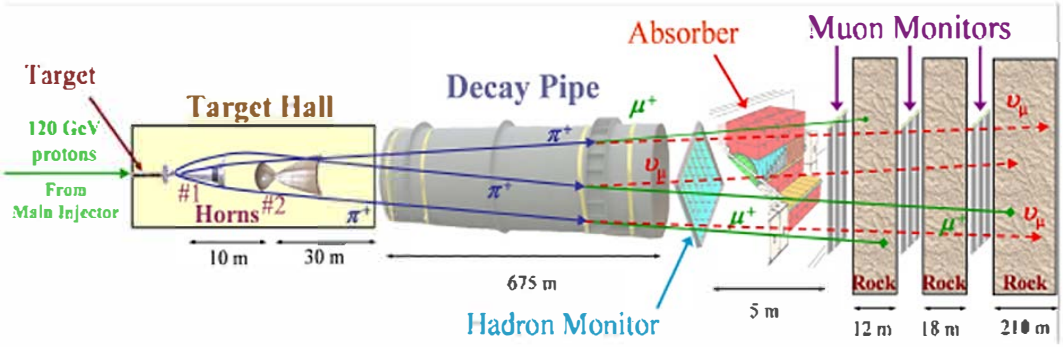

Figure 2.3: Diagram of the NuMI beamline from [38]. The 120 GeV protons hit a graphite target and produce a secondary beam of hadrons, which are then focused by two magnetic horns. The hadrons decay as they travel through the long pipe. Besides the neutrinos from the hadron decays, other particles have been created along the way, predominately muons. The latter are detected and used for beam monitoring purposes by the muon monitors as well as stopped right after by the beam dump or the rock.

The 120 GeV protons collide with the graphite target which is segmented into 48 fins and 1.2 m long, corresponding to two interaction lengths. The resulting mesons, mainly pions and kaons, are focused while traversing through two magnetic horns. These two parabolic-shaped aluminum horns are water-cooled and pulsed with up to 200 kA to focus the hadrons. Depending on their polarity, positively or negatively charged particles get focused. The different polarities are called "forward horn current" (FHC) for focusing π^+, K^+, and "reverse horn current" (RHC) for focusing π^-, K^-.

In flight the mesons decay

$$\pi^{\mp} \to \mu^{\mp} + \overset{(-)}{\nu}_{\mu} \text{ with BR} = 99.98\%$$
$$K^{\mp} \to \mu^{\mp} + \overset{(-)}{\nu}_{\mu} \text{ with BR} = 63.55\%$$

into muons and muon neutrinos in the decay pipe, which is a 675 m long and 2 m in diameter big volume filled with helium at low pressure. After the decay pipe, remaining hadrons and muons get stopped by an absorber and 240 m of rock. More about the NuMI beamline can be found here [48].

2.1.2 Off-Axis Concept

The neutrino flux from the decay of pions and kaons is

$$\Phi = \left(\frac{2\gamma}{1+\gamma^2\theta^2}\right)^2 \frac{A}{4\pi z^2} \tag{2.1}$$

where $\gamma = E_{\pi,K}/m_{\pi,K}$, θ is the angle between the meson and the outgoing neutrino direction, A is the area of the detector and z is the distance from the

source. The energy of the generated neutrinos is related to their parent pions' and kaons' energy through

$$E_\nu = \frac{0.43E_\pi}{1+\gamma^2\theta^2} \quad \text{and} \quad E_\nu = \frac{0.96E_K}{1+\gamma^2\theta^2}, \tag{2.2}$$

respectively. The relation between flux and energy of the neutrino and parent pion given by equations 2.1 and 2.2 is plotted in fig. 2.4. It is apparent from the right picture that at 14 mrad the energy of the neutrino does not have a strong dependence on the energy of the parent pion.

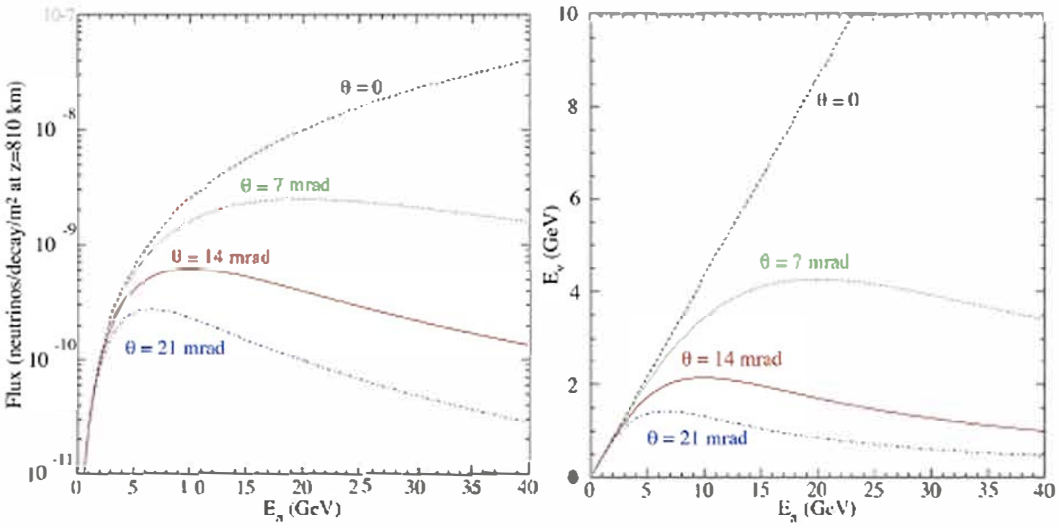

Figure 2.4: Left: Neutrino flux at a location 800 km away from the source and at an angle θ from the beam axis. Right: The energy of the neutrinos produced at an angle θ as a function of the pion energy [49].

The placing of both NOνA detectors 14.6 mrad off the main axis has the advantage of a neutrino flux narrowly peaked at around 2 GeV, see fig. 2.5. In this configuration, the suppression of high energy neutrinos reduces the neutral current background at the region of interest, where the ν_e appearance

and ν_μ disappearance probabilities both experience local maxima at an L/E of around 500 km/GeV.

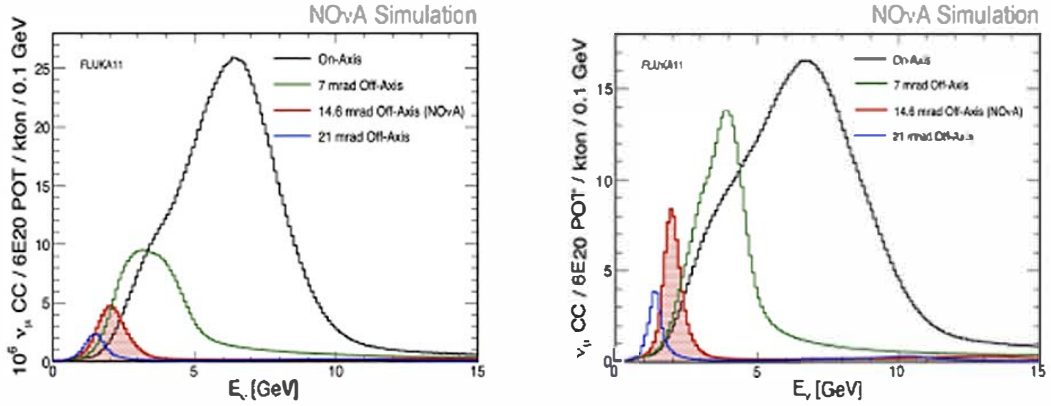

Figure 2.5: Charged current muon neutrino energy spectra (flux x cross-section) for the ND (left) and FD (right) at different angles with respect to the beam axis without oscillations taken into account.

2.1.3 Flux

The beam is contaminated with electron neutrinos, because of the muons and kaons decaying in flight:

$$\mu^- \rightarrow e^- + \bar{\nu}_e + \nu_\mu \quad \text{and} \quad K^- \rightarrow \pi^0 + e^- + \bar{\nu}_e \quad \text{for FHC} \tag{2.3}$$

$$\mu^+ \rightarrow e^+ + \nu_e + \bar{\nu}_\mu \quad \text{and} \quad K^+ \rightarrow \pi^0 + e^+ + \nu_e \quad \text{for RHC} \tag{2.4}$$

In addition, there is the so called "wrong" sign contamination coming from inefficiencies in defocussing the wrong sign hadrons that travel through the center of the magnetic horns, which will eventually decay into wrong sign neutrinos.

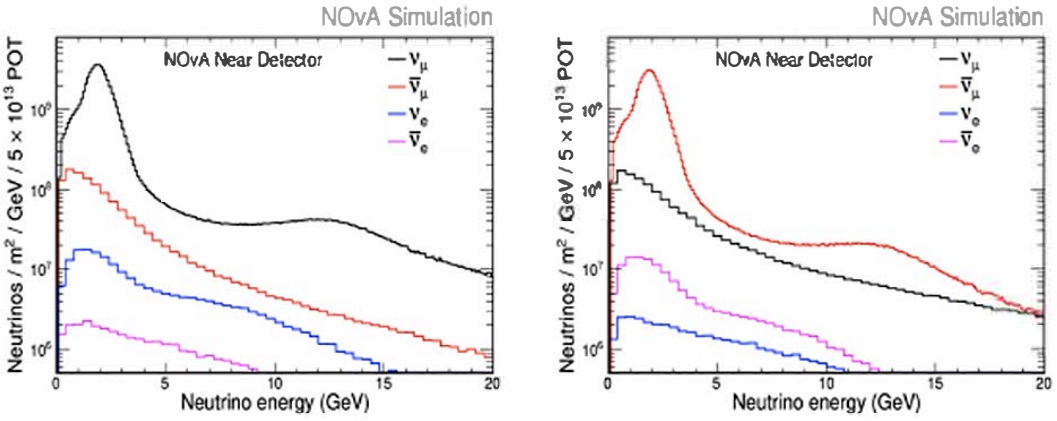

Figure 2.6: Predicted PPFX/-based neutrino beam flux components for the ND flux in the FHC (left) and the RHC (right) in absence of oscillations. The peak at 2 GeV is from pion parents and the smaller one at 14 GeV comes from kaon parents [50].

Component	FHC ND(%)	Component	RHC ND(%)
ν_μ	95	$\bar{\nu}_\mu$	93
$\bar{\nu}_\mu$	4	ν_μ	6
ν_e and $\bar{\nu}_e$	1	ν_e and $\bar{\nu}_e$	1

Table 2.1: Percentages of the different neutrino flavors composing the beam integrated from 1-5 GeV from [51].

2.2 NOνA's Detection Technology

The NOνA detectors are constructed from alternating, orthogonal planes of glued rigid cells, see fig 2.7. The Far Detector comprises a total of 895 planes with 384 cells each, which amounts to a total of 344 k channels. The detector's cross section is a square of 15.5 m sides and it is 59.8 m long, with a total mass of 14 kt. The FD is on the surface of the Earth and its only protection from cosmic rays consists of 1.2 m of concrete and 15 cm of barite, equivalent to about 10 radiation lengths. Because of the FD's small amount of shielding from cosmic rays and the large surface area, it is subjected to a high cosmic ray muon rate of 180 kHz.

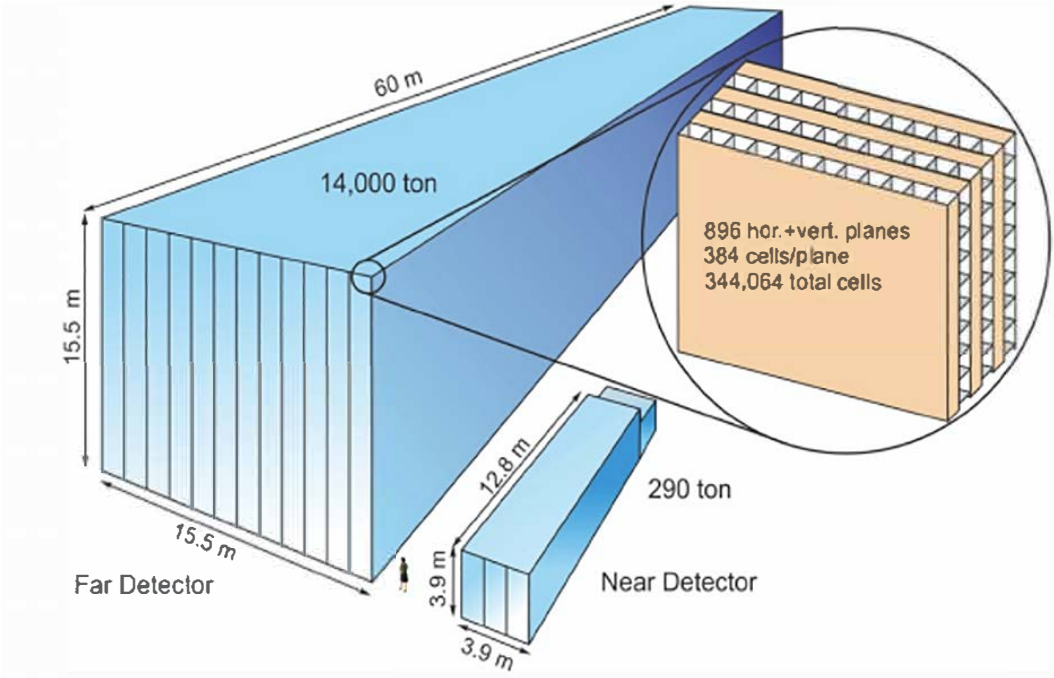

Figure 2.7: Dimensions of Near and Far Detectors, which are constructed from alternating orthogonal and vertical planes.

The Near Detector has dimensions 3.9 m x 3.9 m and is 12.75 m long. It has 192 planes with 96 cells each and weighs 0.3 kt. The last 22 planes of the ND are alternated with one 10 cm thick steel plate every two PVC planes and is only two thirds the height of the detector. This part is called the muon range catcher or stopper reflecting its purpose to contain up to 3 GeV muons produced in the upstream active region of the detector. The ND location underground suppresses the cosmic ray muon rate to a modest 50 Hz.

The alternating orthogonal planes allow 3D event reconstruction. The vertical planes form the top-view or "x-view" and the horizontal planes form the side view or "y-view" of event displays, a schematic of which can be seen in fig 2.8. The detectors were designed for the identification of electron-type neutrino events and therefore made of low Z materials which allows electromagnetic showers from electrons and photons to build up over many planes and cells.

An electromagnetic (EM) shower can be described with two variables: the Molière radius R_M and the radiation length X_0, which respectively account for the transverse and longitudinal dimension of the shower. The Molière radius is largely independent of the particle's energy and can be written in terms of the radiation length

$$R_M = X_0 \frac{E_S}{E_C},$$

where E_S is the multiple scattering energy, and E_C is the critical energy. About 95% of the EM shower is contained laterally in a cylinder with radius $2R_M$.

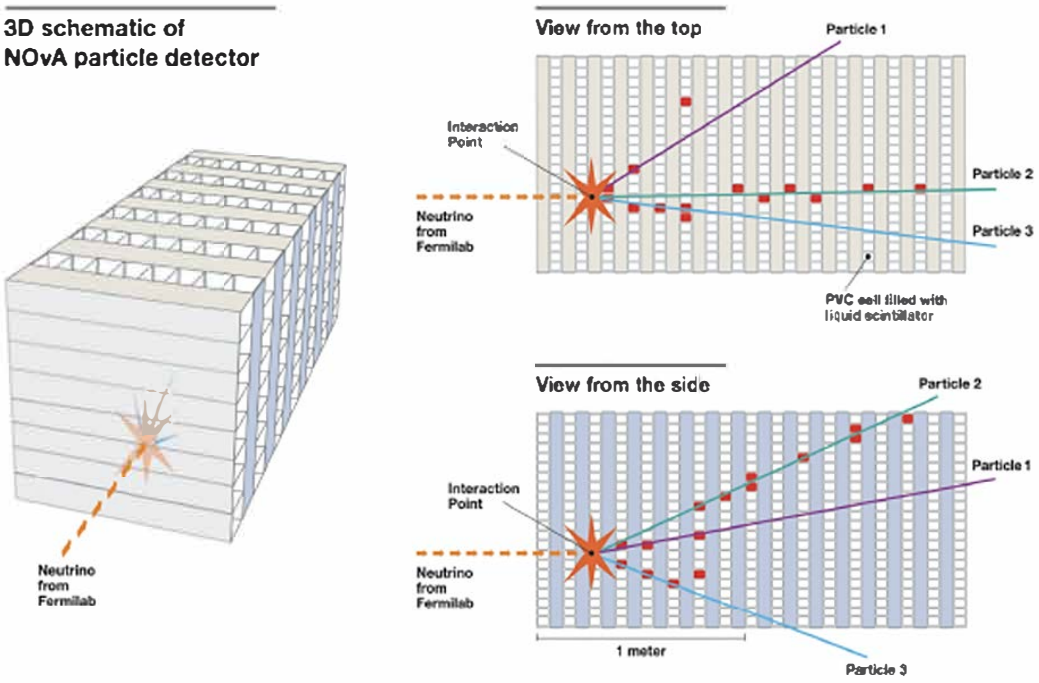

Figure 2.8: Schematic of the alternating PVC plane structure enabling 3D reconstruction of the particles as they travel through it. Horizontal and vertical planes provide the side and top views, respectively.

For NOνA, R_M is 10.5 cm which is roughly the width of 3 cells, while X_0 is 38 cm, or equivalently the length of 6 planes. The length X of electromagnetic showers can be calculated by

$$X = X_0 \frac{ln(E_0/E_C)}{ln2},$$

where E_0 is the initial energy of the particle. The main difference between electrons and photons is that the latter travel through the detector for one radiation length before converting into an e^+-e^- pair and producing scintillation light. One way of spotting neutral pions is looking for a gap between the vertex and the start of a shower, see fig 2.9.

2.2.1 The NOνA Cell

The basic unit of the NOνA detectors is a highly reflective polyvinyl chloride (PVC) cell, see left picture in fig. 2.10, which has an interior width of 3.8 cm transverse to the beam direction and an interior depth of 5.9 cm along the beam direction. Each cell is filled with liquid scintillator and a looped wavelength shifting fiber. A charged particle traversing the liquid interacts with its molecules exciting them, which then emit photons isotropically. These UV photons get wavelength shifted within the fluid, reflected by the TiO_2 coated walls and eventually captured, guided by the wavelength shifting (WLS) optical fiber. Both fiber's ends connect to one single pixel of an Hamamatsu Avalanche Photodiode (APD), which amplifies and digitizes the light.

A pair of 16 cell PVC extrusions are glued together to form a 32 cell

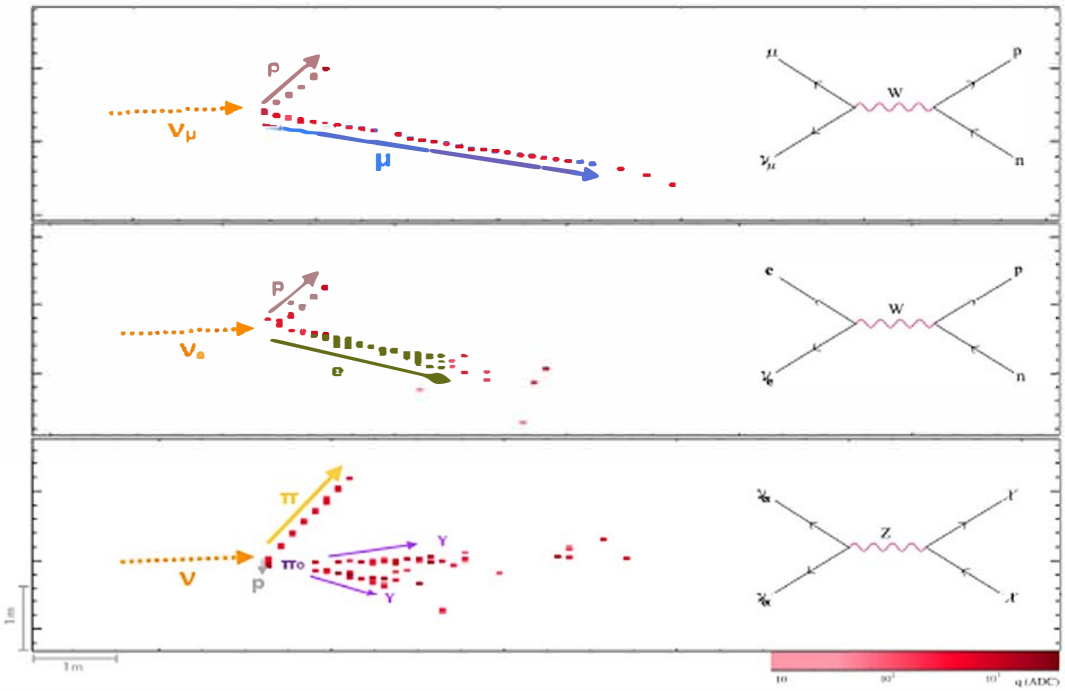

Figure 2.9: Example event topologies in ND from data files. Top: muon neutrino charged current interaction. Middle: electron neutrino charged current interaction. Bottom: neutrino neutral current interaction with a π^0 in the final state [52].

module, see right picture in fig 2.10. One end of the module is capped with a reflective plastic seal and the other end is closed via the manifold cover.

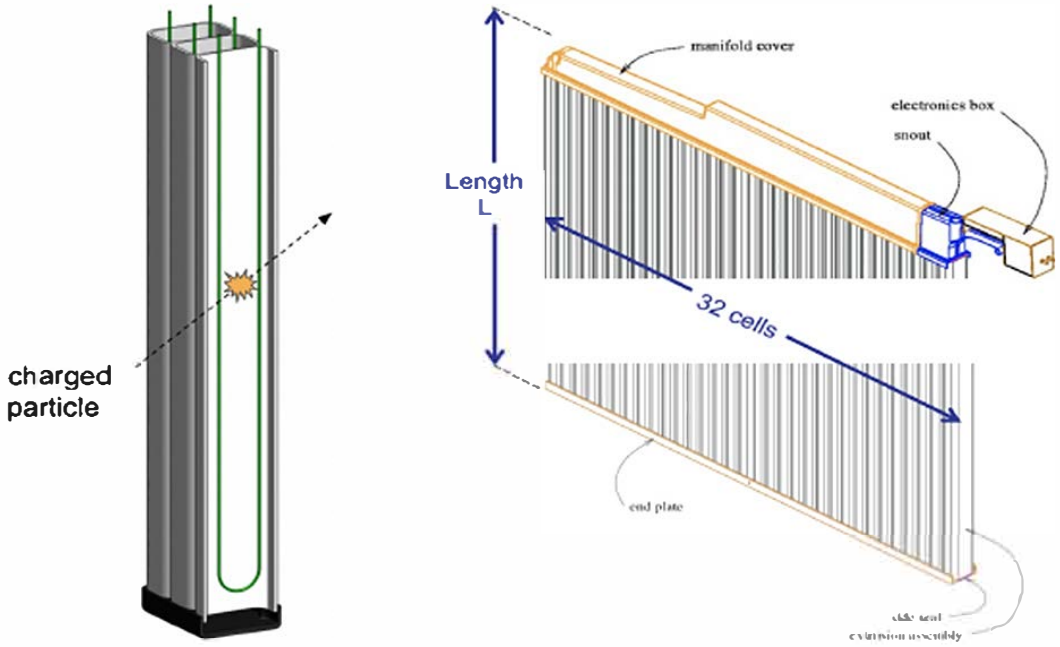

Figure 2.10: Left: a cell containing a looped wavelength shifting fiber (green) surrounded by liquid scintillator, drawn by Marek Proga. An incident, charged particle produces light that bounces off the cell's highly reflective TiO_2 coated walls until absorbed by the fiber. The latter guides the light to an APD. Right: a NOνA extrusion module constructed from two side by side 16 cell PVC extrusions and capped at both ends to contain the liquid scintillator. The manifold end also routes the 64 fiber ends to a cookie which couples to an APD, from [49].

2.2.2 The NOνA Liquid Scintillator

While the PVC cell skeleton accounts for about 35% of the total mass of the detectors, the remaining 65% comprises the active material and comes from the liquid scintillator filling it. The composition of the scintillator was chosen

to satisfy NOνA's performance requirements and an in depth description of its production can be found in [53]. The components of the custom made NOνA scintillator blend are:

- Mineral oil (94% by mass fraction) solvent with an attenuation length greater than 5 meters for photons of 420 nm wavelengths,
- Pseudocumene (4.9% by mass fraction) main scintillant that generates photons in the UV range,
- Scintillator wavelengthshifter 1: PPO, or 2,5-diphenyloxazole, (0.11% by mass fraction) shifts the UV photons to a longer wavelength,
- Scintillator wavelengthshifter 2: bis-MSB, or 1,4-dimethylstyryl-benzene, (0.0016% by mass fraction) shifts the already shifted photons to even longer wavelengths appropriate for capture by WLS fiber,
- Stadis-425 (0.001% by mass fraction) antistatic agent that prevents charge build-up,
- Vitamin E (0.001% by mass fraction) antioxidant, preventing degradation by yellowing of the mineral oil.

2.2.3 The Wavelength Shifting Fiber

The fiber is 0.7 mm in diameter with a core of polystyrene mixed with 300 parts per million R27 dye as the wave-shifter. The WLS fiber retains the 400-450 nm, blue photons from the scintillator and wavelength shifts them

to green photons in the range of 490-550 nm. The attenuation of the light traveling through 15.5 m of fiber is about a factor of ten, with green light preferentially surviving.

2.2.4 The Avalanche Photodiode (APD)

Both ends of the WLS fiber are read out by one pixel of a 32-pixel Avalanche Photodiode, see fig. 2.11. Each pixel is a silicon detector, where an

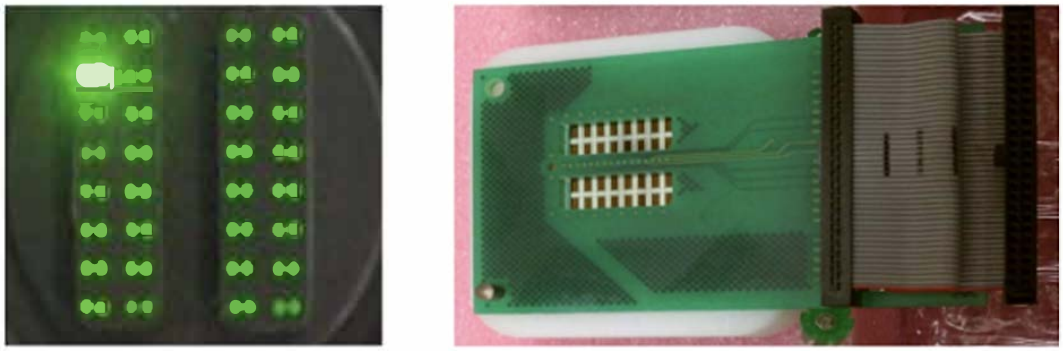

Figure 2.11: Left: the ends of 32 wavelength-shifting fibers organized in a cookie at the end of a module to mount to an APD. Right: custom designed 32-pixel Avalanche Photodiode from [54].

incident photon coming from the fibers knocks out an electron from a silicon atom producing an electron-hole pair. A high reverse bias voltage of around 425 V generates an electric field across the silicon wafer ahead of a p-n junction. The electrons drift past the p-n junction where the electron signal avalanches, leading to an amplification of the latter. The voltage applied to each APD is carefully set and monitored to ensure a consistent amplification across all channels in the detector. The gain is set to 150 to increase the signal-to-noise ratio. To reduce the thermal noise, each APD is kept at -15°C using

a thermal-electric cooler (TEC) device controlled by the front-end electronic board (FEB).

The quantum efficiency for a NOνA APD as well as one for a typical PhotoMultiplier Tube (PMT) and the NOνA scintillator emission spectrum is shown in fig 2.12.

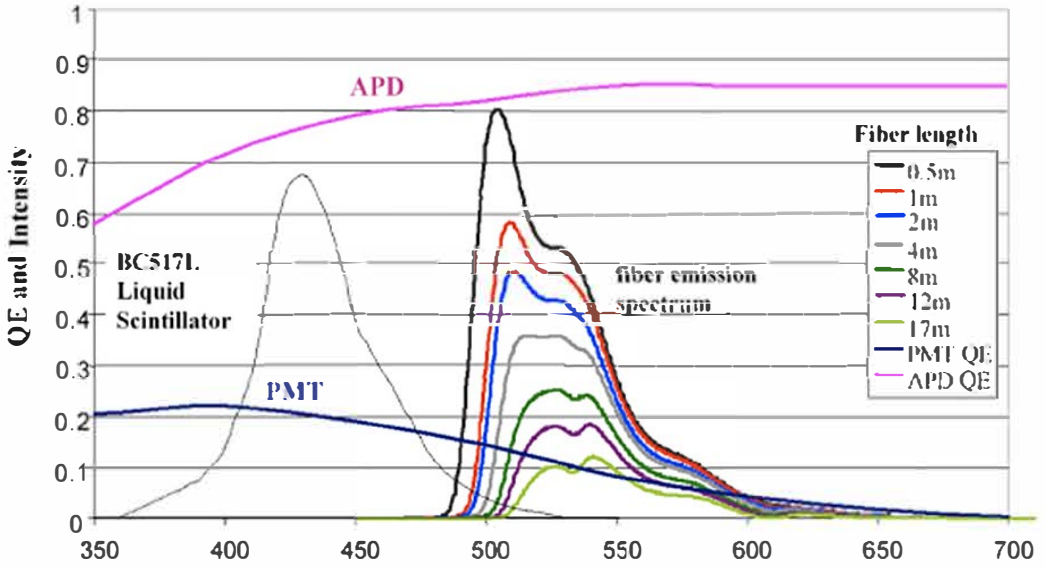

Figure 2.12: The quantum efficiency for a NOνA APD is depicted in pink as a function of the wavelength [nm]. The fiber dye emission spectrum for several fiber lengths is shown in the 480-600 nm range, which coincides with a consistent APD quantum efficiency of 80%. For reference, the FD planes are 15.5 m long and 3.9 m for the ND. The typical PMT quantum efficiency is shown in blue and the liquid scintillator emission spectrum is in gray. From [54].

2.3 Data Acquisition System

The primary task of the Data Acquisition System (DAQ) is to concentrate the data from the large number of APD channels (344 k channels for

the Far Detector, 20 k channels at the Near Detector), buffer this data long enough to apply online triggers, and record the selected data. The detector runs in a continuous readout mode. In this mode all the hits that appear in the detector above a noise threshold receive a time stamp, are read out, sorted into continuous time windows and stored in a deep hit buffer.

For each APD there is a FEB (short for front end board) time stamping, shaping and digitalizing the signal at 500 ns intervals for the FD and 125 ns for the ND to cope with the higher intensity environment. The FEBs send their information down to the data concentration modules (DCMs) to form bigger, synchronized data packages that are ready to be transmitted directly to the buffer farm via Gigabit Ethernet. The DCMs organize the data into 50 μs long units called micro-slices. These micro-slices are aggregated by an event builder module in the DCM into 5 ms chunks or milli-slices. The length of these units has been optimized to the transmission over the internal bus and Ethernet. These milli-slices are dispatched by the DCMs to a pool of buffer nodes, where the full events are built and, if satisfying trigger criteria, sent to permanent storage.

Timing synchronization for these DCMs is handled by chains of Timing Distribution Units (TDU) consisting of one master node (MTDU) and several slave nodes (STDU). A schematic describing the data stream of the DAQ system is shown in fig 2.13.

Every beam spill at Fermilab is time stamped with and synchronized to an external wall clock. The spill information with the high resolution time

stamp is then transmitted to the far detector site, where the hit buffers are searched for any hit data that overlaps with the beam spill and the results are stored through a data logger system to permanent storage. In addition to the beam spill information, the full unfiltered detector data stream gets examined, reconstructing it, identifying specific hit topologies and issuing triggers corresponding to these topologies. The data is held in a circular buffer, where the oldest data is continually overwritten with the most recent one.

When the trigger system arrives at the decision for a particular time window of the readout data, the trigger system instructs the DAQ to search the buffered data for the time interval of interest. Once the data is located it is copied out of the active buffer and sent to the final state of the event building where it is combined with the data from other buffers and recorded to disk.

More about the intricacies of the NOνA DAQ can be found in [55–57].

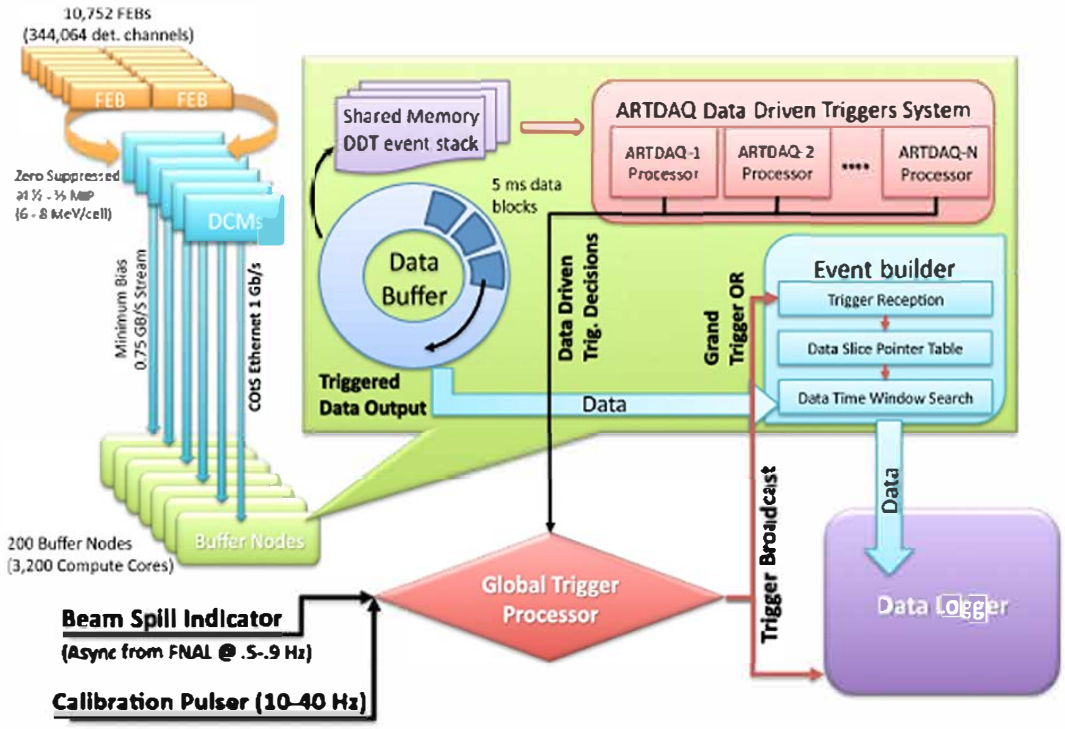

Figure 2.13: A schematic overview of the FD DAQ system.

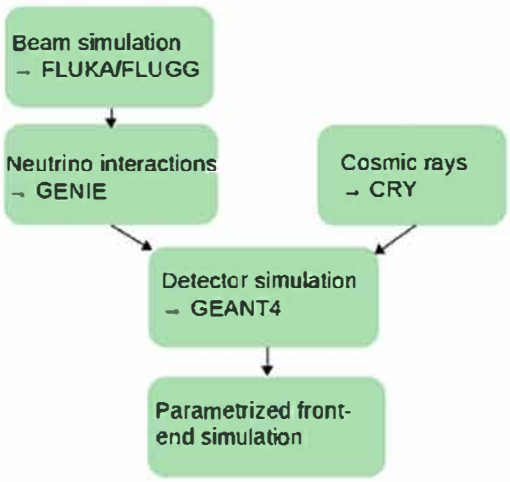

Figure 2.14: A schematic of the simulation chain for the NOνA experiment from [63].

2.4 Simulation Chain

The NOνA simulation, schematically summarized in fig. 2.14, begins with the production of neutrinos in the NuMI beamline.

The FLUGG [58] package combines FLUKA [59, 60], which simulates the interaction of the protons with the target and subsequent interactions of the secondaries, with GEANT4 [61], which handles the geometry description of the target and decay pipe. The output is a flux file consisting of neutrinos (flavor, energy, and momentum) at the point of creation from their parents. Flux files are created for both the RHC and FHC beam configurations. Additional weights correct the latter via a a framework created specifically for the NuMI beam called PPFX [62], which is based on several hadron production experiments.

Furthermore, GENIE [64] simulates the neutrino interactions inside the detectors and their surroundings starting from the predicted flux and detector geometry files. GENIE combines neutrino cross-section data and theoretical models to determine if the neutrinos interact, the vertex position and type of interaction, and outputs a four-vector for each particle produced.

Nevertheless, the default GENIE settings underestimate the visible hadronic energy reconstructed in the detectors, and NOνA's simulation corrects this by activating an additional interaction within GENIE: the meson exchange currents (MEC), explained in section 1.5. This process consists of a neutrino interacting with a nucleon coupled to another nucleon via a meson. Meson exchange currents are well-known from electron scattering, but no contemporary model is able to correctly predict current neutrino data. Therefore, within NOνA's simulation this interaction is weighted to match the observed near detector data. More details about this tune can be found in [33]. Since the far detector is on the surface, cosmic rays are a significant background which get simulated via CRY [65].

Finally, GEANT4 propagates the particles produced by either GENIE or CRY through the detector geometry, and generates their energy depositions in the detector cells. GEANT4 is capable of simulating optical photon processes, generating scintillation light and propagating it inside the cell, through the fiber, and to the APD, but this is very time consuming. Therefore, custom NOνA algorithms [66] take care of these final steps by transporting the light from the liquid to the APD and simulating the FEB response to the APD

signals. The end product is a ROOT [67] output file in the same format as data files with additional truth information ready to be used in downstream reconstruction.

2.5 Event Reconstruction

NOνA collects data in 550 μs readout windows for the entire detector. However, physics interactions take place within a shorter time period. In the FD the primary challenge is to separate 50-70 cosmic rays within the readout window, while the ND is expected to separate around 5 neutrino interactions within the 10 μs beam window. Event reconstruction is the process of converting the electronic signals recorded by the FEBs into a set of measurements associated with the particles passing through the detector. The full chain of the reconstruction is schematically summarized in fig. 2.15. In this section, the different steps are explained that organize an ensemble of hits into tracks, prongs or noise hits, assigning a vertex per interaction. Details about the NOνA reconstruction can be found in [68] and the most recent changes that are part of the frozen version used in this thesis, internally called "production 5" or "prod5", are listed in [69].

2.5.1 Hits

The basic unit of detection in the NOνA framework is the raw hit. It stores pixel information (plane, cell), a time stamp and ADC value. Several hits are grouped by trigger type, detector, run and subrun before stored in

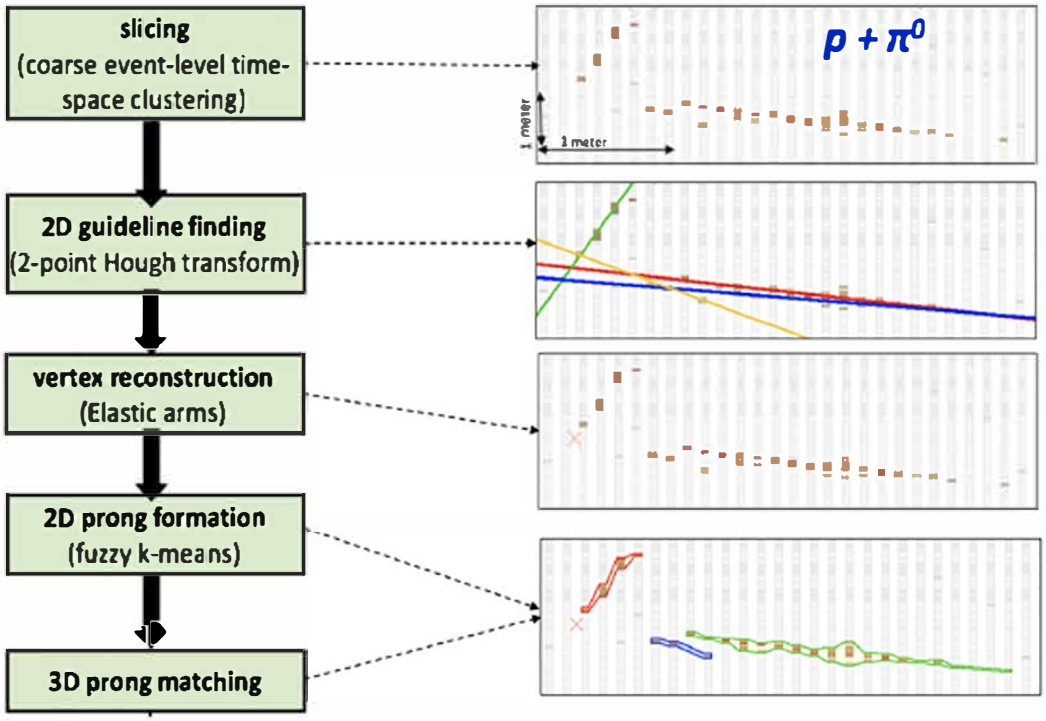

Figure 2.15: Flowchart of the reconstruction algorithms from [70].

data files. Simulation files contain the same attributes as well as how the events were generated. Information about calibration, geometry, beam and detector conditions gets incorporated to convert raw hits into calibrated hits.

2.5.2 Slices

A slice is a group of hits that are close in space and time. The newly developed Time Density Slicer (TDSlicer), thoroughly described in [71], replaced the older Slicer4D in production 5. This new algorithm finds local maxima in the density of time-of-flight corrected hit times. A reconstructed 4D cluster gets generated in the following three steps:

- Identify centroids, i.e. local maxima in the density of hits. In order to accomplish that, the density of hits around each hit is calculated within a view (xzt or yzt):

$$\rho_i = \sum_j exp(-d_{ij}^2/\tau^2), \tag{2.5}$$

  where d_{ij} is the Euclidean distance between two points and τ is a configurable scale parameter set to 16 for the ND and 80 for the FD, which is related to their timing resolution. After evaluating the density for every hit, an isolation score is calculated using

$$\delta_i = \min_{j|\rho_j > \rho_i} (d_{ij}), \tag{2.6}$$

  which is the minimum distance to a hit of higher density. The centroids are the hits with high density and isolation, see 2.16.

- Create 3D clusters in xzt and yzt determined by grouping nearby hits with centroids using Prim's algorithm [72], a minimally connected spanning tree.

- 3D clusters of the two different views are merged into 4D clusters in $xyzt$. Iteratively, the best pair of 3D slices is combined to make a 4D slice and then deleted from the list of available 3D slices to pair.

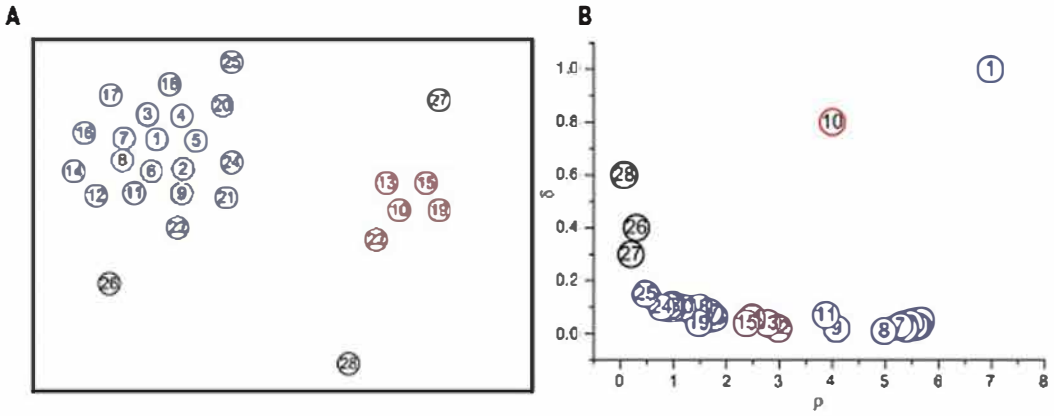

Figure 2.16: On the left a scatter plot of potential data to be clustered. For every point the density, eq. (2.5), is calculated and the numbers correspond to the ordering of the points from high to low in density (1-28). The isolation, eq. (2.6), is plotted on the right, which is the minimum distance to a point of higher density. Though points 2-9 have a higher density than point 10, they are close to point 1, and thus score low in isolation. Point 10 is the most dense point in the smaller cluster. Points 1 and 10 are clearly identified as centroids in this example featuring high density and isolation scores. Points 26, 27, and 28 have too great an isolation to be included with any cluster and too low a density to form their own cluster and are thus treated as noise. From [71].

2.5.3 Vertex

After slicing, the next step is to identify lines in each slice using a modified Hough transform algorithm [73]. Then the Hough lines are used as seeds to determine the global 3D vertex for the slice under the assumption that all activity in the slice has a common origin.

The modified Hough transform algorithm is applied to each individual detector view separately, taking as input pairs of points and calculating a straight line passing through them. Each of these lines contains a unique point that is closest to the origin and has polar coordinates (ρ, θ). Conversely, a point uniquely determines a line in this way and therefore the line itself is parametrized by (ρ, θ). Each line is weighted by the Gaussian smear vote

$$vote = e^{-\left(\frac{\rho-\rho_0}{2\sigma_\rho}\right)^2} e^{-\left(\frac{\theta-\theta_0}{2\sigma_\theta}\right)^2} \quad \text{with} \quad \sigma_\rho = \frac{3}{\sqrt{12}},\ \sigma_\theta = \frac{3}{d\sqrt{6}}, \tag{2.7}$$

where d is the distance between two hits. The dominant lines are those with the highest vote. To identify new lines in the Hough space, an iterative method is employed. First, the hits from the dominant Hough lines are removed, hence drastically reducing the noise for the next iteration in the Hough space, see fig 2.17. This continues until no more peaks can be found above a certain threshold.

Furthermore, the Elastic Arms algorithm [75] uses the Hough lines in order to find vertex candidates. From the intersections of Hough lines, a series of "arms", which are vectors pointing away from the vertex, are constructed and adjusted to better represent the trajectories. Minimizing an energy cost

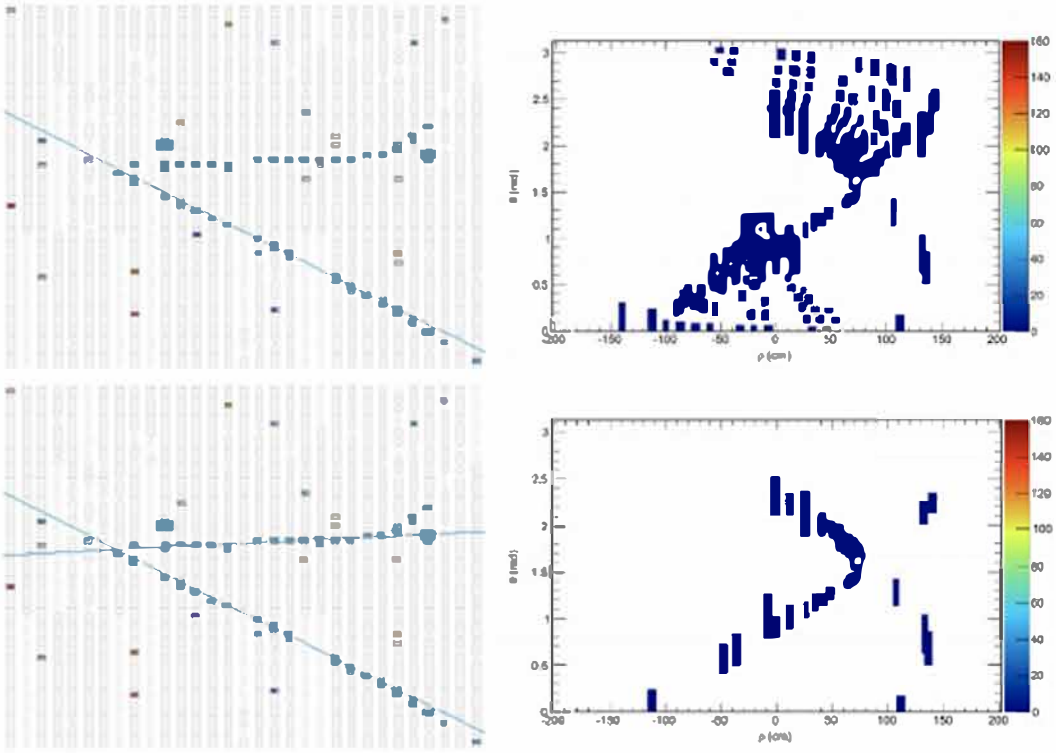

Figure 2.17: First row of event display (left) and Hough space (right) correspond to the first iteration of the algorithm, the second row corresponds to the second iteration, where hits from the 1st Hough line have been removed. From [74].

function the optimum vertex is found. The customized NOνA Elastic Arms algorithm includes additional terms to allow for gaps between the vertex and first energy depositions. Only one vertex per interaction gets reconstructed so far, albeit work and intentions of changing the reconstruction to allow for multiple vertices.

2.5.4 Prongs

Moreover, the vertex is then used as input for the possibilistic "fuzzy k-means" algorithm [76, 77] that produces prongs, which are a collection of cell hits with a starting point and direction. A prong is the reconstruction object that best suits the characteristic of a particle depositing energy in the form of a hadronic or electromagnetic shower.

"Possibilistic" means that not all hits within a slice are required to be part of a prong, and "fuzzy" means that a hit can belong to several prongs, and the total number of prongs is not predetermined. The fuzzy-k algorithm makes use of the angular distribution of energy depositions with respect to the vertex to find peaks that would correspond to different prong centers. Hits are then assigned a degree of membership to each prong based on their distance from the center.

The iterative process avoids duplicating prong centers, and terminates when all hits have been matched with a prong or a maximum number of clusters has been identified. At the end of the prong formation stage there is a set of 2D prongs for each x- and y-view. Finally, these 2D prongs are matched

and merged into 3D prongs based on their geometry and energy distribution using a Kupier metric [70].

2.5.5 Tracks

For particles that are more track-like instead of shower-like (good prong candidates), different reconstruction algorithms need to be employed.

The Kalman-filter algorithm [78] is used to reconstruct the particle trajectory by iteratively collecting hits starting from the downstream end of the detector where the tracks on average are more separated from each other. Slice hits are added to the track and the propagation is continued in the upstream direction until no more hits satisfy the filter separation and probability conditions.

The Kalman-filter technique works well for charged particles that do not shower in the detector, like muons produced in CC interactions, which lose energy via ionization, and leave straight tracks with occasional small kinks. Cosmic muons are particularly well reconstructed using the "Cosmic track" algorithm [79], which applies a sliding window assuming downward-going single-track energy depositions. The different types of tracks are all initially reconstructed separately for each x- and y-view, and those 2D objects get matched based on the overlap in the z-direction.

2.6 Calibration

The calibration of the detectors [80] falls into two categories: energy and timing calibration. The calibration guarantees that the amount of digitized amplitude recorded for each cell can be compared independent of when and where the activity occurred, and can be expressed in units of energy [GeV]. The timing calibration corrects time offsets between the data concentrator modules (DCMs) so that energy depositions in different cells from the same particle are properly correlated in time.

There are three main steps that constitute the energy calibration chain:

- **Attenuation calibration:** The first step is to correct for the attenuation of light in the WLS fiber, which is performed on a cell-by-cell basis. Hits from cosmic ray muon tracks in three neighboring cells, called tricell hits, are used for calibration. Tricell hits, see fig. 2.18, are defined as cell hits having an adjacent hit in the two neighboring cells. This requirement ensures that the path length inside of the central cell can be determined with accuracy and decreases the probability of using noise hits. A fit of a parametric function to the cosmic data will then establish the corrections to be used for any hit in that cell in other data samples.

- **Drift calibration:** This calibration type addresses how the FEB response changes as a function of time. Possible unidentified causes could

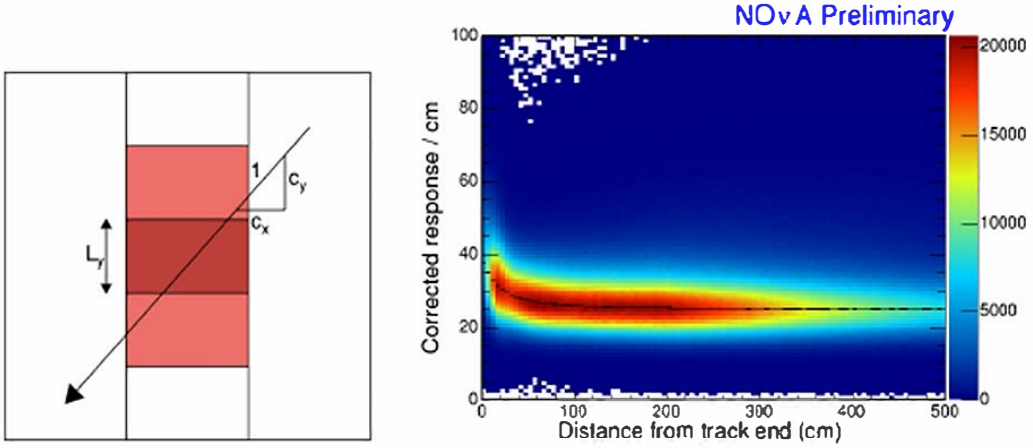

Figure 2.18: Left: Schematic of a tricell hit. The dark-red cell is selected because of its cell neighbours having hits as well.
Right: Each entry in the histogram is from a tricell hit on a stopping muon track. The y-axis shows the path normalized attenuation corrected detector response. The x-axis shows the distance to the stopping point of the muon track. The black fit curve shows the mean of a fit to the peak of the attenuation corrected detector response at 100-200 cm distances from the track end. Hits within the track window are used for the absolute calibration. Both from [81].

be: changes in the APD gain, variation of temperature, aging of the scintillator and changes in the electronics. Here again cosmic muon rays are used to asses these corrections by comparing the variations in response across different periods of data taking. Periods are intervals of time characterized by uniform running conditions. A new period is started for each major change to the running conditions such as a horn current change, a long shutdown, target replacement, etc.

- **Absolute calibration:** After cell-to-cell differences are removed, an absolute scale for the energy has to be established in order to translate a hit's energy deposition into a reconstructed GeV. Cosmic rays are used as a source of consistent energy deposits across the detectors as the energy deposition of stopping muons is well understood from the Bethe-Bloch formula. The average cosmic muon energy loss varies by only 1.8% in the 100-200 cm region from the end of the track. This range sits right on the minimum energy loss region. Tricell hits within that distance to the end of the track are selected, see fig 2.18. A scale factor is then determined that translates the energy units into GeV.

Chapter 3

Measurement of Neutral Pion Production in Neutral Current Interactions

This work aims to measure the cross-section of anti-neutrino induced neutral-current π^0 production using the NOvA near detector. An anti-neutrino undergoing a neutral-current interaction with at least one π^0 above detection threshold in the final state is the signal of the NC π^0 production analysis:

$$\overset{(-)}{\nu} N \rightarrow \overset{(-)}{\nu} \pi^0 X. \tag{3.1}$$

The target nuclei in NOνA are predominantly carbon (66.7% by mass), chlorine (16.1%) and hydrogen (10.8%), with small contributions from titanium (3.2%), oxygen (3.0%) and other nuclei. The goal is to measure a flux-averaged differential cross-section in π^0 momentum (p_{π^0}) and π^0 angle with respect to the beam direction (θ_{π^0}) with reverse horn current NuMI beam data:

$$\left(\frac{d^2\sigma}{d\theta_{\pi^0}\, dp_{\pi^0}}\right)_i = \frac{\sum_j U_{ij}^{-1} N_{\pi^0}(\theta_{\pi^0}, p_{\pi^0})_j}{N_t\ \phi\ \epsilon(\theta_{\pi^0}, p_{\pi^0})_i\ \Delta\theta_i\ \Delta p_{\pi^0 i}}, \tag{3.2}$$

where the indices j and i stand for reco and truth, respectively, ϕ is flux, ϵ is efficiency and N_t is number of targets.

3.1 Motivation

Interactions of neutrinos with nuclei at neutrino energies around 1 GeV, and the resulting final states, are a challenge to describe theoretically as well as to measure experimentally. As a consequence, systematic uncertainties in neutrino interaction cross-sections are typically among the largest uncertainties affecting long-baseline neutrino oscillation measurements, even with the two-detector approach. Today's neutrino oscillation experiments as well as

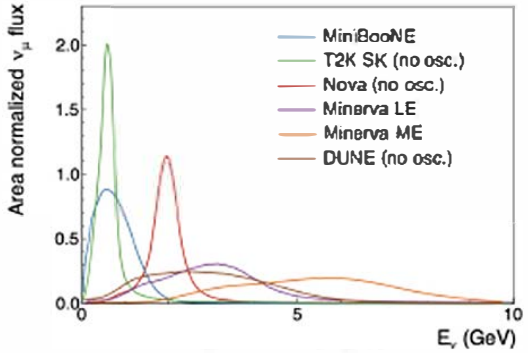

Figure 3.1: Area normalized ν_μ flux for the different energy ranges of current and future experiments, from [82].

the next generation experiments will profit from sophisticated neutrino cross-section measurements within their neutrino energy region, see fig. 3.1.

Specifically within the NOνA context, fig 3.2 depicts the variety of uncertainties that impact the measurement of oscillation parameters. With more NuMI beam data the statistical uncertainty will keep shrinking and systematic uncertainties will gain in importance. NOνA is uniquely positioned to measure the 2 GeV energy region, and with the world's most powerful neutrino

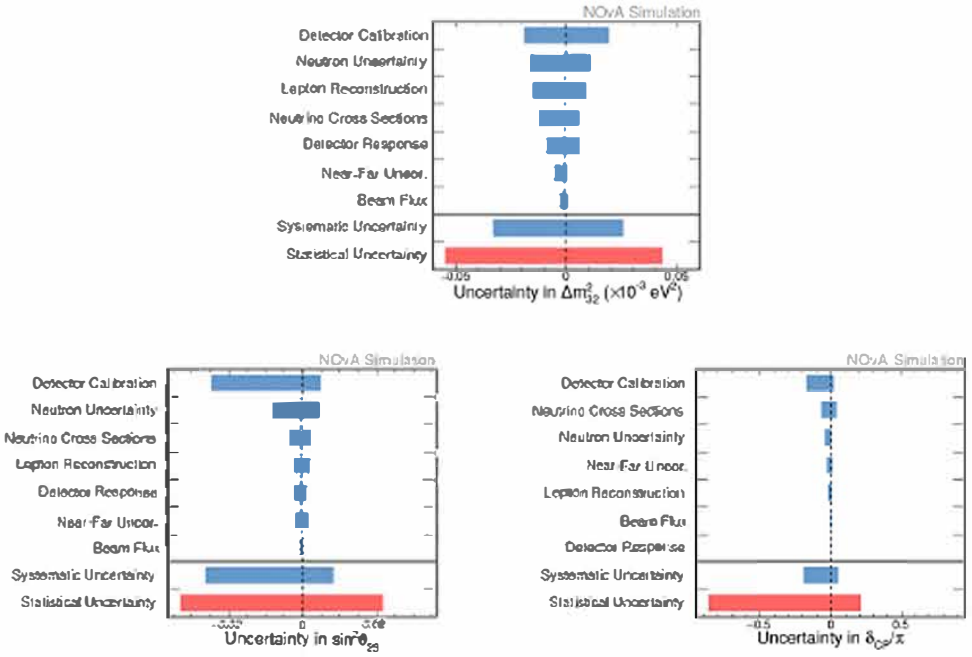

Figure 3.2: Simulated effects of different systematic categories on the oscillation parameters estimation in the joint FHC+RHC ν_μ+ν_e fit. Evaluated at the best fit point: $\delta_{CP} = 0.82\pi$, $\theta_{23} = 0.568$, $\theta_{13} = 0.085$, $\Delta m^2_{32} = 2.40 \times 10^{-3}\text{eV}^2$.

beam it is NOνA's responsability to measure several neutrino cross-sections as accurate as possible. This analysis aims to reduce systematic uncertainties for the oscillation measurement, in particular for the ν_e appearance channel.

When a π^0 is misidentified as an electron, this final state signal process for the ν_e appearance channel

$$\nu_e \, N \rightarrow e \, X \tag{3.3}$$

is indistinguishable from this background process

$$\overset{(-)}{\nu} \, N \rightarrow \overset{(-)}{\nu} \, \pi^0 \, X, \tag{3.4}$$

which is the signal for this study. Neutral pions decay 98.8% of the time into:

$$\pi^0 \rightarrow \gamma + \gamma.$$

Therefore the signature for this analysis is two electromagnetic tracks slightly away from the vertex. Scenarios in which one of the two photons is missing or is hard to reconstruct, make a π^0 decay look like a single electromagnetic shower in the detector instead of two, which is hard to distinguish from an electron. Examples of these scenarios are overlapping photons (with small opening angle) or one out of the two photons depositing most of its energy in just a few cells, which can be caused by one of the photons being low energy (asymmetric decay) or its trajectory being parallel to the detector cells.

The decay

$$\pi^0 \rightarrow \gamma + \gamma + \gamma$$

or any odd number of photons, is forbidden by mandatory conservation of charge conjugation (C-symmetry) in electromagnetic interactions. The C-parity of the π^0 is +1, while the C-parity of a system of n photons is $(-1)^n$. The second largest decay mode is the Dalitz decay (BR $= 1.17 \cdot 10^{-2}$)

$$\pi^0 \rightarrow \gamma + e^- + e^+$$

where a photon internally converts to a real lepton pair. The third largest is the double-Dalitz decay (BR $= 3.3 \cdot 10^{-5}$),

$$\pi^0 \rightarrow e^- + e^+ + e^- + e^+$$

with both photons undergoing internal conversion which leads to further suppression of the rate. The fourth largest established decay mode is the loop-induced and additionally helicity-suppressed leptonic decay mode

$$\pi^0 \rightarrow e^- + e^+$$

with Branching Ratio $= 6.46 \cdot 10^{-8}$.

3.2 Previous Measurements

This section summarizes previous measurements of neutrino induced neutral-current π^0 production in no particular order.

MiniBooNE [83] measures the first absolute cross section for NC π^0 production on CH_2 target using a neutrino beam with a mean energy of 808 MeV:

$$\sigma(\nu) = (4.76 \pm 0.05(\text{stat.}) \pm 0.76(\text{syst.})) \times 10^{-40} \text{cm}^2/\text{nucleons}$$

and anti-neutrino beam with a mean energy of 664 MeV:

$$\sigma(\overline{\nu}) = (1.48 \pm 0.05(\text{stat.}) \pm 0.23(\text{syst.})) \times 10^{-40}\text{cm}^2/\text{nucleons}.$$

NOνA [37] uses near detector data taken in neutrino mode from 2014 to 2019, which accounts for 8.09×10^{20} POT, to report a flux-averaged cross section of:

$$\sigma(\nu) = (2.55 \pm 0.012(\text{stat.}) \pm 0.34(\text{syst.})) \times 10^{-39}\text{cm}^2/\text{nucleons}.$$

MicroBooNE [84] uses the Booster muon neutrino beam with a mean energy of 800 MeV to measure neutral-current single π^0 production on argon in three distinct ways:

- for the semi-inclusive NC:

$$\sigma(\nu) = (1.243 \pm 0.185(\text{syst}) \pm 0.076(\text{stat})) \times 10^{-38}\text{cm}^2/\text{Ar},$$

- exclusive NC $\pi^0 + 1p$:

$$\sigma(\nu) = (0.444 \pm 0.098(\text{syst}) \pm 0.047(\text{stat})) \times 10^{-38}\text{cm}^2/\text{Ar},$$

- exclusive NC $\pi^0 + 0p$ processes:

$$\sigma(\nu) = (0.624 \pm 0.131(\text{syst}) \pm 0.075(\text{stat})) \times 10^{-38}\text{cm}^2/\text{Ar}.$$

T2K [85] uses the ND280 detector to measure an inclusive neutral-current π^0 production with a muon-neutrino beam peaked at 0.6 GeV:

$$\sigma(\nu) = (2.145 \pm 0.284(\text{syst}) \pm 0.109(\text{stat})) \times 10^{-40}\text{cm}^2/\text{nucleons}.$$

3.3 Simulation, Reconstruction and Data Set

The simulation and reconstruction used in this analysis are identical to that used for the 2020 oscillation results [20]. The analysis is performed using NOνA's CAF Analysis framework taking Common Analysis Files (CAF) as input.

All the plots for this analysis are produced using the cafana definition denoted:

`prod_caf_R20-11-25-prod5.1reco.a_nd_genie_N1810j0211a_nonswap_rhc_nova_v08_full_v1`

which contains 202672 files accounting for a total of $5.0668 \cdot 10^{21}$ protons on target, $2.5 \cdot 10^{16}$ POT per file.
The expected sensitivity is kAna2019RHCPOT $= 12.331920 \cdot 10^{20}$, so all the histograms below have been scaled to that number: $0.243 = \frac{12.3319 \cdot 10^{20}}{5.0668 \cdot 10^{21}}$.

3.4 Signal Definition

The signal for this channel is any $\overset{(-)}{\nu}$ NC interaction with at least one π^0 with kinetic energy above a certain threshold in the final state (see subsection 3.6.6 for more details on the kinetic energy threshold). This includes neutral pions exiting the target nucleus after intra-nuclear Final State Interactions (FSI), but excludes those created from particles after leaving the target nucleus. Below, in figures 3.3 and 3.4, two event displays of the same clean

signal event can be seen, where the hadrons resulting from the interaction are low energy and do not get mixed with the energy deposits of the photons.

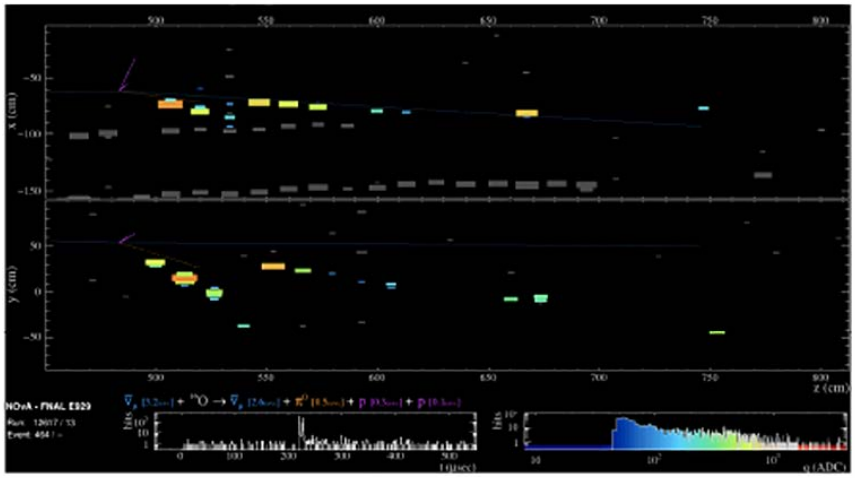

Figure 3.3: The true direction of the particles is depicted with colored, dotted lines, which match with the particles' colors in the process at the bottom left. In parenthesis are the kinetic energies of the particles.

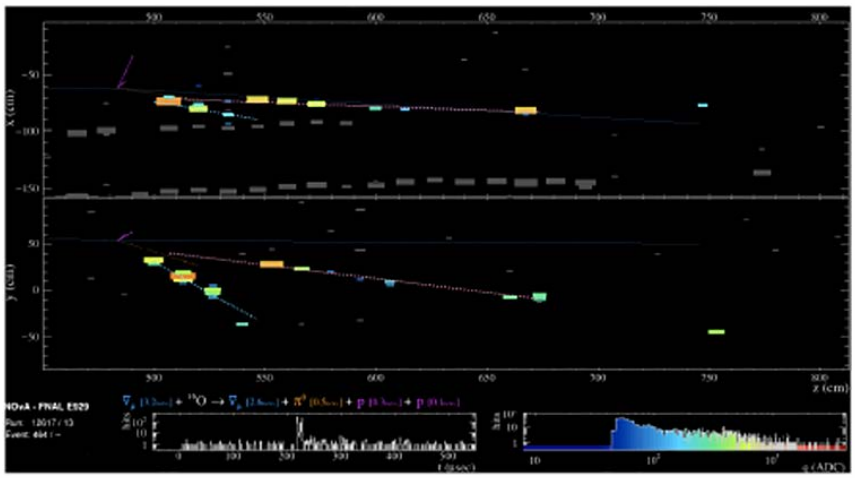

Figure 3.4: The two reconstructed prong lengths are depicted with wider, dotted lines in addition to the true particle directions.

The z-axis represents the beam direction and the two views within the

same event display correspond to the top and side view of the detector. The small colored rectangles (hits) are the particle's energy deposits that translate into scintillation light within the NOvA cells. The amount of light collected is proportional to the energy deposited in each cell and the ADC scale at the bottom maps the different colors of the rectangles with different ADC counts. In particular, the redder the color, the higher the energy deposited and the bluer the smaller. The gray rectangles correspond to hits from other slices occurred at a different time.

More signal event displays can be found in appendix A, where a variety of reconstruction features are highlighted.

3.5 Backgrounds

Given the signal definition the background, which is everything non-signal, can be organized into four different categories:

- CC interactions without neutral pions in the final state,
- CC interactions with at least one neutral pion in the final state,
- NC interactions without neutral pions in the final state,
- NC interactions with all neutral pions in the final state below threshold.

Different examples of background event displays can be found in appendix B. The function of this categorization will become more apparent later on, but for

now it is a labeling scheme, which enables differentiation between an otherwise amorphous ensemble of events.

3.6 Event Selection

The first step in the analysis is to develop a set of selection criteria that obtains a clean sample of neutrino neutral-current interactions with at least one π^0 in the final state above threshold from the total sample of simulated interactions. Events with any activity in the muon catcher (where active planes are interlaid with steel planes) are not considered in this analysis. We start by simply selecting only events with 2 shower-like tracks (called prongs). The NOvA reconstruction software automatically orders the prongs by amount of energy, therefore the 1st prong will always be the most energetic or leading prong.

All events are required to pass a StandardSpill Cut, which only selects NuMI spills that are acceptable for analysis purposes. Qualitatively this data quality requirement imposes a good beam performance, acceptable state of the detector electronics and quantitatively it corresponds to this set of conditions:

- spill POT $> 2 \cdot 10^{12}$
- $-202 <$ horn current < -198
- $-2.0 <$ horn x and y position on target < 2.0
- $0.57 <$ Beam width in x and y < 1.58

- time delay between NuMI time stamp and spill < 0.5 ns
- fraction of hits occurring outside the beam peak < 0.45
- number of missing DCMs $= 0$

There are two different types of requirements that will constitute the event selection and they can be classified based on their goal:

- requirements that ensure a good quality of events, with good quality prongs (eg. Constraint on Number of Hits (subsection 3.6.5), neutral pion kinetic energy threshold (subsection 3.6.6)), which will be determined by ensuring a good quality reconstructed invariant mass.
- requirements that minimize the systematic and statistical uncertainties on the total cross-section (eg. Fiducial Volume (subsection 3.6.1), Containment Volume (subsection 3.6.2) and MuonID Constraint (subsection 3.6.3).

Subsequently follow details to elaborate on the latter strategy to determine selection criteria that minimize both the systematic and statistical uncertainties on the total cross-section:

$$\sigma = \frac{N_{sel,\,Data} - s \cdot N_{bkg,\,MC}}{\Phi \cdot \epsilon \cdot N_{target}}, \tag{3.5}$$

where $N_{sel,\,Data}$ is the number of selected data events, $N_{bkg,\,MC}$ is the estimated number of selected MC background events, Φ is the total flux, N_{target} is the

number of targets. The efficiency ϵ is:

$$\epsilon = \frac{N_{sel,\,signal}}{N_{signal}} \quad \text{and} \quad s = \frac{POT_{Data}}{POT_{MC}} \tag{3.6}$$

is the ratio of the exposure in data to the exposure in the simulation.

The figure of merit to optimize in this case is the fractional uncertainty on the cross-section. The fractional uncertainty on the total cross-section may be plotted as either a function of a variable (eg, vertex position) or as a function of a cut value. Ignoring uncertainties on the flux and the number of targets (weakly depending on the selection criteria), and correlations between background estimates and efficiency, the fractional uncertainty on the cross-section is:

$$\frac{\delta\sigma}{\sigma} = \sqrt{\frac{(\delta N_{sel}^{stat})^2 + (\delta N_{bkg}^{stat})^2 + (\delta N_{bkg}^{syst})^2}{(N_{sel} - N_{bkg})^2} + \left(\frac{\delta\epsilon}{\epsilon}\right)^2}, \tag{3.7}$$

where the statistical uncertainty on the number of selected events is negligible.

Further details on the derivation of eq. 3.7 and the computation within the NOνA framework can be found in [86].

In order to ensure proper reconstruction of the events in terms of energy, direction of the prongs and vertex location, the need of a fiducial and containment cut is strictly necessary. Unfortunately, these two cuts have not been optimized for this analysis and the values have been taken from precedent work done by Alan Cedeno [87].

3.6.1 Fiducial Volume

The reconstructed vertex of the event (demarked by a cross in the event displays) is required to be within a certain volume. This volume's name is fiducial volume and is given by this set of coordinates:

$$V_x \in [-80, 120], \quad V_y \in [-148, 60], \quad V_z \in [225, 950], \tag{3.8}$$

being $V_{x,y,z}$ the coordinates of the reconstructed vertex.

3.6.2 Containment Volume

In addition, the two prongs are not allowed to leave a certain part of the detector, which means that the end of the prongs has to be contained inside this volume:

$$stop_x \in [-160, 120], \quad stop_y \in [-180, 155], \quad stop_z \in [200, 1200], \tag{3.9}$$

being $stop_{x,y,z}$ the furthest hit away from the beginning of the prong for each coordinate.

3.6.3 MuonID Constraint

In order to reduce background events with one muon in the final state, mainly $\overset{(-)}{\nu}_\mu$CC events, a Muon Identifier (MuonID) has been employed. This variable identifies muon-like tracks using a Convolutional Visual Network (CVN) trained to distinguish between 5 different types of particles interacting in the near detector, which is where the training's "5 label" name stems from. CVN is an image recognition technique which uses the map of event hits as an input.

Within NOνA this technique is very powerful and has been deployed to recognize full neutrino interactions or singular prongs. In this case, the training was done on single prongs, more details can be found in [88]. The CVN algorithm calculates a MuonID for each prong, but only the highest score gets saved for each event. The assumption behind this procedure is that there will only be one muon at most in the final state per event and the prong with the highest MuonID score is the best muon candidate. We place a MuonID constraint to diminish the amount of events with muons in the final state, so that events with low MuonID values are kept and the ones above the constraint are discarded.

This cut was optimized looking at purity and efficiency of possible cut values of this variable, which will be explained within this section. Nevertheless, there are many figures of merits that could have been used and this is just one options within many. Figure 3.5 shows the highest value of the MuonID per event. The choice of requiring events to have a MuonID < 0.14 is somewhat arbitrary since the plot on the right of fig. 3.5 shows no maximum for the efficiency or purity. We decide on a MuonID < 0.14 requirement, because the efficiency almost reaches it's highest value at that point and on the left plot we see the signal going to zero after that. Furthermore, a prong length cut of 5m is in place for all prongs, since the CVN 5lMuonID was not trained on longer than 5m long muons.

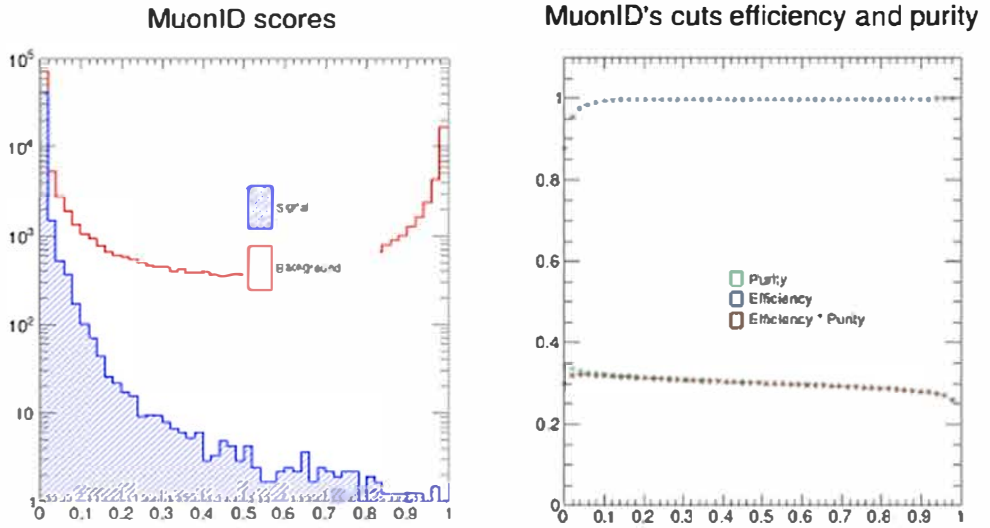

Figure 3.5: Left: "5 label" MuonID variable for signal and background, one entry per event. Right: Efficiency, purity and their product computed for different requierement values of MuonID. The requirement includes the events with lower MuonID values.

3.6.4 Electromagnetic Shower ID

In order to improve our selection, we want to use an electromagnetic shower identifier (EMID) which will reduce the amount of protons, neutrons and charged pions within our sample. A binary network was trained by Fan Gao [89] on individually simulated single particles (electrons, photons, protons and charged pions) to separate these into two categories: electromagnetic shower-like or not. Unlike the MuonID variable, the EMID will be assessed and displayed for the 1st ($EMID_1$) and 2nd prong ($EMID_2$)[1]. By signal events we mean those with all of the following characteristics:

[1]For the majority of this writing the subscript X_1 will be associated with a variable X of the 1st prong and X_2 for the second prong.

- only two reconstructed 3D prongs per event;
- events have to pass MuonID, Containment and Fiducial requirements;
- from the truth information of the event, the event has to:
  - correspond to a neutral current interaction,
  - contain at least one π^0 in the final state.

The background events still have to fulfill the first two requirements listed above but fail the third one. Background can be classified into 4 different types: CC interactions with or without a π^0 in the final state and NC interactions without a π^0 or without a π^0 above threshold, which is discussed in subsection 3.6.6.

The plots in fig. 3.6 show the distributions for signal and background events for the EMID variable of the 1st prong, respectively. Within the CAFAna framework each prong can be assigned a particle label corresponding to the best matched truth particle [2].

[2]The truth matching algorithm readily available within the CAFAna framework only allows for one type of matching between reconstructed prongs and true simulated particles. The way it pairs truth and reco information is solely based on amount of energy deposited, in other words, it checks what is the true particle's identification number responsible for the highest ADC value within a prong summing over all hits. For this analysis a different truth matching algorithm would have been more convenient, given that around 33% of signal events have both prongs matched to the same true particle. An effort was undertaken to develop a different truth matching algorithm based on number of hits corresponding to a simulated particle, but after some rough investigations, the differences weren't very encouraging and the effort was abandoned.

This breakdown into the different particle types demonstrates that the EMID variable is a very powerful discriminator for this analysis because it clearly differentiates protons and gammas. It will also help to further diminish the amount of muons which still slip through the MuonID cut. Nevertheless, a different variable will be needed to diminish the amount of electron prongs present in the background.

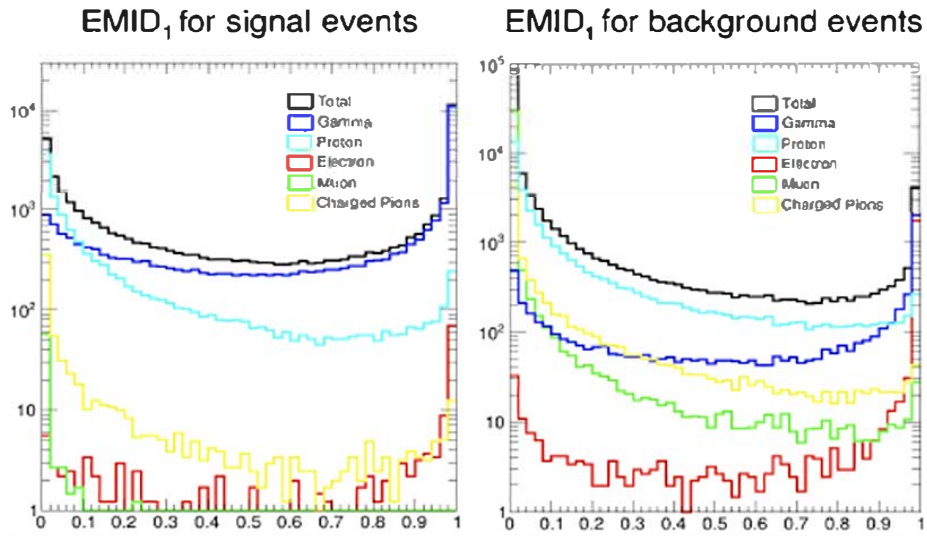

Figure 3.6: EMID variable of the 1st prong for signal (left) and background events (right). This variable clearly separates proton from photon prongs.

Unfortunately, the second prong's EMID variable is not as useful to distinguish photons and electrons from other particles. The second prong is less energetic by definition, so it is shorter and harder to identify as an electromagnetic shower. The corresponding distributions for the second prong can be found in fig. 3.7, which both point out the challenge of removing the dominating contaminating particle: protons.

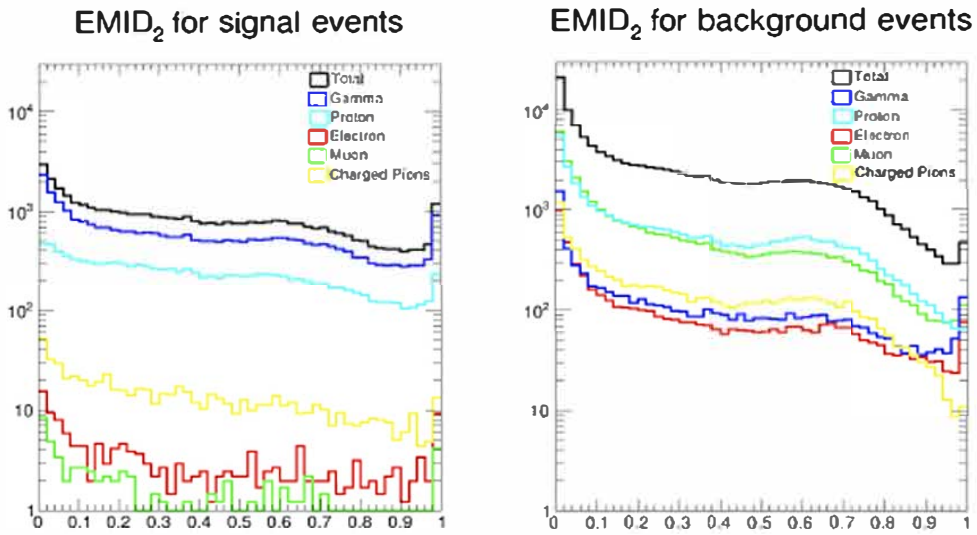

Figure 3.7: EMID variable of the 2nd prong for signal (left) and background (right) events.

It is important to point out the relation between the 1st prong and 2nd prong. Since they share the energy of the decaying π^0, the more energetic the first prong is the less energetic the 2nd prong will be. Figure 3.8 shows that signal events in which both prongs are identified as gamma particles [3] with high EMID scores in the first prong still have a variety of EMID scores for the second prong. For signal events whose prongs are not required to be gamma particles, the majority of events have a high $EMID_1$ and low $EMID_2$. The various ways in which the reconstruction fails predominantly affect the quality of the second prong: the two gammas from the π^0 decay overlap and get reconstructed as a single prong, one of the photons produces just a few hits

[3]For the rest of this writing the "signal $\gamma\gamma$" events are those passing the signal requirements and both of whose prongs are primarily composed of photons' energy depositons (from truth information).

and does not get reconstructed or other particles created within the interaction overlap with one or both of the gamma prongs.

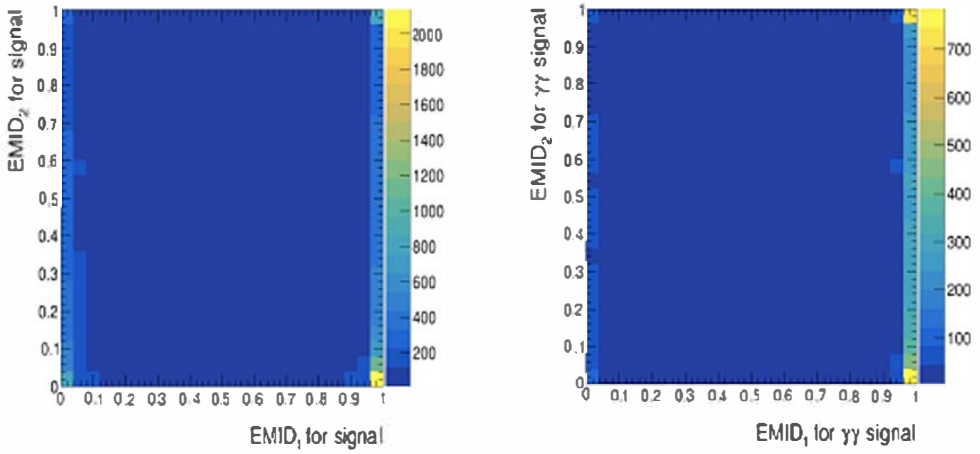

Figure 3.8: EMID scores for signal (left) and for signal $\gamma\gamma$ events (right).

3.6.5 Constraint on Number of Hits

The reconstructed object called "prong" already requires a minimum amount of two hits, but in order to identify a prong as a gamma we want to ensure a good quality prong and pose a more stringent requirement on the minimum number of hits per prong. To optimize the constraint on the number of hits (NHits) of both prongs, we investigate how the events are distributed in the EMID variable against the NHits for the two prongs.

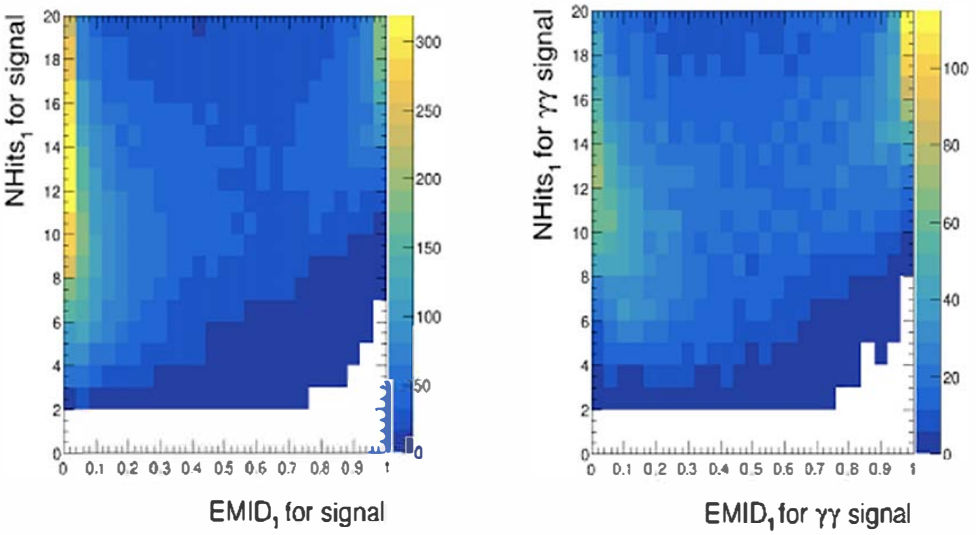

Figure 3.9: $\mathrm{NHits_1}$ vs $\mathrm{EMID_1}$ for signal (left) and signal $\gamma\gamma$ events (right).

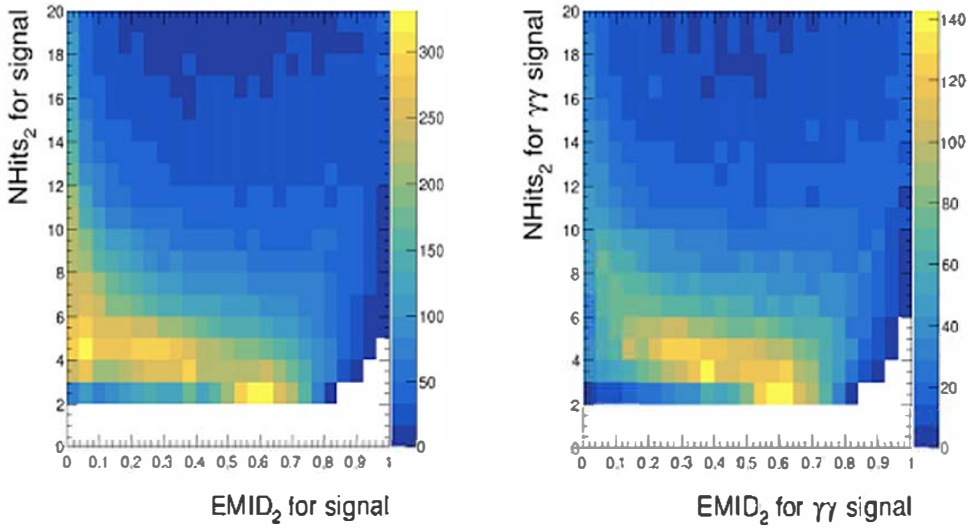

Figure 3.10: $\mathrm{NHits_2}$ vs $\mathrm{EMID_2}$ for signal (left) and signal $\gamma\gamma$ events (right).

From the first set of figures 3.9 we learn that even a $\mathrm{NHits}_1 > 8$ constraint would be a viable option since most of the events with high EMID_1 scores have at least 8 hits or more. A population of low EMID_1 values is visible in the left plot, which consists mostly of protons as we saw in fig. 3.6. In figure 3.10 we see a more complicated scenario in which a considerable amount of events that cluster around higher EMID_2 values have very few hits.

In order to decide on the minimal number of hits required for both prongs, we compute the invariant mass

$$M_{\gamma\gamma} = \sqrt{2E_1E_2\left(1 - \frac{\vec{p}_1 \cdot \vec{p}_2}{|\vec{p}_1| \cdot |\vec{p}_2|}\right)} \tag{3.10}$$

from reconstructed information. Since a potential NHits_1 requirement affects less amount of events than NHits_2, we first assess where to place the latter keeping $\mathrm{NHits}_1 \geq 5$, which is a conservative value as explained above.

In figure 3.11 it becomes apparent that from $\mathrm{NHits}_2 \geq 5$ to $\mathrm{NHits}_2 \geq 6$, the distribution itself does not change in shape but rather shifts. This is qualitatively different when changing from $\mathrm{NHits}_2 \geq 4$ to $\mathrm{NHits}_2 \geq 5$, where a considerable amount of the shoulder to the left of the peak decreases. Hence $\mathrm{NHits}_2 \geq 5$ is the right cut to make in order to have a good quality 2nd prong. The left plot in fig. 3.11 shows that there is no change in shape for the different distributions and almost no shift. Therefore the most sensible cut in NHit_1 is to be at least equal to NHit_2. From this study we conclude that $\mathrm{NHits}_1 = \mathrm{NHits}_2 \geq 5$ is the most appropriate choice in order to guarantee a gaussian-shaped invariant mass peak.

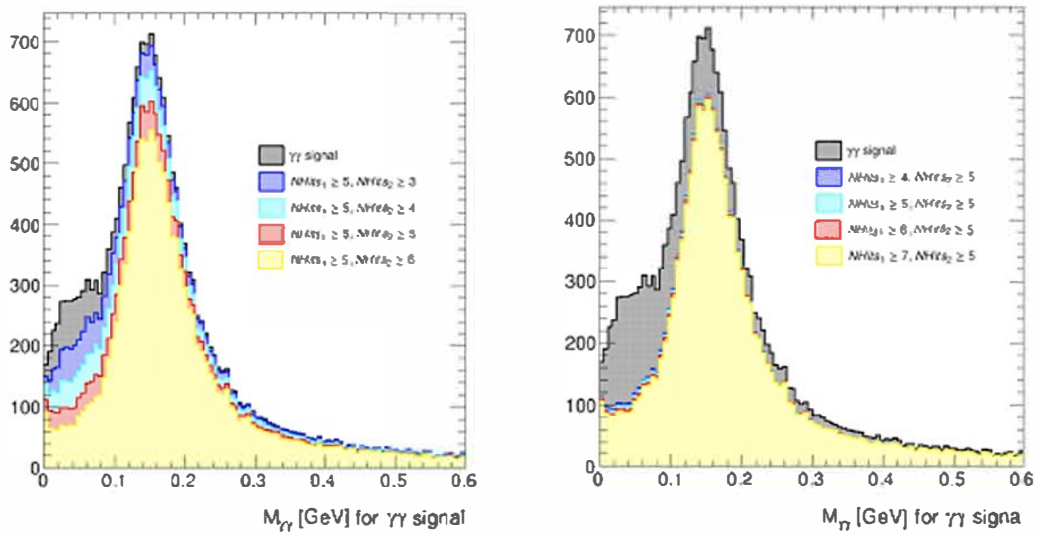

Figure 3.11: Both plots show the invariant mass, eq. (3.10), for signal $\gamma\gamma$ events. On the left we vary the NHits_2 cut and keep the NHits_1 cut constant, whereas on the right we fix $\text{NHits}_2 \geq 5$ and change the requirement for NHits_1.

Figure 3.12 shows 2D plots for the invariant mass variable as a function of NHits_1 and NHits_2 respectively. These show the improvement going from $\text{NHits}_2 \geq 4$ to $\text{NHits}_2 \geq 5$ as events with low values of the invariant mass disappear. The plots without NHits_2 cut almost show no difference when changing the NHits_1 cut.

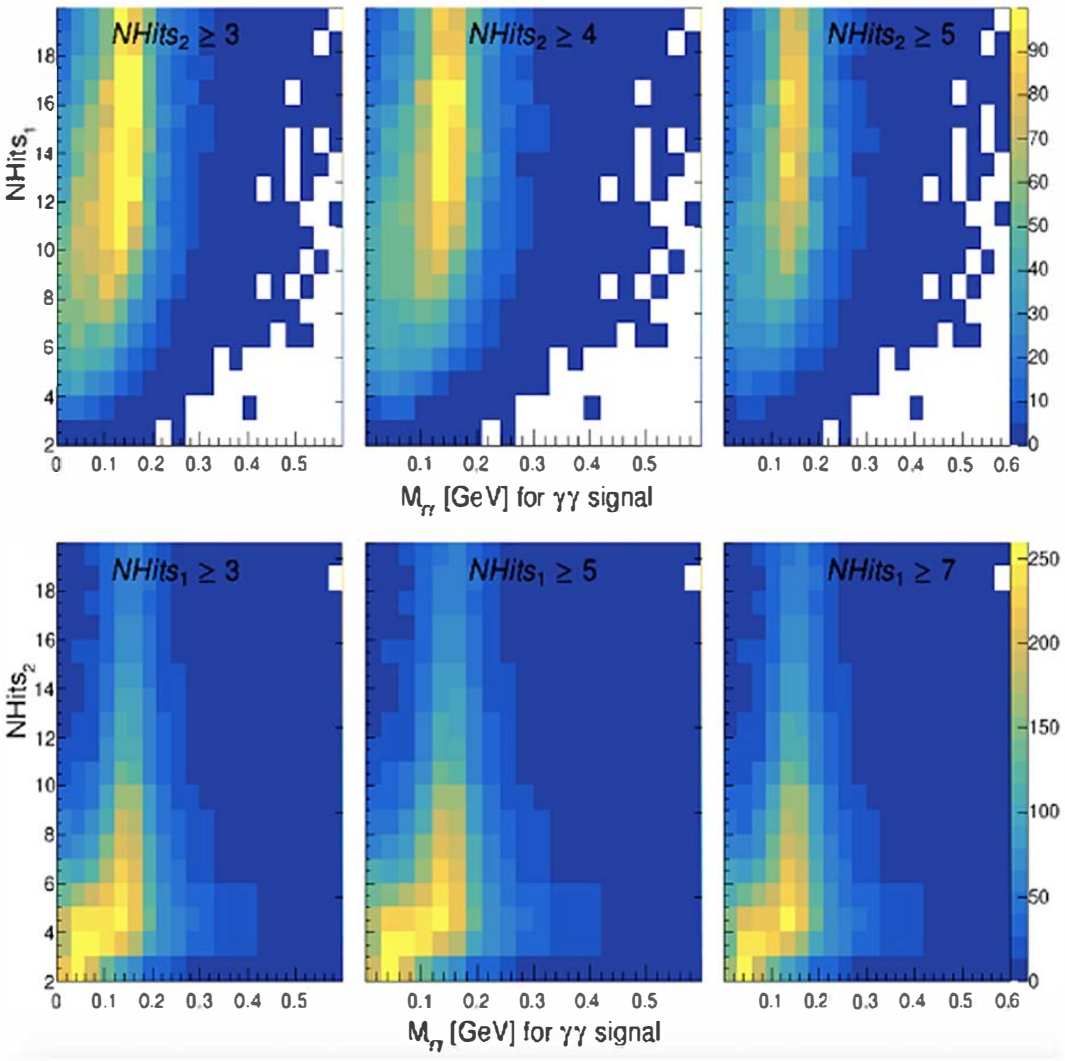

Figure 3.12: All 6 histograms are filled with signal $\gamma\gamma$ events. The top row depicts the invariant mass, eq. (3.10), and NHit_1 space for different cut values of NHit_2. The bottom row contains the same events but in invariant mass, NHit_2 space for different cut values of NHit_1. Note that the z-scale is the same for all plots in the same row, but changes from one row to the other.

3.6.6 π^0 Kinetic Energy Threshold

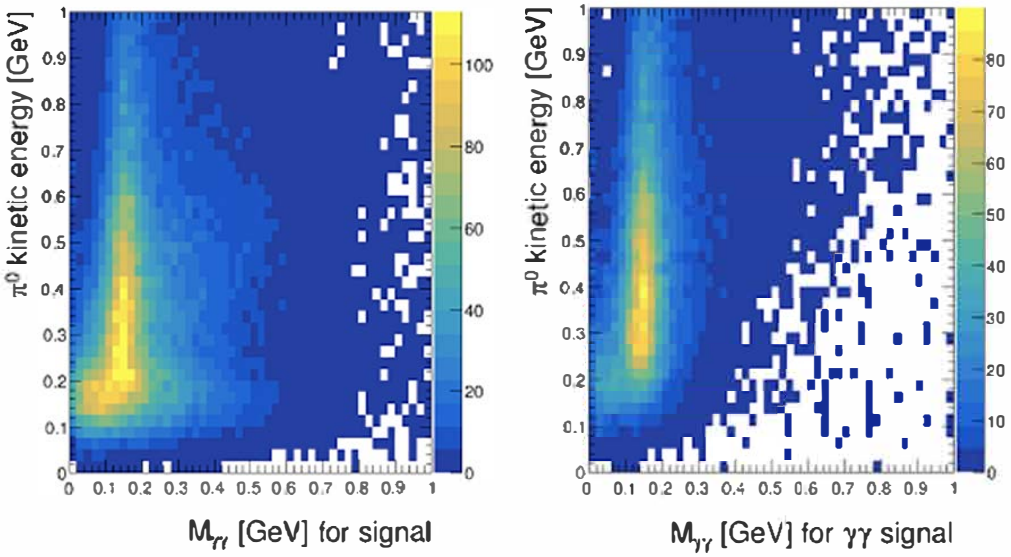

Figure 3.13: The invariant mass as a function of the true kinetic energy of π^0 for signal (left) and signal $\gamma\gamma$ events (right), both with $\text{NHits}_{1,2} \geq 5$.

Very low energy neutral pions can be neither detected nor identified, therefore a kinetic energy threshold is needed. In order to determine this threshold for this selection, the 2D plot on the left of fig 3.13 is produced, which shows the reconstructed invariant mass and the true kinetic energy of the π^0 binned in 25 MeV intervals.

For events with several neutral pions in the final state, the true kinetic energy of the π^0 is not a well defined variable. When there are several neutral pions in a given event, the most energetic one will be the one considered. The assumption behind this choice is that the most energetic π^0 in the event is likely to deposit more energy in the detector being the only one reconstructed

most of the time.

For every row in the grid, i.e. within the same bin of kinetic energy, the maximum of events at the correct invariant mass bin should be identifiable. Even by eye it is clear that this threshold should be at least at around 200 MeV, given that below this value the events are broadly distributed and the peak is not at the right invariant mass value.

From the left plot in fig. 3.14 the kinetic energy threshold for the neutral pion is determined to be 275 MeV, because the efficiency flattens out and reaches 50%.

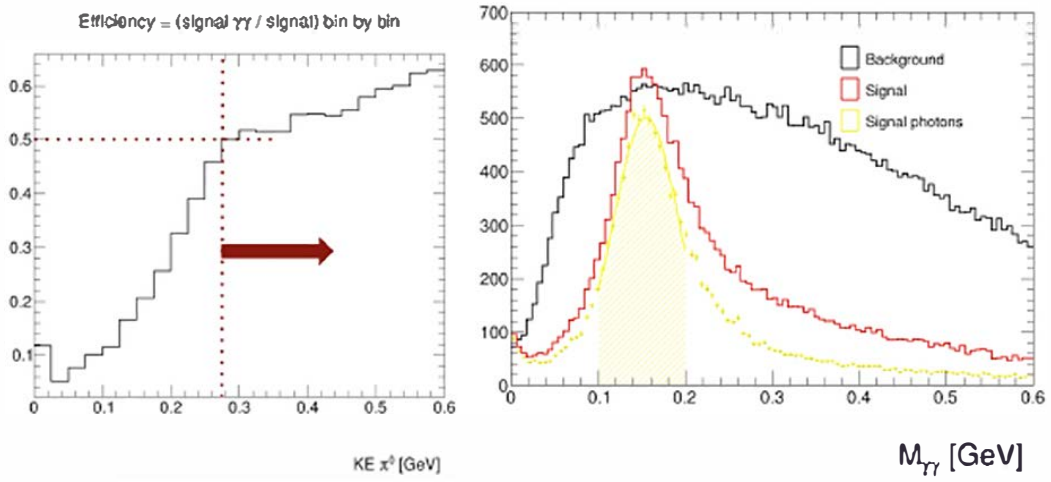

Figure 3.14: Left: Efficiency of signal $\gamma\gamma$ over total amount of signal events with $\text{NHits}_{1,2} \geq 5$ computed within 25 MeV bins in true kinetic energy of the neutral pion, where the dotted red lines indicate the choice of threshold.
Right: The invariant mass for background, signal and signal $\gamma\gamma$ events with $\text{NHits}_{1,2} \geq 5$ and $\text{KE}_{\pi^0} \geq 275$ MeV (only for signal $(\gamma\gamma)$). The latter distribution is fitted with a gaussian within the shaded range of the histogram, $[0.1, 0.2]$ GeV and the mean is at 0.155 GeV.

The selection cuts described in this section are applied before assaulting the real challenge: how to differentiate between signal and background. In simulation, also called MC for Monte Carlo, this is not a problem, because the truth information contains the key to distinguish between both. Whereas in data this is not the case and a pre-manufactured key is very much needed. The general idea is to study the theory in hand, in this particular case: simulation, and extract the features that enable a distinction between them.

The traditional way of separating signal from background is making use of the different topologies and energy deposition characteristics of different particles, but new machine learning techniques have proven to be more powerful in doing so without inserting the physics knowledge acquired a priori. Hence, a Boosted Decision Tree was trained on simulated data to extract these features[4].

The next section will enlighten some of the technical machinery and provide details on the procedure for future generations interested in replicating the plots.

[4]The simulated data definition for this part of the analysis is: *prod_caf_R201125-prod5.1reco.a_nd_genie_N1810j0211a_nonswap_fhc_nova_v08_full_v1_batch3*.

3.7 Boosted Decision Tree as classifier

A Boosted Decision Tree (BDT) was developed to distinguish between signal and background within the NC π^0 selection. The framework used to train and evaluate the performance of the BDT is the Toolkit for Multivariate Data Analysis with ROOT (TMVA) [90].

A BDT is a multi-variate classification algorithm that takes signal and background events with a corresponding list of discriminating variables as input and outputs a new classifier after the training that assigns a score from $[-1, 1]$ to each event.

The basic structure of the algorithm is a tree. A decision tree starts from a root node with equal amount of signal and background (maximal mix) and applies criteria or constraints to split the sample into purer nodes.

If a node satisfies any of the stopping criteria or can not further optimize a splitting of the sample into purer nodes, it terminates the branch with a leaf. The terminating conditions are: minimal amount of events in each node, to ensure statistical significance, and a maximal depth set to 5. The Gini Index is the separation criterion used for node splitting. This BDT uses 100 trees to find the score for each event and uses AdaBoost as boosting method.

Before the training, overall weights on signal and background events are set such that the algorithm is trained on an equal amount of both categories in order to avoid bias of the classifier towards the more populated category.

The variables the finalized BDT was trained on are:

- **Shower width of first and second prong:** averaged and weighted (by its energy deposits) width of the prong.

- **Shower gap of first and second prong:** distance between the location of the reconstructed vertex and the start of the reconstructed prong. A priori, this variable is very powerful to help distinguish neutral pions from charged particles like protons, electrons and other pions. Neutral pions, in contrast to the other particles, present a gap between the interaction vertex and the beginning of the energy depositions, which corresponds to the distance traveled by the π^0 itself before decaying into two gammas, and to the conversion length of the latter, discussed in section 2.2. Nevertheless, a well known and common reconstruction failure obscures this variable as the reconstruction algorithm often assign hits from the vertex (originating from other particles) to the start of the prong, such that the distribution of gap length has a maximum at zero even for photon prongs.

- **Maximal plane number gap of first and second prong:** this variable is also easily available using the CAFAna framework and turned out to be very useful, given the short coming of the **Shower gap** explained above. When this known failure mode happens, it may be that the **Maximal plane number gap** is the actual gap in amount of planes instead of units of cm.

- **EMID of first and second prong:** this variable was discussed in great detail in subsection 3.6.4.

- **ProtonID of first and second prong:** this variable is very similar in spirit as the EMID, but it is one of the 5 variables from Derek Doyle's 5lCVN training [88, 89]. This variable was trained to solely identify protons and distinguish them from the other four particle types present in the training sample. Due to the improvement it provides to the classification of signal and background, it was included as part of the inputs.

- **Invariant mass:** this is probably the most important variable, besides the EMID, which does most of the heavy lifting distinguishing photons/electrons from other particles. There were several studies and ideas on how and where to use this discriminating power, but the definitive choice was to impose a selective interval [0.1, 0.25] GeV and use it for the training, see fig. 3.15.

- **Amount of energy deposited within a 40 cm cube around the reconstructed vertex:** this variable was implemented within the CAFAna framework by Chatura Kuruppu [91], which opened the opportunity for an easy test within this analysis. Given a π^0 production in the neutrino interaction, the amount of energy deposited around a close vicinity of the reconstructed vertex is relatively small. Intuitively it makes sense and the quantitative results improved.

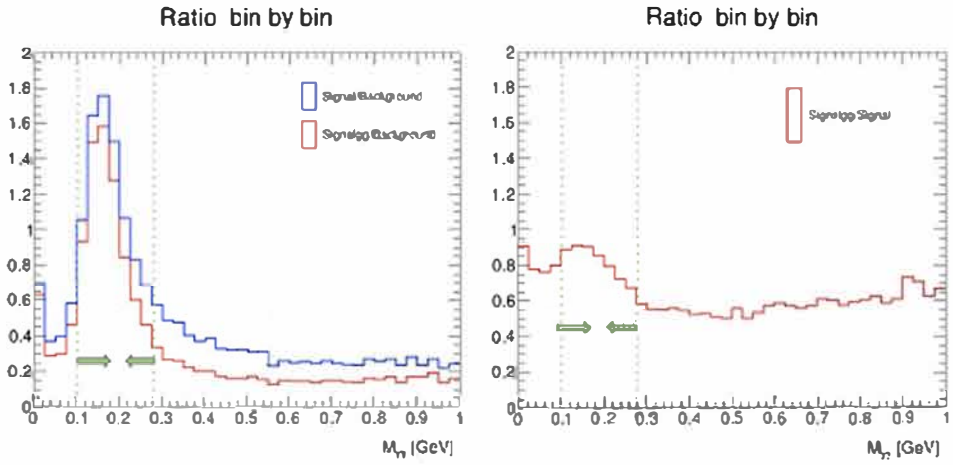

Figure 3.15: Optimization criterium for the invariant mass cut.

The input variables were all added one by one, correlation between them were studied and several figures of merit (variable importance, separation power, ROC, purity and efficiency) were analyzed before settling for this set of parameters and additional cut in invariant mass. The variables that did not make it into the training are either strongly correlated with others, so that they wouldn't provide additional information, or are correlated with the energy and angle of the prongs. Overtraining is definitely undesired and has been avoided by making sure that the test sample and the training sample outputs were consistent with each other.

Figure 3.16 shows the result of the BDT training and the distributions for signal and background events, which in turn are classified into neutral-current and charge-current background.

Once the BDT is optimized to separate signal and background events

using the least amount of easily accessible variables within the CAFAna framework, two possible courses of action unfold: to either set a cut value for the BDT output variable to delimit signal (above) from background (below) events, or to proceed with a template fit. The cut approach is more straight forward, therefore cumulative efficiencies and purities as well as the product of those were plotted to asses the power of different BDT scenarios. From these studies it became clear that a template fit path would be more suitable for this analysis given the low amount of signal events and the limited power of the BDT as classifier.

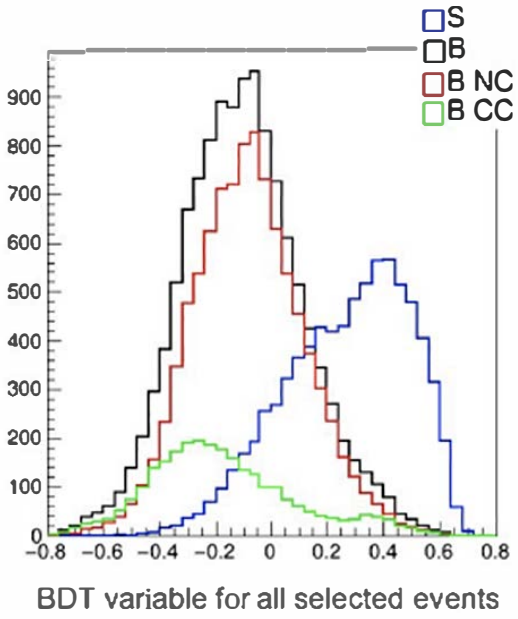

Figure 3.16: BDT output for all events passing the selection.

3.8 Template Fit

The general idea of a template fit measurement is to generate distributions from MC and vary their normalization, α for the B NC template and β for the B CC template displayed in fig. 3.16, while keeping their shape and fitting to the total amount of data events. The goodness of fit can be assessed by a chi-square calculation and from the resulting normalization of the distributions it is possible to extract the amount of signal (N_{π^0}) and background ($\alpha + \beta$) present in the data sample,

$$N_{\pi^0} = \text{Number of events in data} - \alpha(\text{B NC}) - \beta(\text{B CC}). \tag{3.11}$$

The framework in order to do so was semi-developed and some tests were done, but time became short to fully follow through.

The first step towards a complete template fit measurement is to determine the binning for which each of those templates is going to be made. For this NC π^0 analysis aiming for a double differential measurement in momentum and angle of the π^0, the phase space of the neutral pion has to be subdivided in a sensible way. More about the choice of binning will be explained in the next sections.

3.9 Neutral Pion Momentum Reconstruction

The in-depth understanding of the π^0 momentum reconstruction capabilities of the NOνA experiment is paramount to this measurement. Therefore a thorough description of it is consecrated to this section.

Some qualitative understanding of the reconstruction performance had already been developed by this point while training the various BDTs with several variables. One option that was considered at the time, was to only use the information of the first EM-like prong, given that the gammas often overlap and the second prong is less reliable to be reconstructed in the right direction or more prompt of being contaminated by other particles.

The gist of those studies turned out to be that the combined information correspoding to the two separate prongs was closer to the true MC than the forlorn one prong by itself. Therefore, for all the plots to come, and the BDT explained before, the decision was made to use both information from the reconstructed showers required for all of the events.

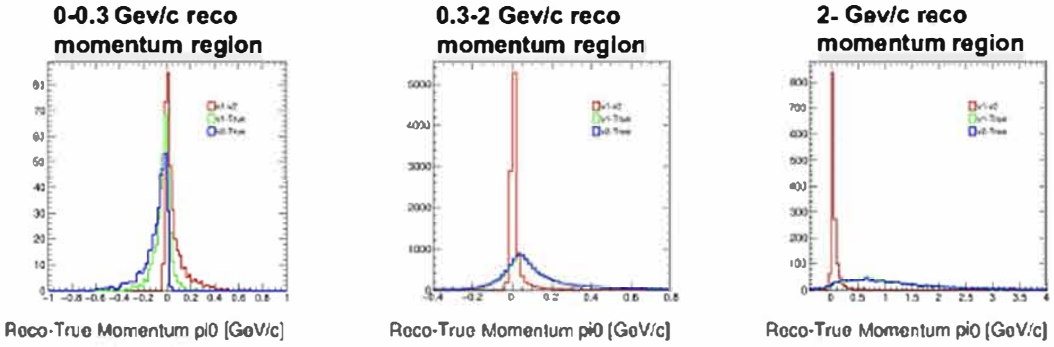

Figure 3.17: On the left: the low momentum region, in the middle: the intermediate momentum region, on the right: the high momentum region with low statistics.

There are two distinct ways in which the momentum of the neutral pion can be reconstructed. One of them, which will be referred to as first version,

v1, only uses the amount of energy associated with both prongs:

$$\text{(v1)} \quad |\vec{p}_{\pi^0}| = \sqrt{(E_1 + E_2) - m^2}, \tag{3.12}$$

where m is the literature value for the neutral pion.

The second version, v2, is the actual sum of the reconstructed objects:

$$\text{(v2)} \quad |\vec{p}_{\pi^0}| = |\vec{p}_1 + \vec{p}_2|, \tag{3.13}$$

and therefore additionally contains the prong's direction and opening angle. As mentioned before, a prong in NOνA has a starting point and a direction associated with it. The sum of the unitary vectors corresponding to each of the showers multiplied with the energy associated to them is $\vec{p}_i$.

Figure. 3.17 highlights the differences between the two versions in three regions of the neutral pion momentum. Each of the plots in the triptych shows v1 (in green) and v2 (in blue) compared to the true momentum of the most energetic π^0 present in the interaction as well as v1 minus v2 (in red).

The two versions only significantly differ in the low momentum region, where v1 clearly outperforms v2 with less bias and a more gaussian looking distribution. Even though in the other regions it is less obvious, version 2 of the reconstructed momentum is less biased.

Given these results, the decision was made to use v2, since the measurement is meant to be performed as a function of the angle of the π^0 with respect to the beam direction. Nevertheless, the low and high momentum regions will not be part of the measurement because of poor angular resolution for stubs and low amount of statistics respectively.

The performance of the reconstruction algorithms applied to the two prongs of the selected signal events is depicted in fig. 3.18, which shows true vs reco momentum of the π^0. The black line is meant to be a reference line to better appreciate deviations from $y = x$. In addition, fig. 3.19 shows the differences between reco and true momentum of the π^0 as a function of its truth. The red crosses in the three plots denote the average (in y) for each bin (in x).

The main features of plots 3.18 and 3.19 is the worsening of resolution, increased bias and larger deviation from a gaussian-like distribution towards higher momenta of the neutral pion, see fig. 3.20.

These plots were compared to the ones corresponding to the ν_μ CC π^0 analysis in NOνA, which uses a similar preselection, dataset but different signal definition. In their case, the events pile towards the reference line and the reconstruction is cleaner, but an additional cut (EMID for both prongs > 0.17) is needed to achieve this improvement. This requirement imposes a minimum amount of electomagnetic-shower-like behavior for the prongs associated with the meson, which was studied and adopted for this analysis. The corresponding changes can be appreciated in fig. 3.21 and 3.22.

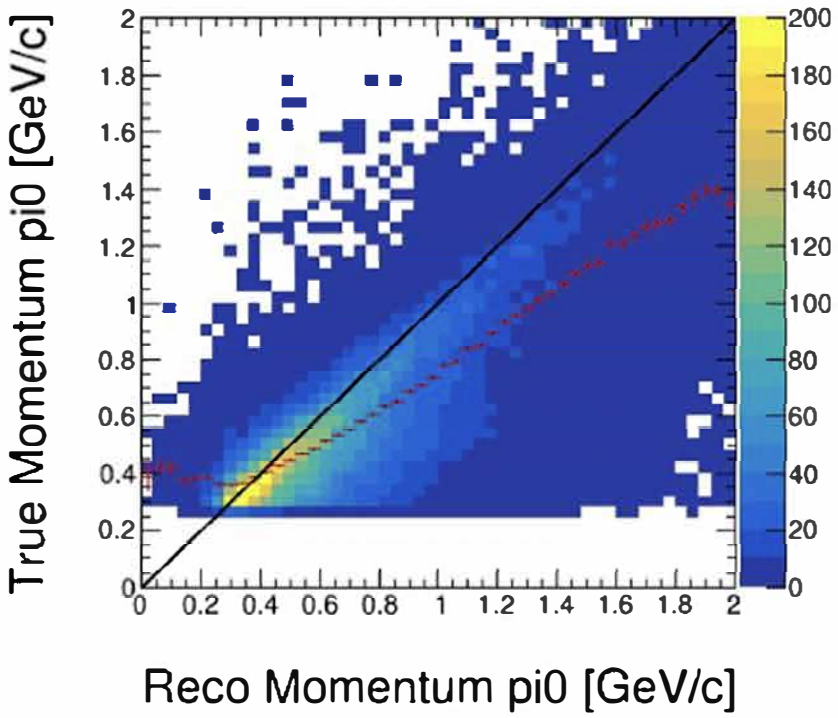

Figure 3.18: Momentum reconstruction out of the box without EMID cut.

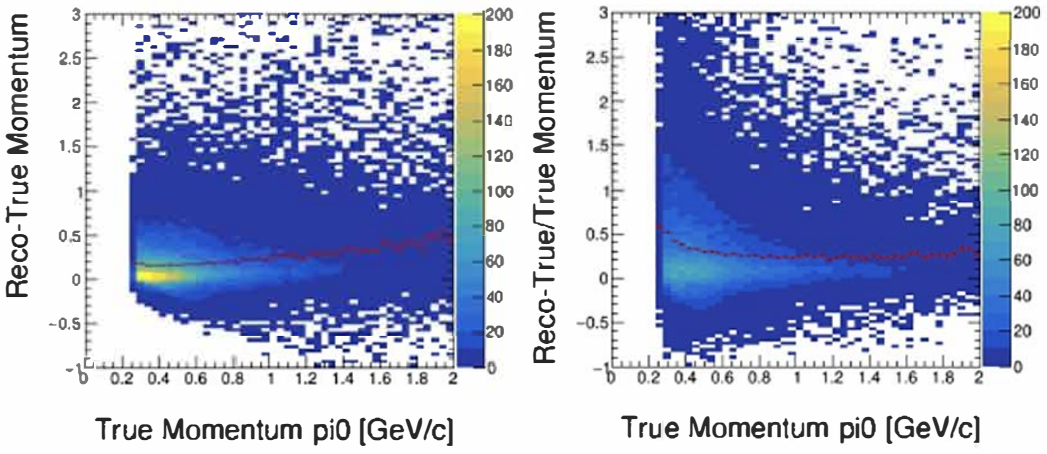

Figure 3.19: Momentum reconstruction out of the box without EMID cut.

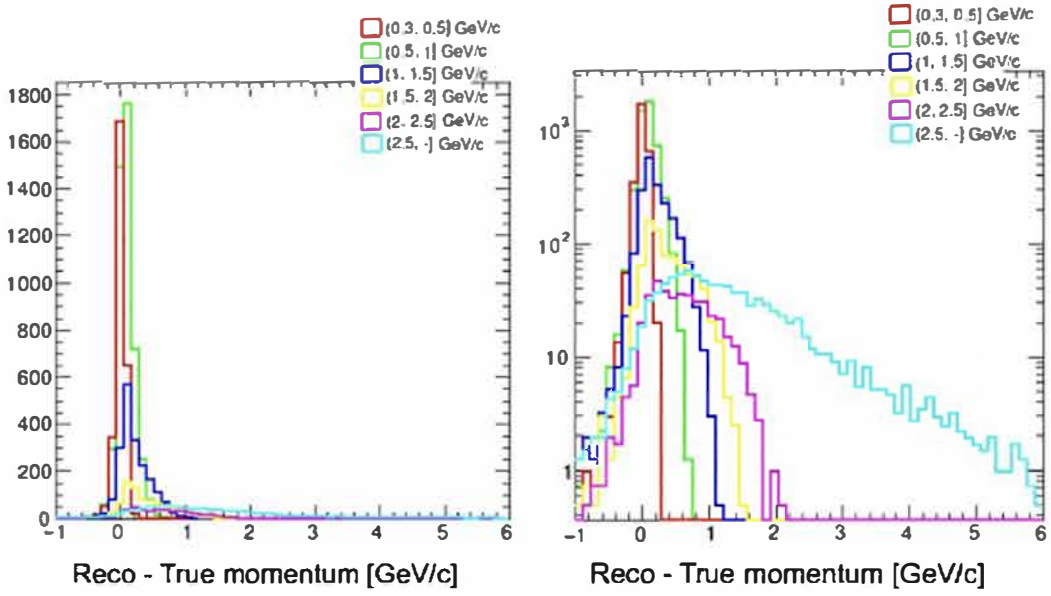

Figure 3.20: Momentum resolution slices out of the box without EMID cut.

Flipping between fig. 3.21 and 3.18 it is possible to spot the depletion of events, specially in the lower right shoulder, as well as the closing of the gap between an imaginary line connecting the red crosses, here referred to as Maginot Line for simplicity, and the reference line in black. The events affected by this EMID cut were further investigated and their prongs often get truth-matched to other none-gamma particles. Therefore, this loss of events was deemed as necessary to improve the measurement.

A second order effect that is less noticeable at first glance is the disappearance of the wiggles in the Maginot Line. Given the somewhat consistent trend of reco being larger than true, the initial idea and effort was focused on fitting a polynomial function to the averages of each bin and use it to correct

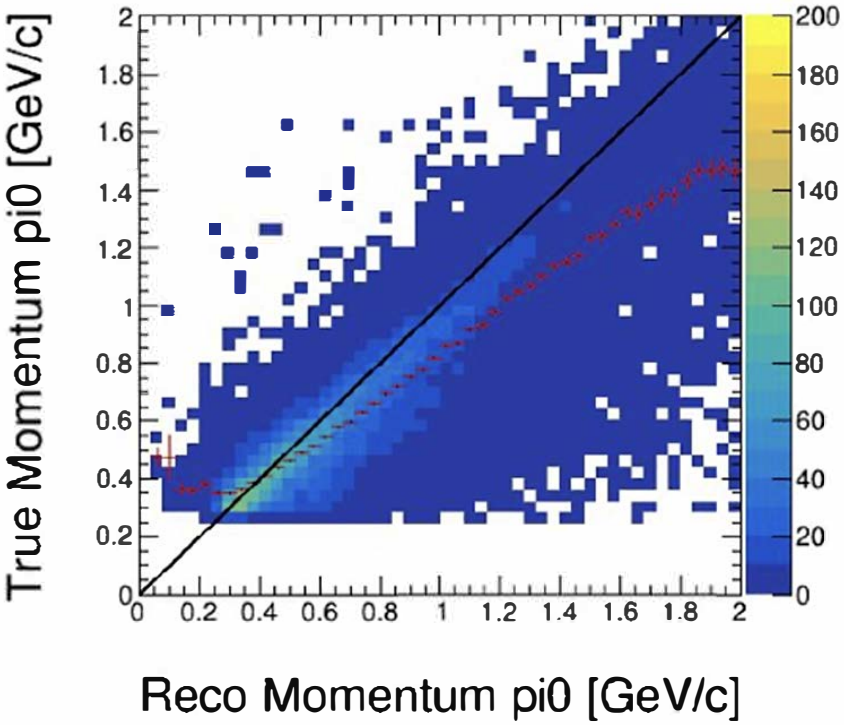

Figure 3.21: Momentum reconstruction with EMID > 0.17.

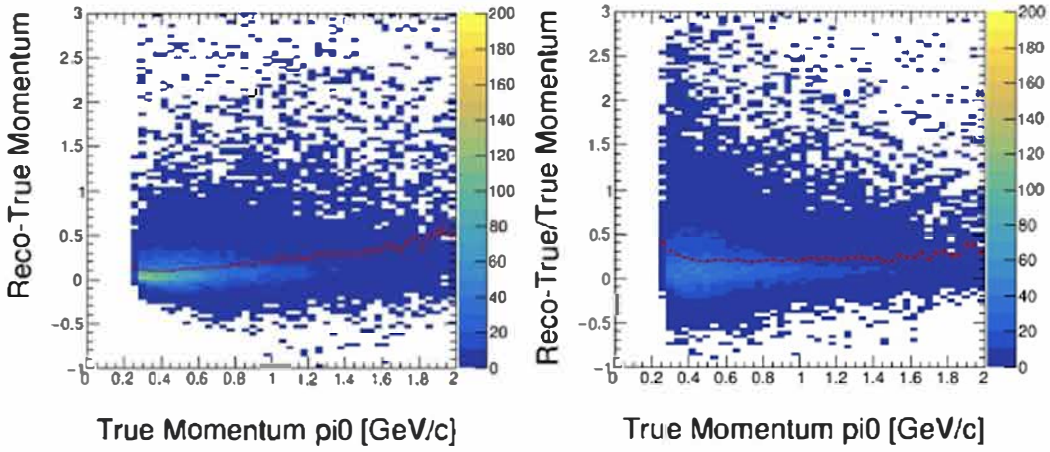

Figure 3.22: Momentum reconstruction with EMID > 0.17.

the overshooting in reco momentum.

Several fitting functions were investigated (e.g. fig. 3.25), but a machine learning (ML) algorithm seemed to be more contemporary and was worth contemplating. In the section to come, the full-fledged path towards an amended momentum reconstruction is presented.

The last feature to point out is the change in curvature of the Maginot Line at the crossing with the black reference line. Fitting of this lower part would require a higher order polynomial and studies had shown that low reco momentum events have poor angular reconstruction.

3.10 Momentum Correction using gradient Boosted Decision Tree on regression

As already motivated in the previous section, the need of the neutral pion momentum correction is imperative and the method of choice is a gradient Boosted Decision Tree. Several other machine learning algorithms (MLP, DNN, kNN and a simple BDT) were trained to predict the momentum reconstruction from a set of input variables, but the optimized technique follows this recipe:

- gradient Boosted Decision Tree with 100 trees,
- input variables: invariant mass, $\mathrm{EMID}_{1,2}$ and the reconstructed momentum of the neutral pion,

to obtain right from left in fig. 3.23.

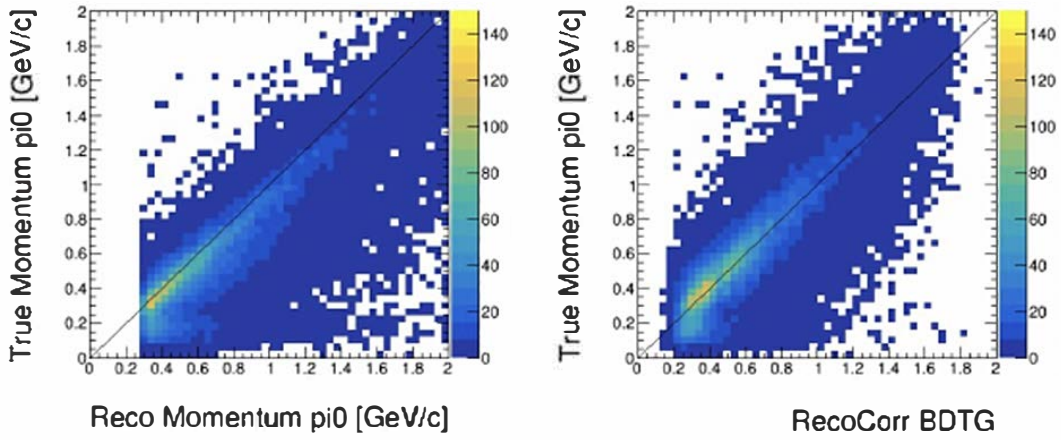

Figure 3.23: On the left, a TH2D histogram filled with signal events in true and reco momentum space of the neutral pion. On the right, the correction after the BDTG has been trained and optimized. A clear improvement and migration of events towards the reference line can be appreciated.

The four input variables as well as the target variable, in this case the true momentum of the most energetic neutral pion in the interaction, are used to predict the corrected reconstructed momentum, which will replace the originally reconstructed momentum from here on.

This method is distinct from the previously explained Boosted Decision Tree as classifier in that it predicts a variable, which is not part of the input. Instead of differentiating between signal and background events, it outputs a variable not bounded and matching the so called target variable (true $\vec{p}_{\pi^0}$).

Here the cut on true was removed and replaced by a similar cut on reco $\vec{p}_{\pi^0}$, but the ML massaging of the data leads to the migration of some events to that space. As explained before, due to low angular resolution on short prongs, low momenta events are discarded, therefore this will not be a

problem.

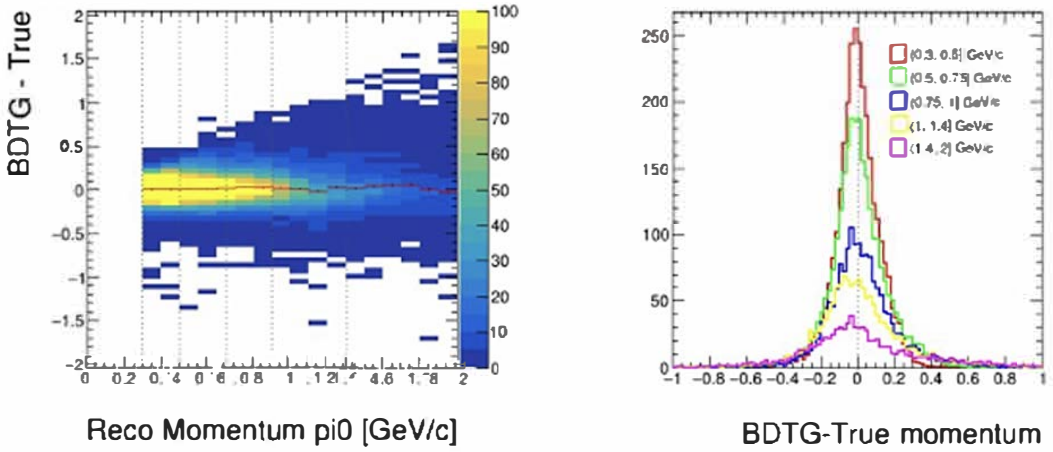

Figure 3.24: On the left, a TH2D histogram with the difference between reco corrected momentum (denoted as BDTG) and true as a function of reco is filled with the same signal events. Here the red crosses form a fairly straight line ($y = 0$), which speaks for the power of the amendment. On the right, the resolution of the momentum reconstruction is plotted for the binning suggested on the left.

Figure 3.24 shows the new distribution

$$\text{corrected reco } \vec{p}_{\pi^0} \text{ (BDTG) } - \text{ true } \vec{p}_{\pi^0}, \tag{3.14}$$

of events along reco $\vec{p}_{\pi^0}$. The black, fine dotted, vertical lines hint towards a potential binning in reco space. For each of those bins, a one dimensional distribution of the resolution is plotted: all of the peaks align and the widening increases as a function of higher energy of the neutral pion.

For comparison to the preferred BDTG correction of $\vec{p}_{\pi^0}$, figure 3.25 displays the already mentioned first attempt of a polynomial fit (in yellow). In analogy to fig 3.24, fig. 3.26 shows the resolution for the same binning scheme. It is obvious, that the fit correction underperforms with less symmetrical, less gaussian-like distributions and higher bias towards higher energies.

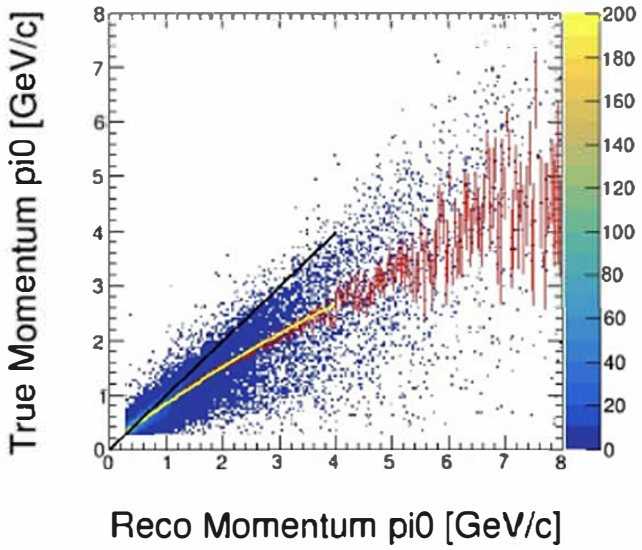

Figure 3.25: Momentum reconstruction with EMID > 0.17 and 2nd order polynomial fit to the averages in red. The fitting range is limited to the length of the yellow line ignoring everything above and below. In black the reference line (y=x).

All bins considered, figure 3.27 is the last plot arguing for a BDTG correction instead of a fit, where T stands for truth.

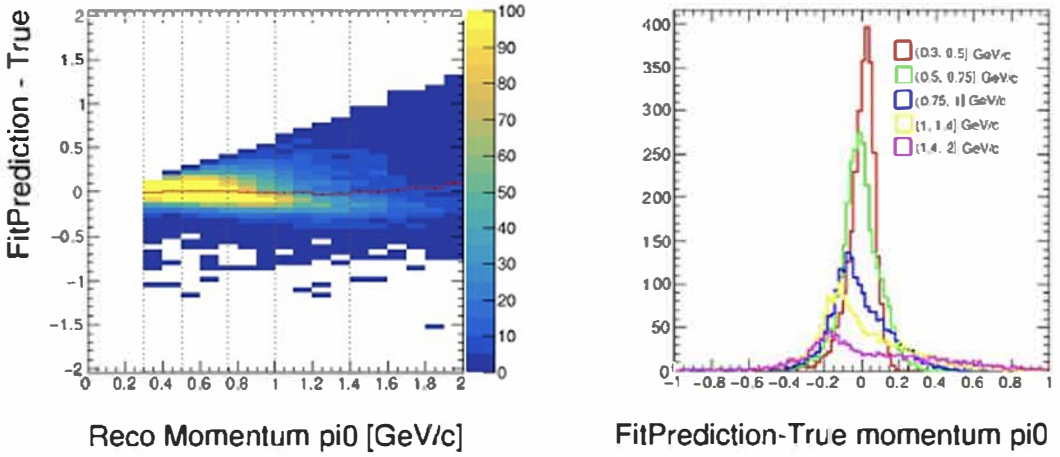

Figure 3.26: Resolution of the corrected momentum reconstruction via 2nd order polynomial fit plotted for the same binning of fig. 3.24.

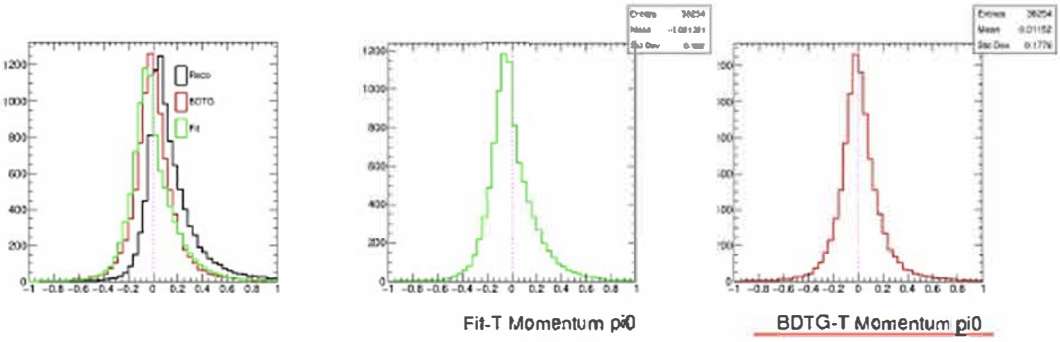

Figure 3.27: Resolution of corrected momentum reconstruction using a 2nd order polynomial as fit or the BDTG. All events are plotted summing over all the bins of the parameter space $[0.3, 2]$ GeV/c. The plotted differences are: Reco minus true in black, BDTG corrected minus true in red, Fit minus true in green.

3.11 Proposed binning

Guided by previous and current analyses performed with NOνA ND data, it was clear that systematic errors were going to be the limiting factor for this measurement. Therefore, a set of bins was chosen in order to maximize the amount of events kept and minimize bins with very little statistics.

Figure 3.28 is a grid of the parameter space ($\vec{p}_{\pi^0}$, θ), where the number in each bin corresponds to the amount of events within. The legend to the right of the table indicates the color-code: green for proposed analysis bins, gray for bins that contain less than 100 signal events and red for below selection cut. Outside the colored space, the x-axis is the corrected reconstructed momentum of the neutral pion [GeV/c] and the y-axis is the angle with respect to the beam direction in degrees.

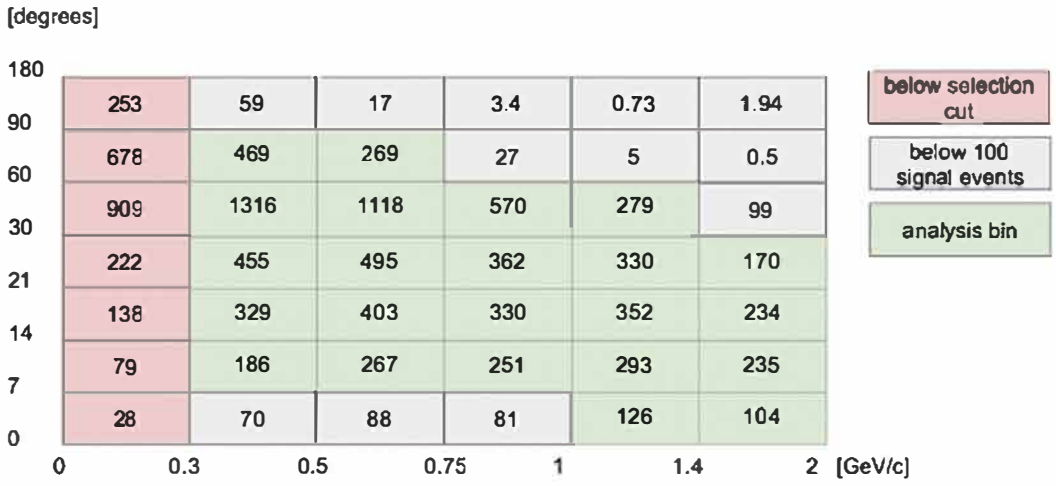

Figure 3.28: Number of signal events in each bin.

For the same set of bins, figure 3.29 is filled with the standard deviation

of the angular resolution distribution for the corresponding slot. The cuts are in reco space and the resolution is reco - true. The purpose of this exercise is to make sure that the angular and momentum resolution is smaller than the actual bin size.

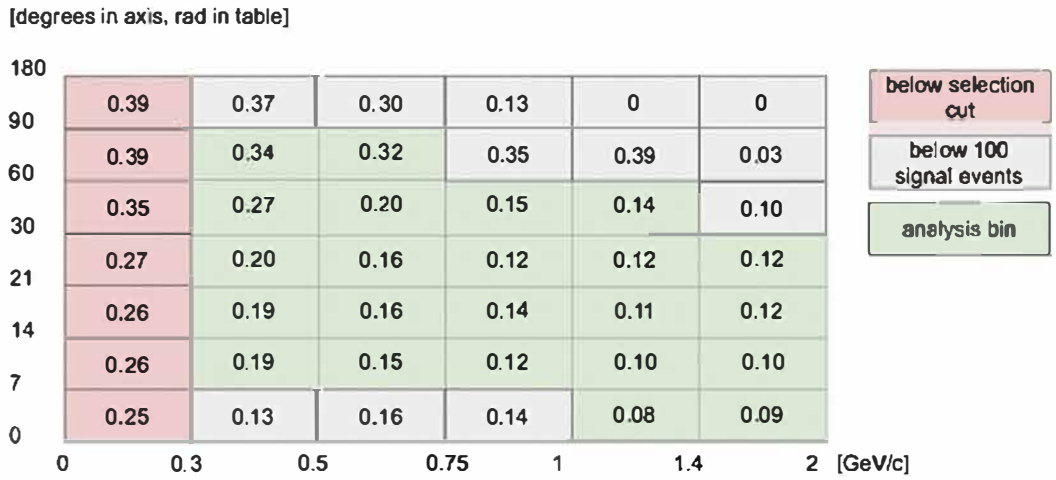

Figure 3.29: Standard deviation in rad.

The only additional piece of information provided in fig. 3.30 with respect to fig. 3.29 is the first column (colored green), which does not show the first momentum bin, but the bin width of the angle in radians. This might seem like a confusing way of displaying the information, but intuitively degrees are easier to picture, and the whole analysis was performed in radians.

Indeed some of the distributions (reco - true) have a standard deviation that exceeds the bin width, see figs. 3.31, 3.32, and 3.33. These were further evaluated and several options were contemplated. One option was to perform a gaussian fit to the peak of the distribution ignoring the tales, which are

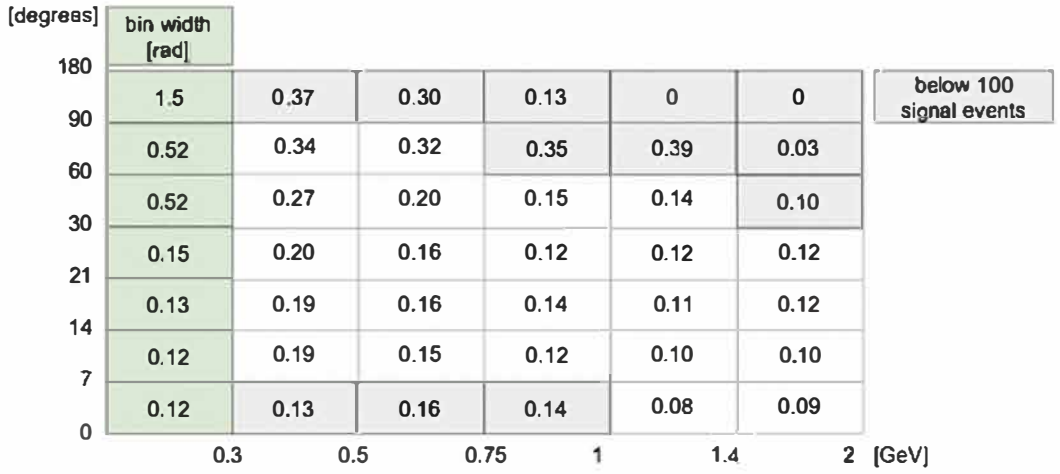

Figure 3.30: Check that bin width is not smaller than standard deviation.

responsible for the large RMS. The other option was to make the bins larger, but the RMS also increased since more events end up in the tales. Therefore, it was deemed appropriated to keep it as is.

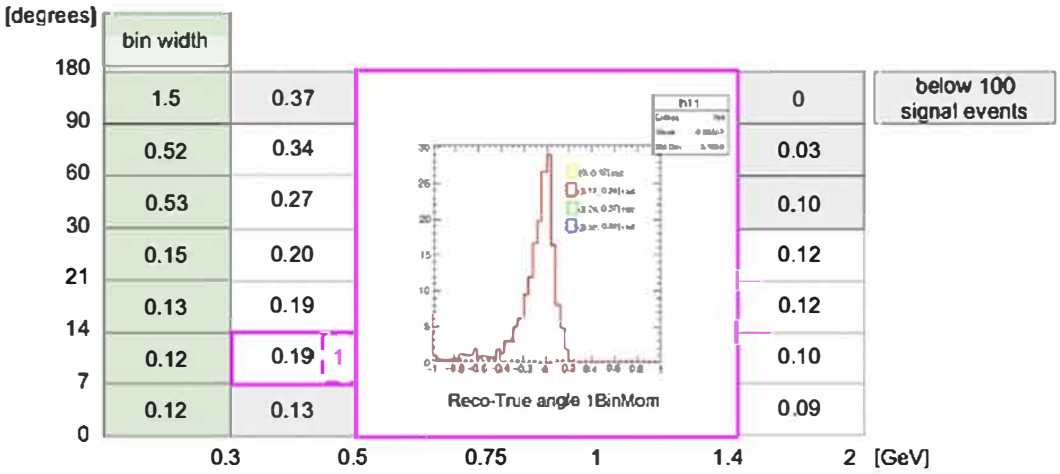

Figure 3.31: Angle resolution in bin 1.

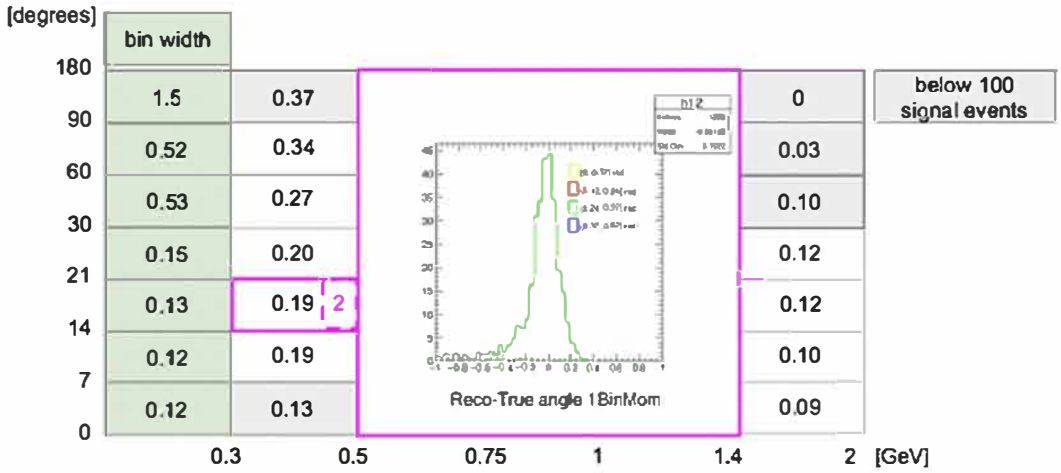

Figure 3.32: Angle resolution in bin 2.

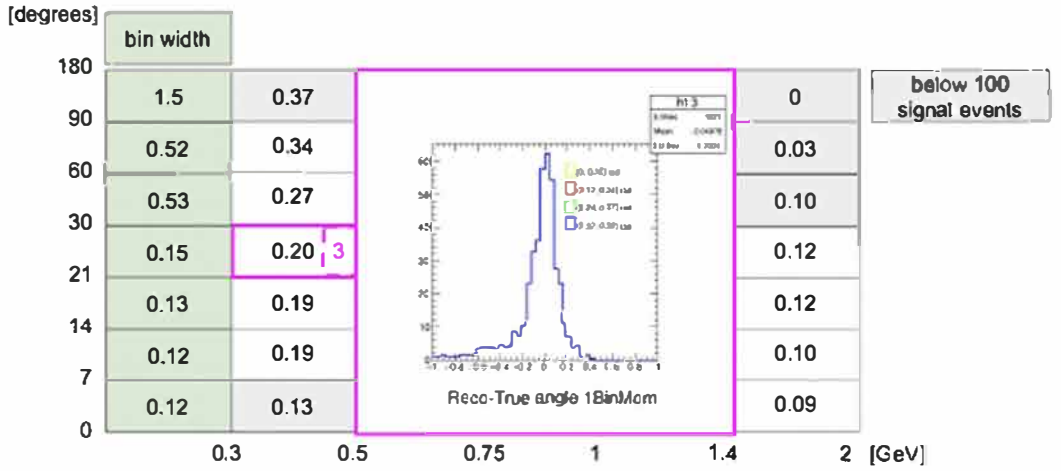

Figure 3.33: Angle resolution in bin 3.

3.12 Simplified measurement

As stated at the beginning of the chapter, the intention was to measure the cross-section in each true bin i of the parameter space as described by:

$$\left(\frac{d^2\sigma}{d\cos\theta_{\pi^0}\, dp_{\pi^0}}\right)_i = \frac{\sum_j U_{ij}^{-1} N_{\pi^0}(\cos\theta_{\pi^0}, p_{\pi^0})_j}{N_t\ \phi\ \epsilon(\cos\theta_{\pi^0}, p_{\pi^0})_i\ \Delta\cos\theta_i\ \Delta p_{\pi^0 i}}. \tag{3.15}$$

As events unfolded, time became short and a simplified version detailed below crystalized. The rearrangement of the terms leads to

$$\begin{aligned}&\sum_j U_{ij}^{-1} N_{\pi^0}(\cos\theta_{\pi^0}, p_{\pi^0})_j \\ &= \left(\frac{d^2\sigma}{d\cos\theta_{\pi^0}\, dp_{\pi^0}}\right)_i N_t\ \phi\ \epsilon(\cos\theta_{\pi^0}, p_{\pi^0})_i\ \Delta\cos\theta_i\ \Delta p_{\pi^0 i},\end{aligned}$$

and assuming the unfolding matrix to be $U_{ij}^{-1} \approx \mathbb{1}$, the following holds

$$[N_{\pi^0}(\cos\theta_{\pi^0}, p_{\pi^0})]_i = \left(\frac{d^2\sigma}{d\cos\theta_{\pi^0}\, dp_{\pi^0}}\right)_i N_t\ \phi\ \epsilon(\cos\theta_{\pi^0}, p_{\pi^0})_i\ \Delta\cos\theta_i\ \Delta p_{\pi^0 i},$$

where $N_{\pi^0}(\cos\theta_{\pi^0}, p_{\pi^0})$ is precisely fig. 3.28.

Chapter 4

Conclusion

This thesis describes two distinct projects within the NOνA experiment. The NOνA test beam project was meant to be my dissertation project, but the halo problem was a major impediment to achieve an analysis within a reasonable amount of time. Nevertheless, the NOνA test beam program has rapidly improved over the pandemic and is now up to speed and taking data. Future generations will profit from it and incorporate their results for a better calibration. Those studies will also influence future refinements of cross-section analyses in general and the here presented NC π^0 measurement in particular.

Attentive readers have probably spotted several flaws and shortcomings along the way, but here is the full list of wishes with respect to a more accurate and robust analysis. First and foremost, the measurement should be done using near detector data instead of MC. Secondly, systematic errors must be taken care of, specially considering the calibration uncertainties present in NOνA. Efficiency and purity corrections are also negligible given the simplification of the measurement, which was necessary due to the lack of unfolding techniques available in the time quench. Thirdly, the number of target nucle-

ons or nuclei has to be estimated, which can be done either making use of a numerical approach or an analytical calculation.

Last but not least, the continuing data taking of the NOνA experiment, the ripening of new machine learning techniques, and the enthusiasm of researchers is going to pave the way for much better measurements of neutrino cross-sections. Consequently, the precision of the neutrino oscillation parameters will improve and lead to final answers, discoveries of the fundamental nature of these tiny and still poorly understood particles.

Appendices

Appendix A

Monte Carlo Signal Event Displays

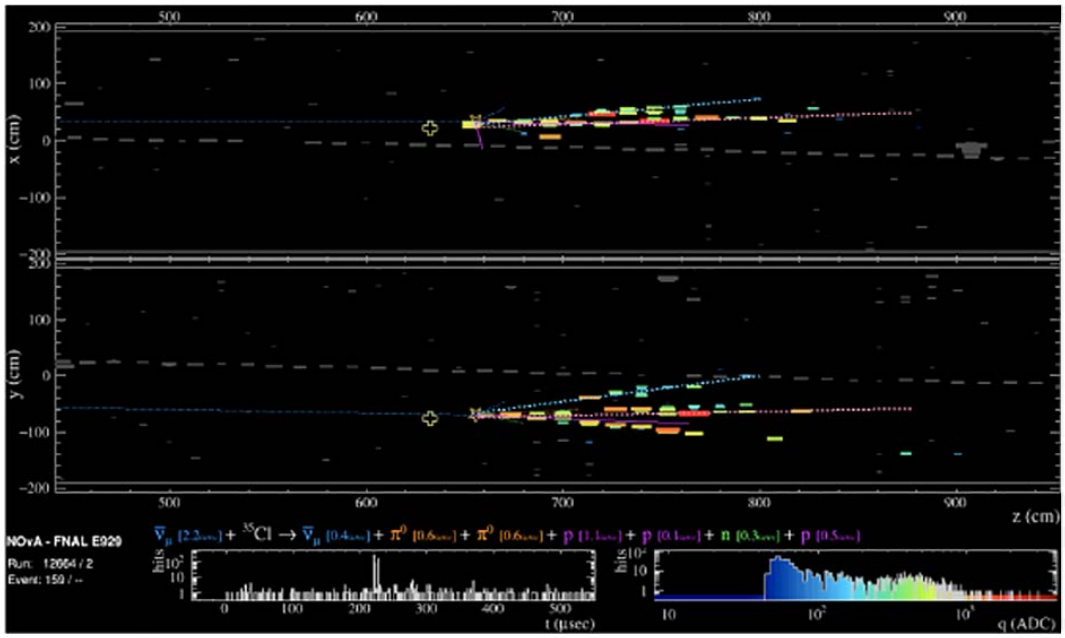

Figure A.1: Anti-muon neutrino neutral current interaction with two neutral pions of the same energy in the final state. Energy deposits from a proton in the final state get reconstructed as part of one of the gamma prongs. The cross mark represents the location of the reconstructed vertex, while the true vertex is at the position of the star.

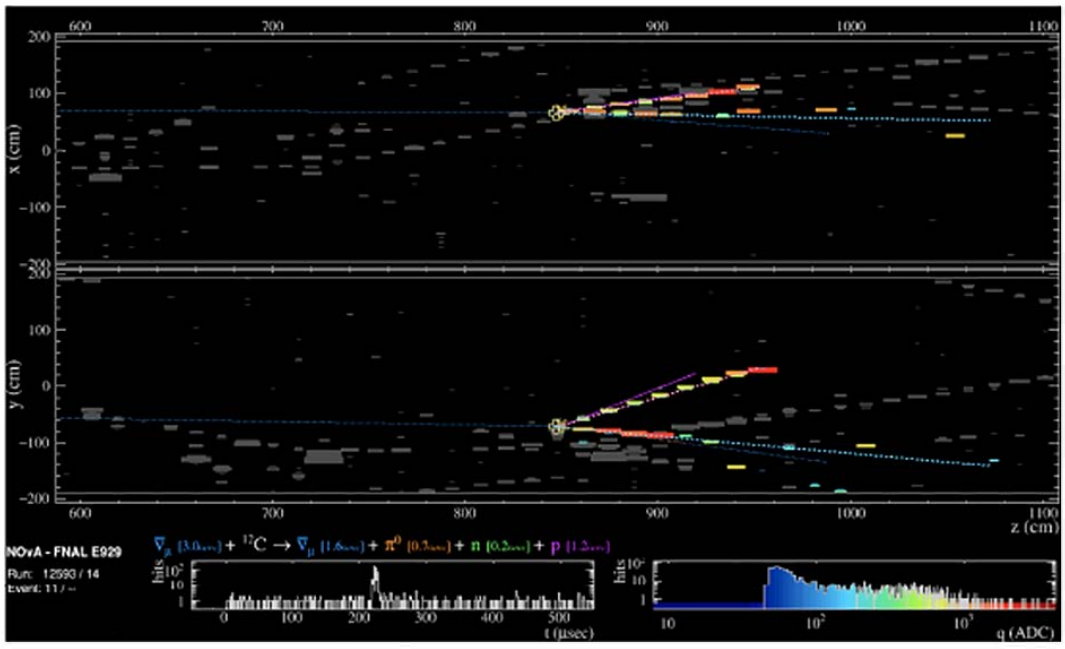

Figure A.2: Anti-muon neutrino neutral current interaction with a π^0 in the final state. One energetic proton in the final state becomes one of the two reconstructed prongs, while the second one corresponds to the two overlapping gammas from the decayed π^0.

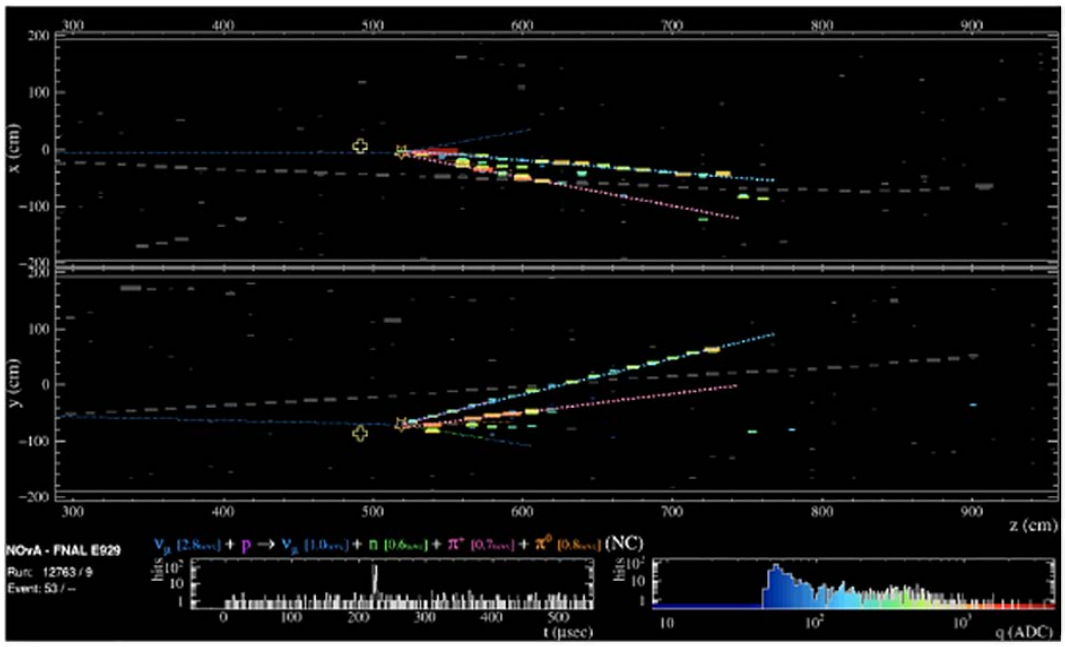

Figure A.3: Muon neutrino neutral current interaction with a π^0 in the final state. One energetic charged pion in the final state becomes one of the two reconstructed prongs, while the second one corresponds to only one of two gammas from the decayed π^0.

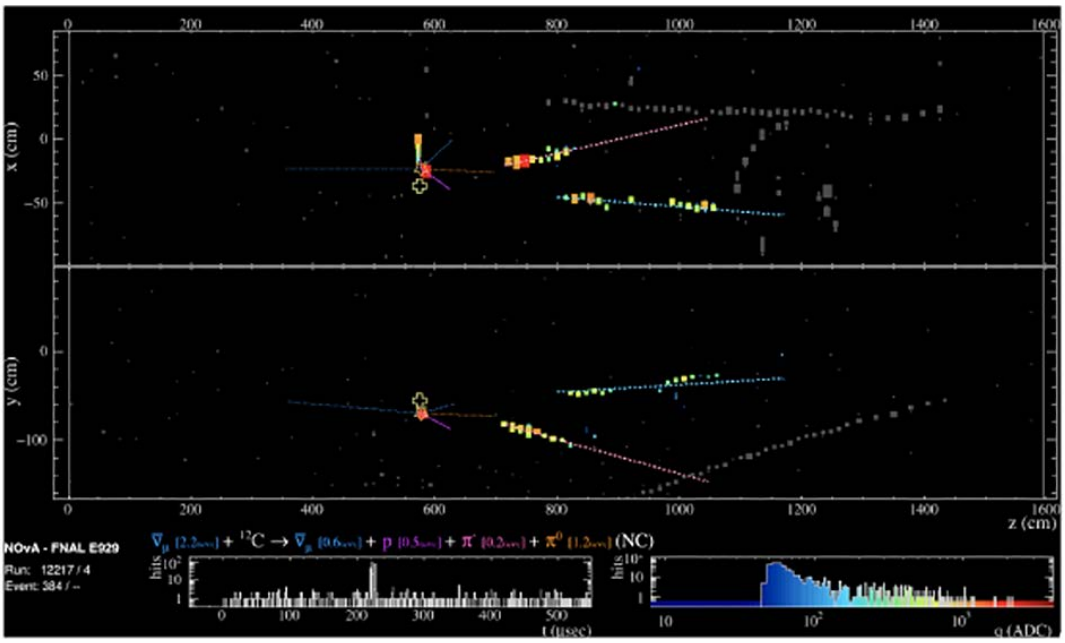

Figure A.4: Anti-muon neutrino neutral current interaction with a π^0 in the final state. A charged pion and a proton are also present in the final state, but their energy deposits are clearly separated from the two reconstructed gamma prongs.

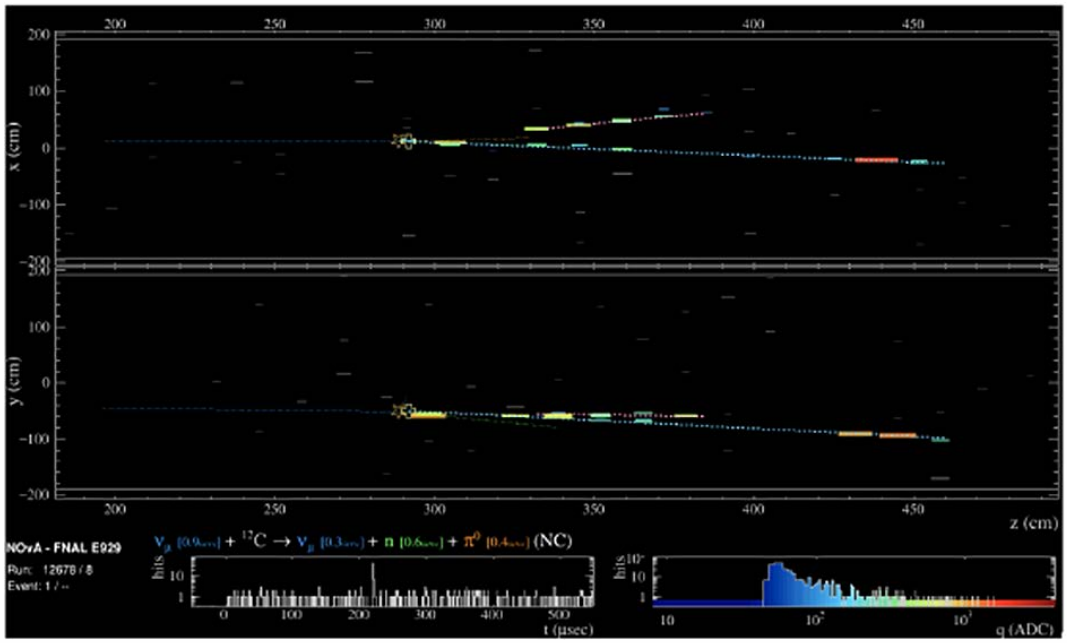

Figure A.5: Muon neutrino neutral current interaction with a π^0 in the final state. A neutron in the final state deposits energy around the interaction vertex and those hits get reconstructed as part of one gamma prong, which will not have a gap but several missing continuous planes.

Appendix B

Monte Carlo Background Event Displays

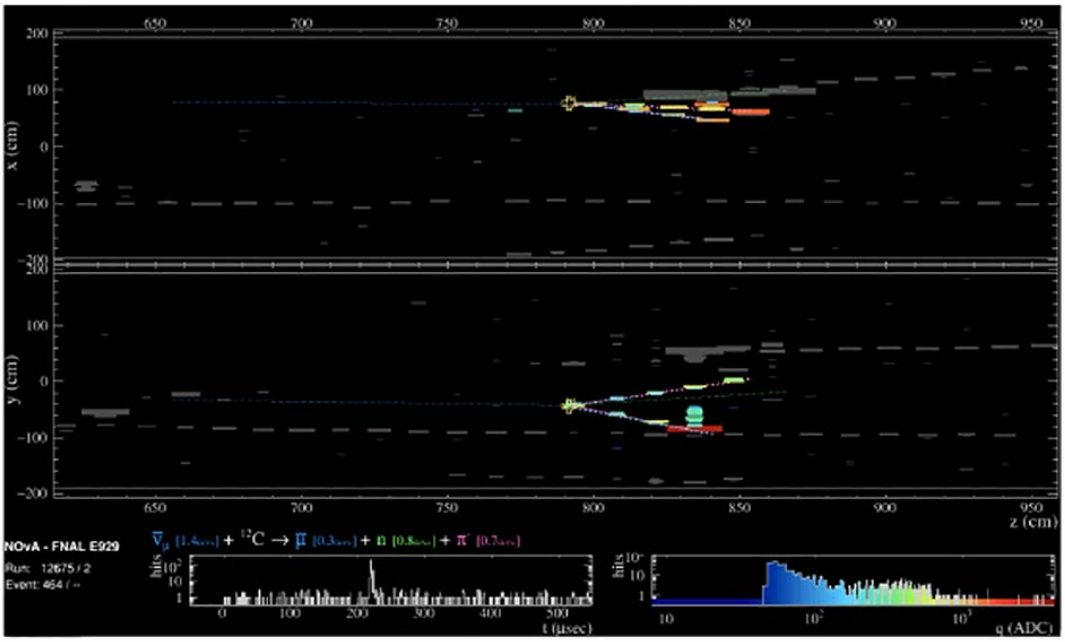

Figure B.1: Anti-muon neutrino charged current interaction without neutral pions in the final state. A low energy muon and a charged pion deposit energy, which gets reconstructed as two prongs.

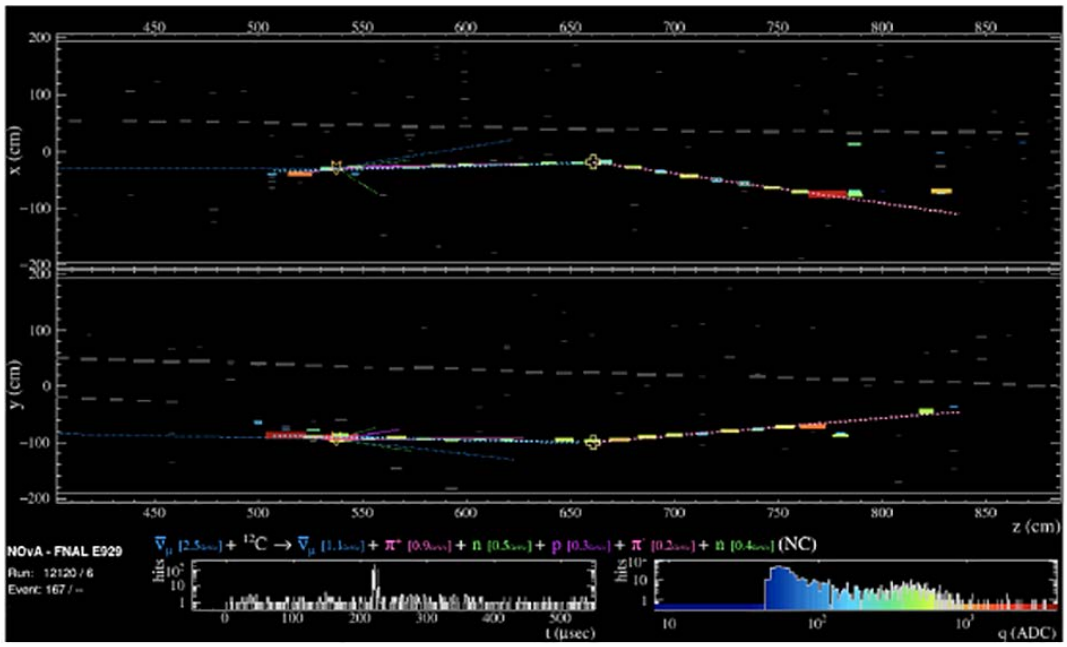

Figure B.2: Anti-muon neutrino neutral current interaction without neutral pions in the final state. An energetic charged pion gets reconstructed as two prongs, because of a kink in its trajectory.

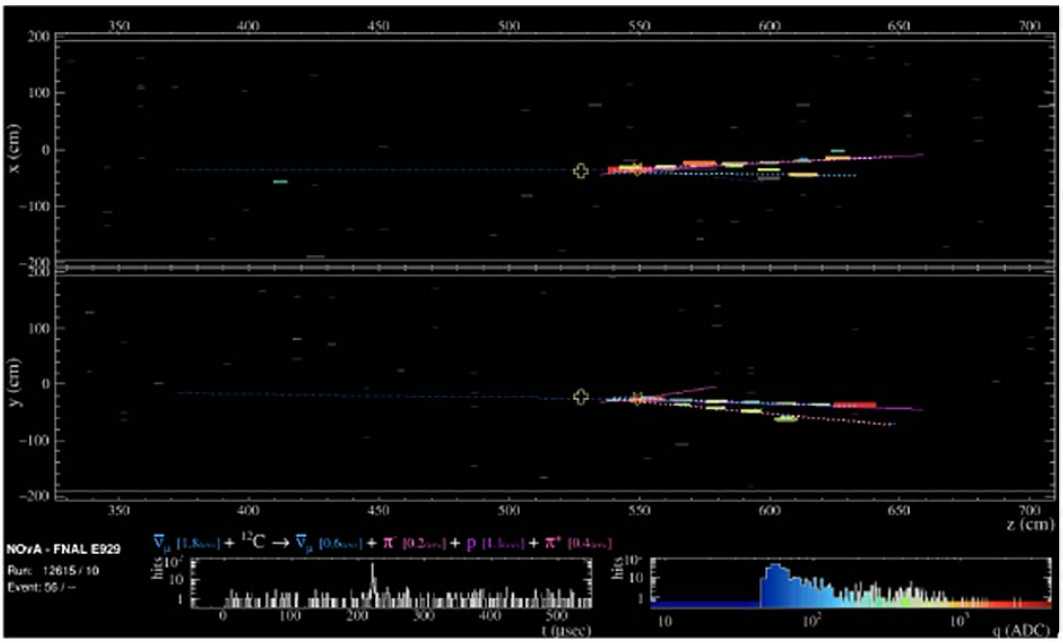

Figure B.3: Anti-muon neutrino neutral current interaction without neutral pions in the final state. A charged pion and proton deposit energy, which gets reconstructed as two prongs.

Appendix C

Cherenkov Counter for NOνA's Test Beam

The Test Beam NOνA detector is a third fairly new detector located in the downstream end of the MC7 enclosure in the Fremilab Testbeam Facility (FTBF), which is a high-energy beam facility at Fermilab devoted to research and development of detectors. FTBF receives 120 GeV protons from the Main Injector during a 4.2 s continuous spill every minute. The primary protons interact in a primary copper target, 100 m upstream of the NOνA Test Beam detector. A second target located in the same MC7 enclosure as the detector generates a tertiary beam, which is collimated, bended and measured along the tertiary beamline. NOνA Test Beam collected data from December 2019 until March 2020 and in the same period in 2020-2021. The detector has 32 vertical and 31 horizontal planes and is considerably smaller than the ND, see fig. C.1.

The NOνA Test Beam effort is crucial to improve the systematic errors through a better understanding of the detector's response to hadronic and electromagnetic showers, scintillation light yield, fiber attenuation, etc. By imaging the interactions of single particles at a known momentum, the Test Beam detector will provide data that allows to enhance the MC simulations

Figure C.1: NOνA Test Beam detector at its location in MC7 from [92].

as well as the event selection algorithms within NOνA.

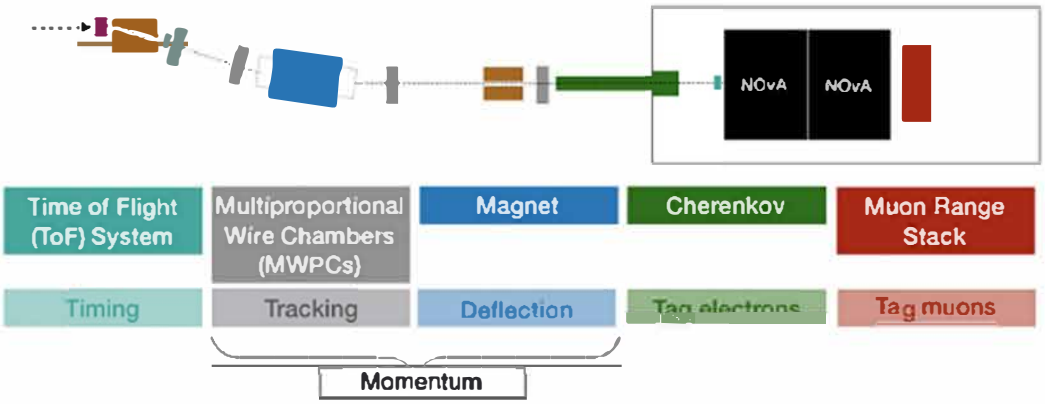

Figure C.2: Schematic of the tertiary beamline.

Figure C.2 shows the tertiary beamline with its different components and their positions. The wire chambers' tracking information combined with the known B-field of the magnet will provide the momentum of individual particles. This and the time of flight data will be the key for particle identification.

The beamline is designed to provide a beam of electrons, muons, pions, protons and kaons with momenta ranging from 0.2-2 GeV/c. From the left image of figure C.3 one can deduce that in this range of momentum, electrons, muons and pions are indistinguishable, and that kaons become indistinguishable from the former at momenta higher than 1 GeV/c. In order to clearly distinguish electrons from all the other particles, Prof. Lang's group at UT Austin built a Cherenkov Counter, which will only see a signal when electrons travel through.

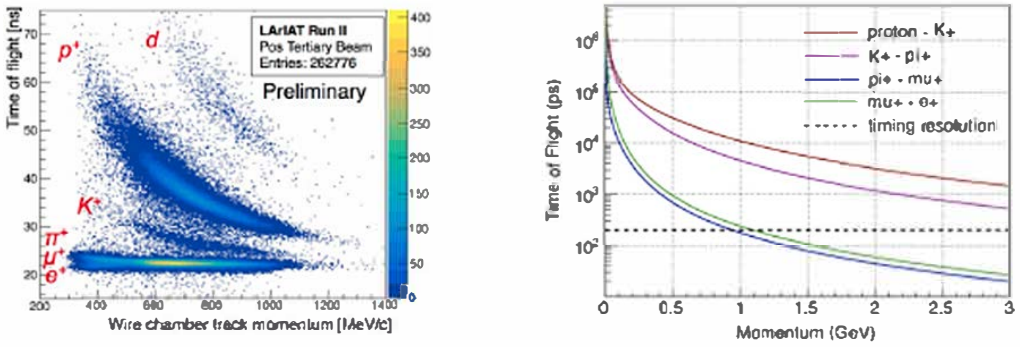

Figure C.3: Particle in time of flight vs momenta plane. Left: Preliminary data from LArIAT Run II [93]. Right: Calculation of relative time of flight for pairwise choice of particles. They become indistinguishable once the graph falls below the threshold (dotted line) [94].

The Cherenkov Counter is filled with gaseous CO_2 at a pressure slightly lower than 1 atm in order to identify electrons because this makes the electron the sole particle capable of emitting Cherenkov radiation, see fig. C.4. Below is the relation between the pressure inside the vessel and the index of refraction:

$$n = kP + 1 \quad \text{where} \quad k = 4.1 * 10^{-4}\ \text{atm}^{-1}.$$

C.1 Reflectance Tests

In order to determine the material for the mirror inside the Cherenkov Counter, reflectance tests were carried out with an UltraScan VIS Spectrophotometer in Fermilab. This instrument, see figure C.5, was used to measure the diffuse and specular or direct reflection of light. There are two possible measurement modes in which you either only measure the diffusive component or both diffuse and direct reflectivity combined. The materials tested were

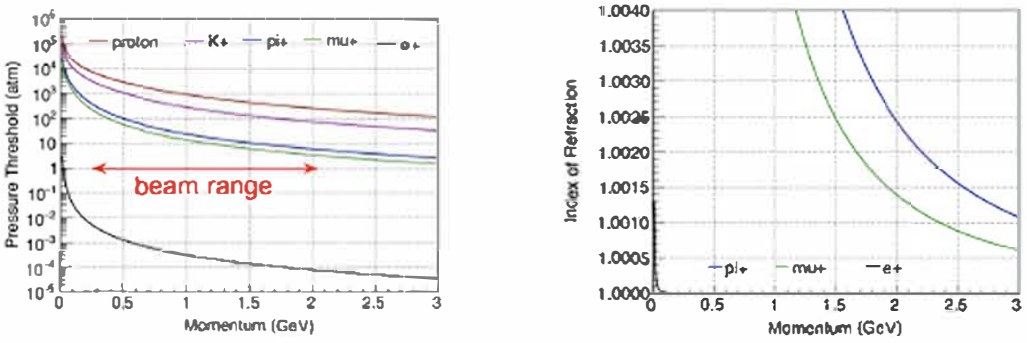

Figure C.4: The threshold determining whether a particle emits Cherenkov radiation in terms of (left) the pressure of CO_2 and (right) the corresponding index of refraction [95].

vinyl, Mylar, a commercial mirror, Reflectech, Vikuity and ESR. Mylar was identified as the most specular reflective material for lower light wavelengths and therefore used for the mirror.

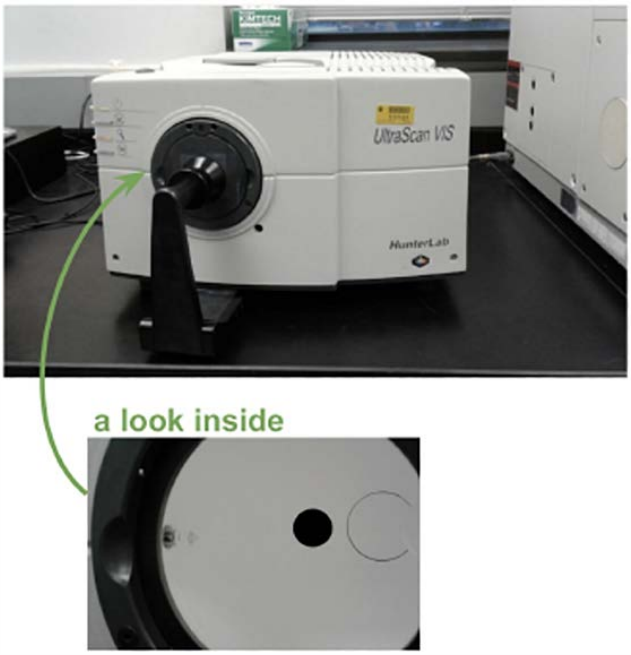

Figure C.5: Picture of the UltraScan VIS Spectrometer used to perform the reflectivity studies.

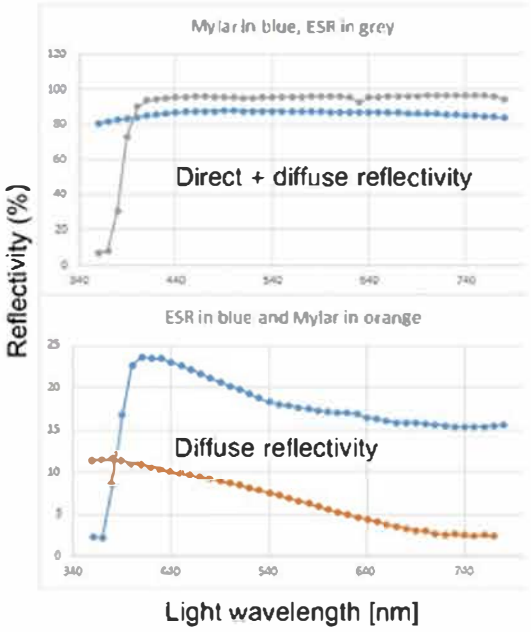

Figure C.6: Reflectance measurements of direct and diffuse reflectivity combined as a function of the light wavelength for ESR and Mylar.

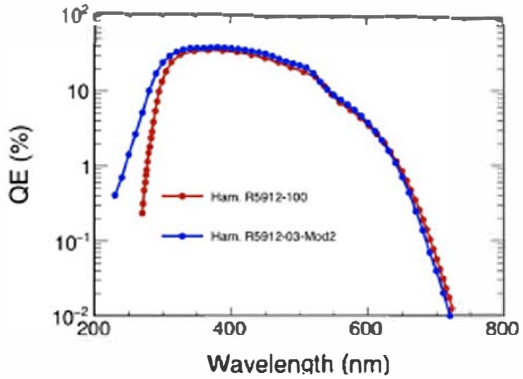

Figure C.7: Quantum efficiency of a commercial Hamamatsu PMT (in red) and the PMT installed at the end of the vertial pipe (in blue).

C.2 The Counter's Mechanical System

The counter consists of two stainless steel pipes connected to an L-shaped structure in which a Mylar mirror focuses the light into a light-tight PMT mounted at the short end of the L, see figures C.8 to C.18. The vertical pipe also contains a Mylar cone to guide the light towards the photon detector. The upstream and downstream windows of the long pipe are sealed to the pipe using flanges and are made out of vinyl, which allows particles to pass through without significant interactions. An additional layer of 44.4 μm Tedlar was added to both upstream and downstream windows to reduce light leaks, since taking data while the lights are turned off inside the MC7 enclosure was more complicated than originally anticipated.

A GEANT4 simulation as well as an analytical calculation was used to obtain the amount of photons detected by the PMT at an index of refraction of n=1.0004. These two methods agreed in the result of 10 photo-electrons (PEs) per meter of travelled distance by the electron.

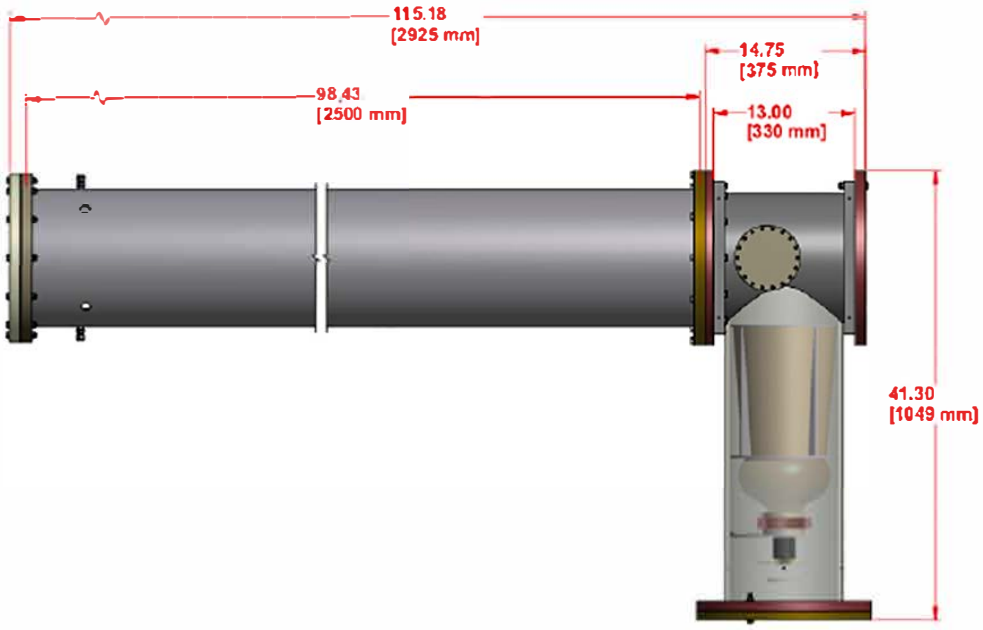

Figure C.8: Schematic of Cherenkov Counter for the NOνA Test Beam [96], drawn by Marek Proga.

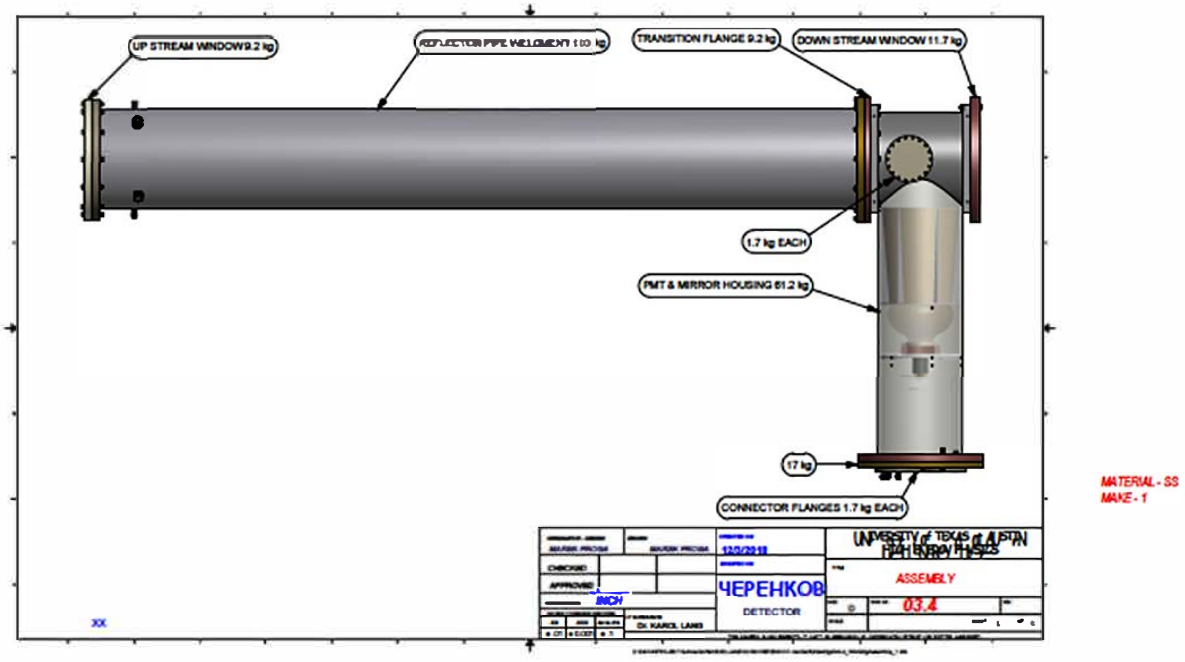

Figure C.9: Schematic of Cherenkov Counter for the NOνA Test Beam [96], drawn by Marek Proga.

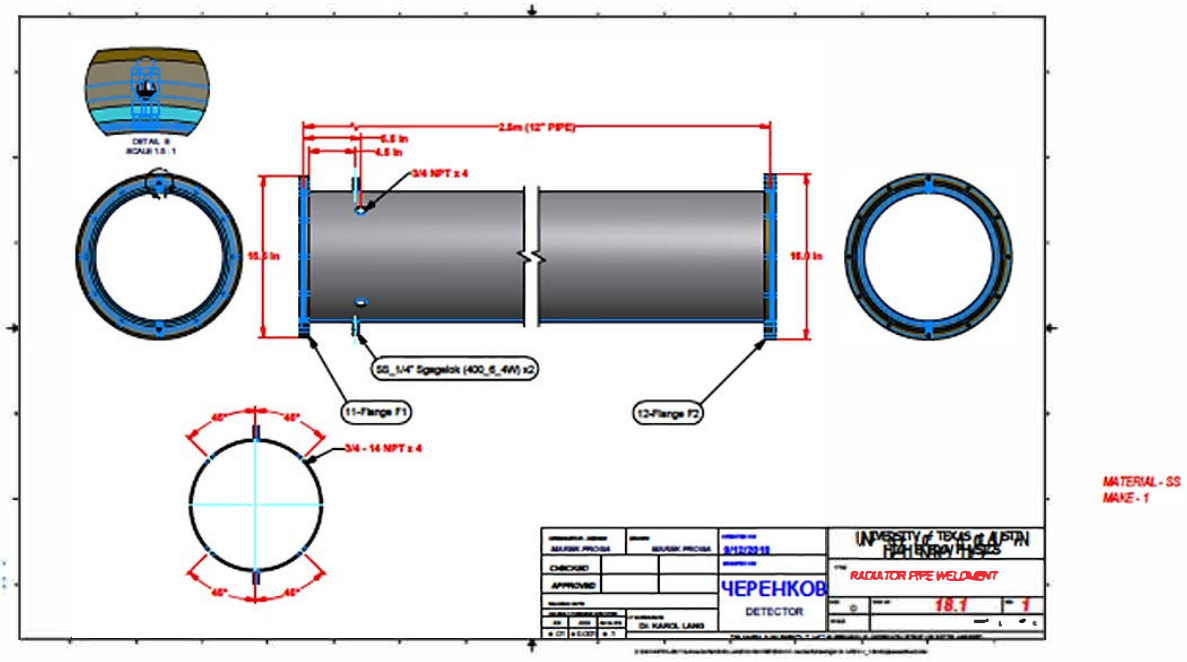

Figure C.10: Schematic of the horizontal pipe with gas connections and NPT holes [96], drawn by Marek Proga.

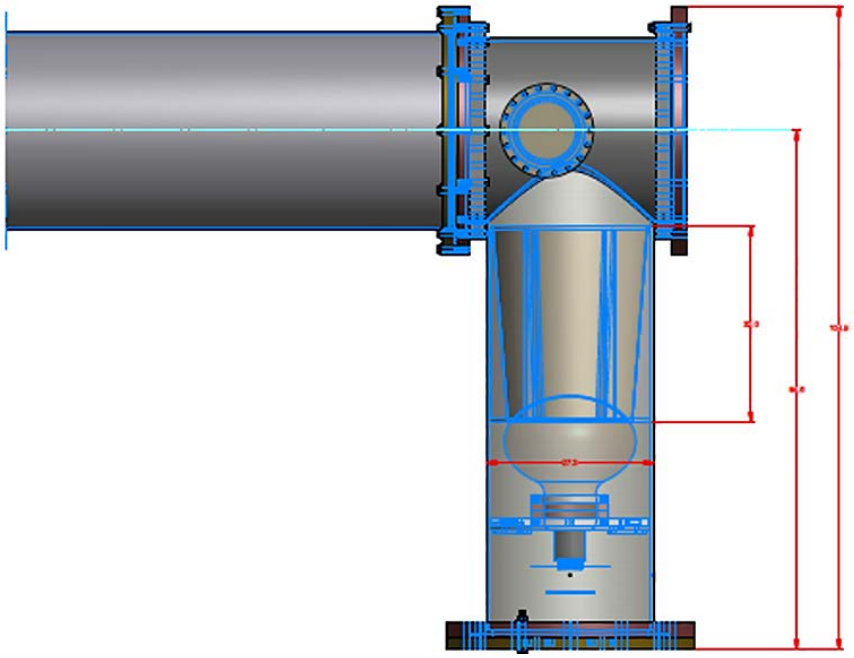

Figure C.11: Schematic of the vertical pipe with cone and PMT [96], drawn by Marek Proga.

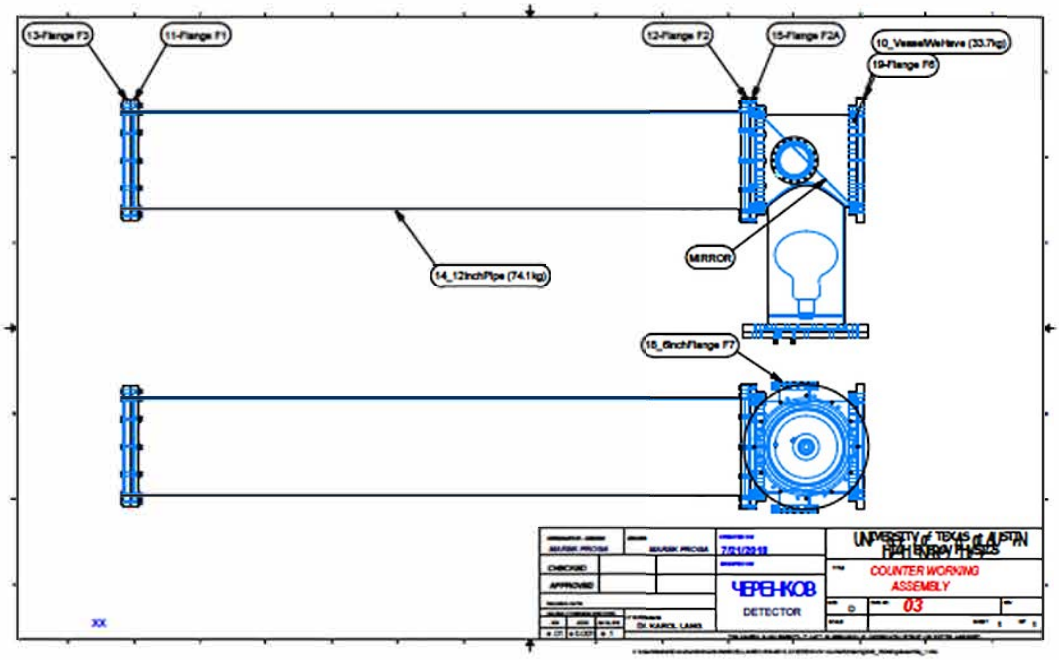

Figure C.12: Schematic of the Cherenkov Counter with weights and mirror position [96], drawn by Marek Proga.

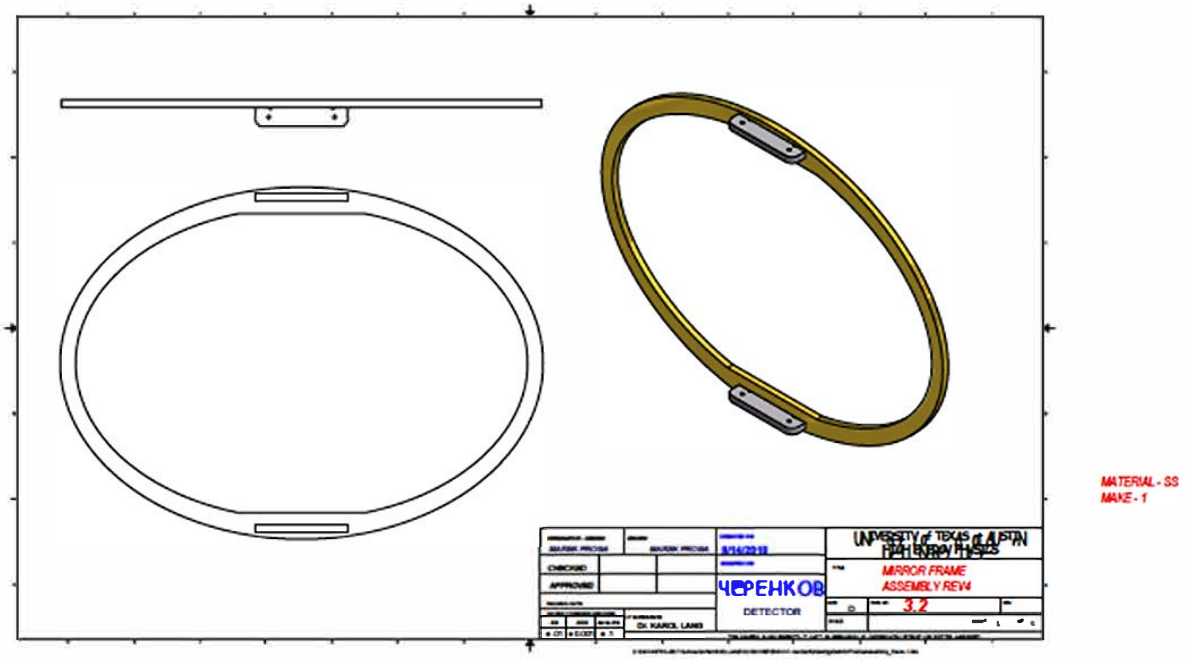

Figure C.13: Schematic of the acrylic frame of the mirror [96], drawn by Marek Proga.

Figure C.14: Pictures of the finalized mirror and cone made out of spanned Mylar foil glued to the frame via stycast. The frames were laser cut and the irregularities on the foil were heat-shrank using a hair dryer.

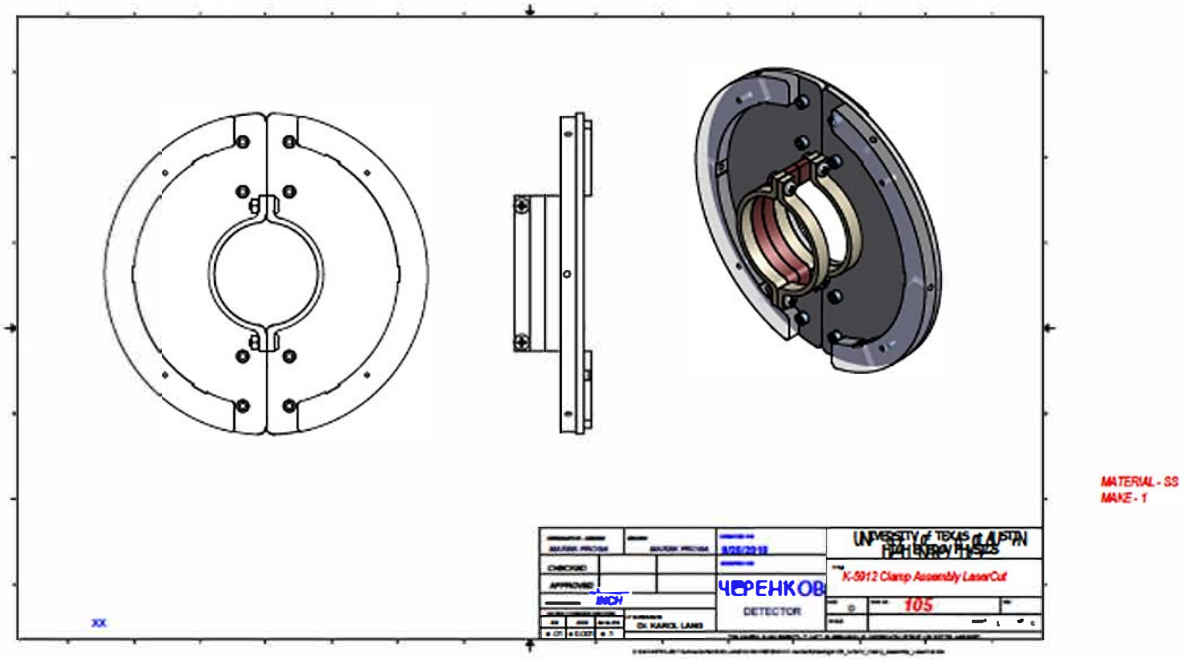

Figure C.15: Schematic of the acrylic PMT mount [96], drawn by Marek Proga. The parts were made using a laser cutter and then assembled.

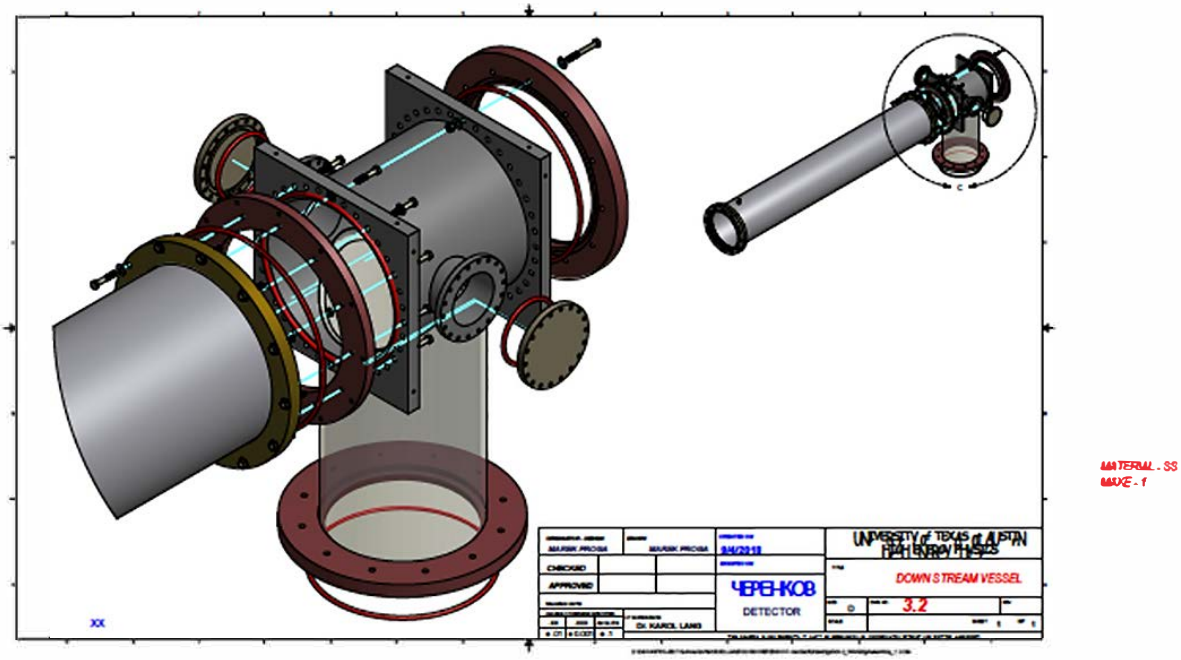

Figure C.16: Schematics of mechanical connection between the horizontal and vertical pipe [96], drawn by Marek Proga.

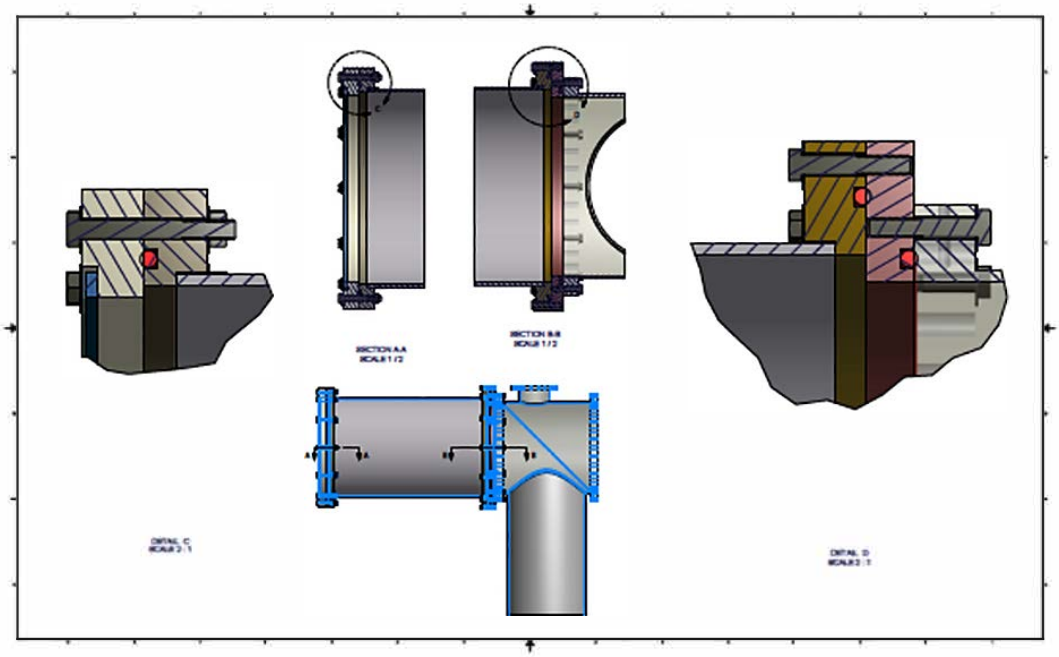

Figure C.17: Schematic of different screws' connections [96], drawn by Marek Proga.

Figure C.18: Left: the horizontal pipe on rails before the installation of the vertical pipe. Right: side view of fully installed Cherenkov Counter.

C.3 The Counter's Electrical System

A high voltage power supply (a Droege, see FERMI: ES-7109) provides -1,600 V through the SHV connection to the PMT. The PMT signal is read out through a BNC connector, which can be seen in figure C.19. The current the PMT draws when operating normally should be under 1 mA (we saw up to 0.28 mA when testing with a pulsed LED at UT Austin).

In order to calibrate the PMT, LED lights will be placed at the start of the horizontal pipe, upstream of the mirror. These LED lights will be pointed at the mirror, so the light reflects off the mirror to the cone, guided by it through further reflections and finally detected by the PMT. The LEDs are mounted using 4 NPT standard caps which were milled to have a half inch

hole to fit in BNC mounts. The BNCs were then attached to the LEDs, then the BNC mounts were potted to the NPT caps with blacked out stycast. At the left most side of figure C.10 the holes where the LEDs will be screwed into can be identified. The LEDs will be powered through a pulse generator with a pulse of 8 ns at an amplitude of 5 V. The LED pulse will be generated simultaneously with a trigger for the PMT. This is done to get the signal from the LEDs in coincidence with the trigger. Once this process is done the LEDs will be disconnected from the pulse generator, but will remain in the Cherenkov pipe. Figure C.20 illustrates the calibration setup.

Figure C.19: Schematics and picture of electrical connections.

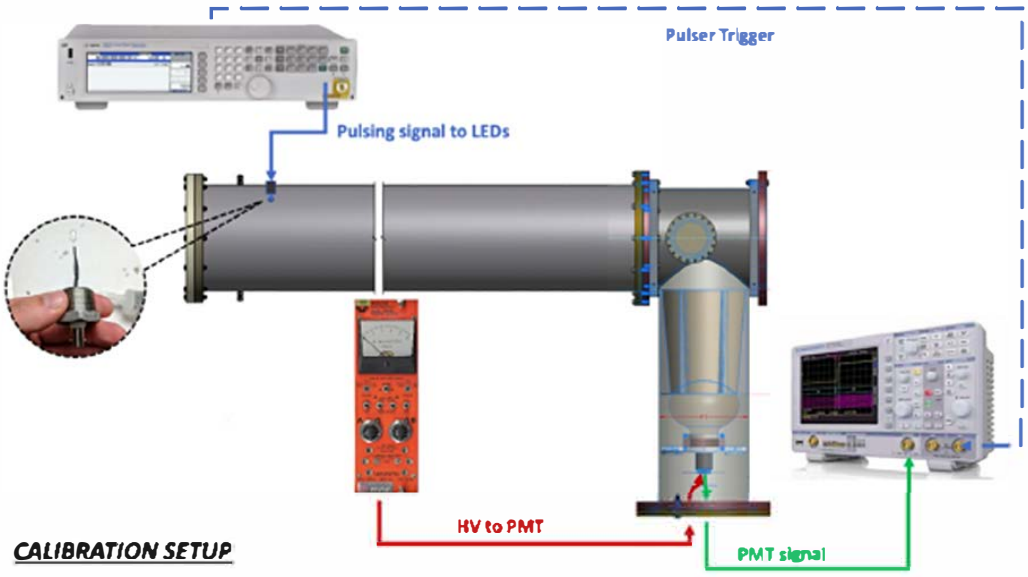

Figure C.20: Electrical circuit for the LEDs.

C.4 The Counter's Gas System

Figure C.21 and C.22 show a schematic and a picture of the gas system, respectively.

The Cherenkov Counter contains about 250 liters of CO_2 that will be kept at about 3-5 mm H_20 above atmospheric pressure. The nominal flow rate of 200 ccm allows a single cylinder to last about 4-5 weeks. For this reason there will only be one cylinder connected to the system at a time, so there is only one bottle regulator associated with the system.

This cylinder will be located to the west of MC7a, in the cylinder storage area formerly used for the MIPP H_2 target gas supply. The bottle regulator is connected to a panel-mounted valve assembly via a flexible braided hose.

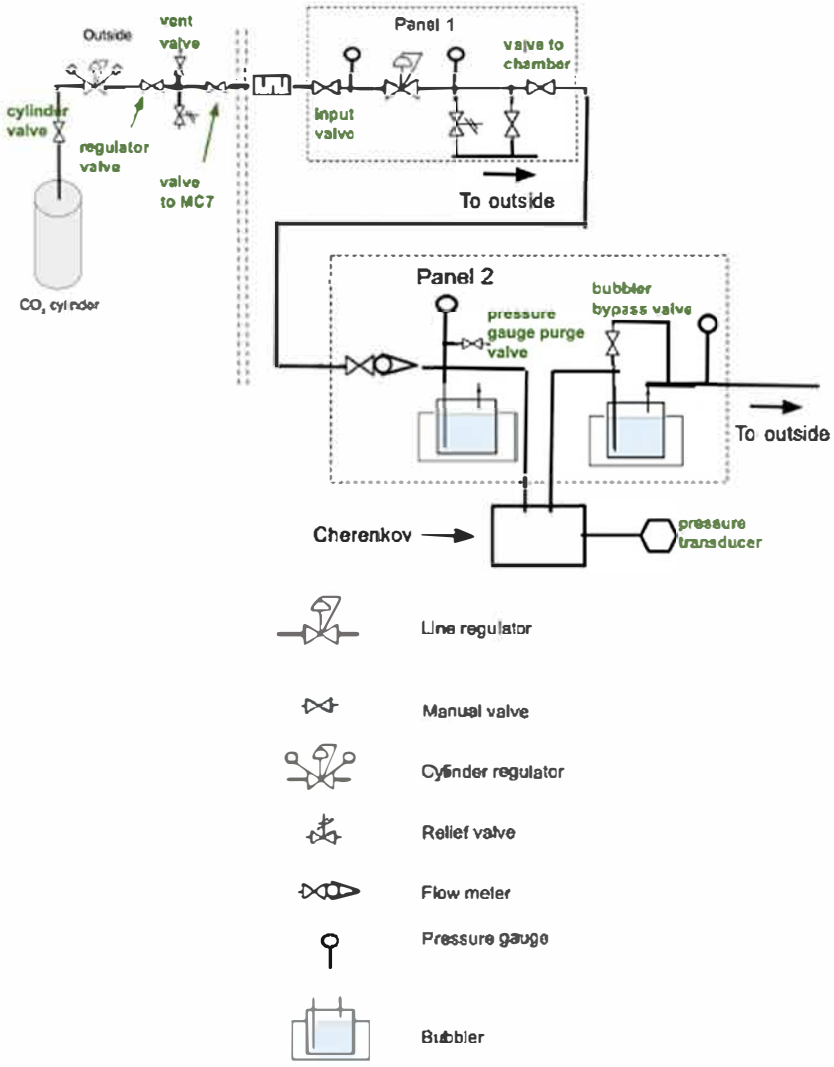

Figure C.21: Gas system schematic.

Figure C.22: Pictures of the cylinder and setup outside MC7 and the gas panels inside the enclosure.

After going through this assembly, which contains 3 valves (vent, isolation, and 50 psi relief), the gas enters MC7a via a 1/4" stainless line. This then connects to a 3/8" blue polyethylene line that runs north to the panels, located on the east wall of MC7b next to the detector. There are 3 panels that contain all the controls for the system, other than what is outside.

A line regulator on the lower Cherenkov panel will bring the nominal 10-15 psi line pressure down to about 1.5 psi before entering the flow meter on the upper panel. A relief valve set to 15 psi is located just after the regulator. There is an input relief bubbler teed off the output of the flow meter (that will limit chamber pressure to less than 2" of water) that is mounted to the back of the middle panel. There are also two precision pressure gauges mounted to the upper panel. One measures chamber pressure via a static pressure line connected directly to the chamber, the other measures exhaust vent pressure - needed to monitor effects of wind gusts, since the system vents outside. The exhaust bubbler is mounted to the front of the upper panel, and there is a bubbler bypass valve that allows for higher flow rates during initial purging of the detector.

There is some likelihood that the counter will need to be moved out of the beam on occasion. In order to maintain the gas purity within the detector during this period, we have installed a sufficiently long gas line so that flow can continue at all times, no matter which position the detector is in. At some point, we may add the ability to monitor the system remotely - either with a camera on the panels, a pressure transducer for the detector, or both.

Bibliography

[1] Zyla, P. A. *et al.* Review of Particle Physics. *PTEP* **2020**, 083C01 (2020).

[2] Funchal, R. Z. *et al.* The physics of neutrinos (2013). 1308.1029.

[3] de Gouvea, A. *et al.* Neutrinos (2013). 1310.4340.

[4] Hernandez, P. Neutrino Physics. In *8th CERN-Latin-American School of High-Energy Physics*, 85–142 (2016). 1708.01046.

[5] Pauli, W. Open letter to the physicists at the gauverein meeting in tubingen (1930).

[6] Fermi, E. Versuch einer Theorie der β-Strahlen. I. *Zeitschrift fur Physik* 88, 161–177 (1934).

[7] Chadwick, J. Possible existence of a neutron (1932). Nature.

[8] Cowan, C. L., Reines, F., Harrison, F. B., Kruse, H. W. & McGuire, A. D. Detection of the free neutrino: a confirmation **124**, 103–104 (1956). URL https://science.sciencemag.org/content/124/3212/103.

[9] Danby, G. *et al.* Observation of high-energy neutrino reactions and the existence of two kinds of neutrinos. *Phys. Rev. Lett.* 9, 36–44 (1962). URL https://link.aps.org/doi/10.1103/PhysRevLett.9.36.

[10] Kodama, K. *et al.* Observation of tau neutrino interactions. *Physics Letters B* **504**, 218–224 (2001). URL https://www.sciencedirect.com/science/article/pii/S0370269301003070.

[11] Glashow, S. L. Partial-symmetries of weak interactions. *Nuclear Physics* **22**, 579–588 (1961). URL https://www.sciencedirect.com/science/article/pii/0029558261904692.

[12] Salam, A. Weak and Electromagnetic Interactions. *Conf. Proc. C* **680519**, 367–377 (1968).

[13] Weinberg, S. A model of leptons. *Phys. Rev. Lett.* **19**, 1264–1266 (1967). URL https://link.aps.org/doi/10.1103/PhysRevLett.19.1264.

[14] Fantini, G., Rosso, A. G., Vissani, F. & Zema, V. The formalism of neutrino oscillations: an introduction (2020). 1802.05781.

[15] Zyla, P. *et al.* Review of Particle Physics. *PTEP* **2020**, 083C01 (2020). And 2021 update.

[16] Stachurska, J. *Astrophysical Tau Neutrinos in IceCube.* Ph.D. thesis, Humboldt U., Berlin, Humboldt U., Berlin (2020).

[17] Nosek, T. Effects of matter in neutrino oscillations and determination of neutrino mass hierarchy at long-baseline experiments (2017). 1612.09132.

[18] Nunokawa, H., Parke, S. & Valle, J. W. Cp violation and neutrino oscillations. *Progress in Particle and Nuclear Physics* **60**, 338?402 (2008). URL http://dx.doi.org/10.1016/j.ppnp.2007.10.001.

[19] Adamson, P. *et al.* Precision Constraints for Three-Flavor Neutrino Oscillations from the Full MINOS+ and MINOS Dataset. *Phys. Rev. Lett.* **125**, 131802 (2020). 2006.15208.

[20] Acero, M. A. *et al.* An Improved Measurement of Neutrino Oscillation Parameters by the NOvA Experiment (2021). 2108.08219.

[21] Abe, K. *et al.* Constraint on the matter–antimatter symmetry-violating phase in neutrino oscillations. *Nature* **580**, 339–344 (2020). [Erratum: Nature 583, E16 (2020)], 1910.03887.

[22] Collaboration, D. The dune far detector interim design report volume 1: Physics, technology and strategies (2018). 1807.10334.

[23] Proto-Collaboration, H.-K. Hyper-kamiokande design report (2018). 1805.04163.

[24] Agostini, M. *et al.* Final Results of GERDA on the Search for Neutrinoless Double-β Decay. *Phys. Rev. Lett.* **125**, 252502 (2020). 2009.06079.

[25] Abgrall, N. *et al.* The large enriched germanium experiment for neutrinoless double beta decay (legend) (2017). URL http://dx.doi.org/10.1063/1.5007652.

[26] Gando, Y. First results of KamLAND-Zen 800. *J. Phys. Conf. Ser.* **1468**, 012142 (2020).

[27] Aker, M. e. a. Improved upper limit on the neutrino mass from a direct kinematic method by katrin. *Physical Review Letters* **123** (2019). URL http://dx.doi.org/10.1103/PhysRevLett.123.221802.

[28] Ashtari Esfahani, A. *et al.* Determining the neutrino mass with cyclotron radiation emission spectroscopy—Project 8. *J. Phys. G* **44**, 054004 (2017). 1703.02037.

[29] Formaggio, J. A. & Zeller, G. P. From ev to eev: Neutrino cross sections across energy scales. *Rev. Mod. Phys.* **84**, 1307–1341 (2012). URL https://link.aps.org/doi/10.1103/RevModPhys.84.1307.

[30] Simo, I. R. *et al.* Relativistic model of 2p-2h meson exchange currents in (anti)neutrino scattering. *Journal of Physics G: Nuclear and Particle Physics* **44**, 065105 (2017). URL https://doi.org/10.1088%2F1361-6471%2Faa6a06.

[31] Mosel, U. Neutrino interactions with nucleons and nuclei: Importance for long-baseline experiments. *Annual Review of Nuclear and Particle Science* **66**, 171–195 (2016).

[32] Lu, X.-G. *et al.* Exploring neutrino-nucleus interactions in the GeV regime using MINERvA. *The European Physical Journal Special Top-*

ics **230**, 4243–4257 (2021). URL https://doi.org/10.1140%2Fepjs%2Fs11734-021-00296-6.

[33] Acero, M. A. *et al.* Adjusting neutrino interaction models and evaluating uncertainties using NOvA near detector data. *Eur. Phys. J. C* **80**, 1119 (2020). 2006.08727.

[34] Deka, P. & Bora, K. Impact of Multi-Nucleon Effects on Neutrino Scattering Cross Section and Events at Near and Far Detectors of NOνA Experiment. *Springer Proc. Phys.* **265**, 147–152 (2022).

[35] Olson, T. G. *Measurement of $d^2\sigma/d|\vec{q}|dE_{avail}$ and 2p2h contribution using charged current ν_μ interactions in the NOvA Near Detector.* Ph.D. thesis, Tufts U., Tufts U. (2021).

[36] Tripathi, J. *Charged Pion semi inclusive charged current cross section measurement in the NOvA experiment at Fermiilab.* Ph.D. thesis, Panjab U. (2020).

[37] Kalra, D. *A measurement of neutrino induced neutral current Neutral pion production cross section with the nova Near detector.* Ph.D. thesis, Panjab U. (2019).

[38] Services, F. C. Gallery. https://vms.fnal.gov/index/vms-home (2021).

[39] Edayath, S. *et al.* Sterile Neutrino Search in the NOvA Far Detector. In *Meeting of the APS Division of Particles and Fields* (2017). 1710.01280.

[40] Acero, M. A. *et al.* Search for slow magnetic monopoles with the NOvA detector on the surface. *Phys. Rev. D* **103**, 012007 (2021). 2009.04867.

[41] Phan, D. D. *A search for neutron-antineutron oscillation in the NOvA experiment.* Ph.D. thesis, Texas U., Texas U. (2020).

[42] Acero, M. A. *et al.* Supernova neutrino detection in NOvA. *JCAP* **10**, 014 (2020). 2005.07155.

[43] Acero, M. A. *et al.* Search for multimessenger signals in NOvA coincident with LIGO/Virgo detections. *Phys. Rev. D* **101**, 112006 (2020). 2001.07240.

[44] Acero, M. A. *et al.* Measurement of neutrino-induced neutral-current coherent π^0 production in the NOvA near detector. *Phys. Rev. D* **102**, 012004 (2020). 1902.00558.

[45] Behera, B. Measurement of the Inclusive Muon Neutrino Charged-Current Cross-Section in the NOvA Near Detector. *Springer Proc. Phys.* **234**, 329–333 (2019).

[46] Kalra, D. Current Status for the Inclusive Neutral Current π^0 Production Cross-Section Measurement with the NOvA Near Detector. (2019).

[47] Ambats, I. *et al.* The MINOS Detectors Technical Design Report (1998).

[48] Adamson, P. *et al.* The NuMI Neutrino Beam. *Nucl. Instrum. Meth. A* **806**, 279–306 (2016). 1507.06690.

[49] Ayres, D. S. *et al.* The NOvA Technical Design Report (2007).

[50] Soplin, L. A. Ppfx technote for the 2017 analysis. Tech. Rep. NOVA-doc-23441.

[51] Acero, M. A. *et al.* New constraints on oscillation parameters from ν_e appearance and ν_μ disappearance in the nova experiment. *Phys. Rev. D* **98**, 032012 (2018). URL https://link.aps.org/doi/10.1103/PhysRevD.98.032012.

[52] Psihas, F. Event displays for nue selected events. Tech. Rep. NOVA-doc-15647.

[53] Mufson, S. & et al. Liquid scintillator production for the nova experiment. *Nuclear Instruments and Methods in Physics Research Section A: Accelerators, Spectrometers, Detectors and Associated Equipment* **799**, 1–9 (2015). URL http://dx.doi.org/10.1016/j.nima.2015.07.026.

[54] Mualem, L. M. Apd overview. Tech. Rep. NOVA-doc-14143.

[55] Kasahara, S. M. NOvA data acquisition system. *Physics Procedia* **37**, 1876–1883 (2012). URL https://doi.org/10.1016%2Fj.phpro.2012.02.511.

[56] Pershey, D. S. *A Measurement of ν_e Appearance and $\bar{\nu}_\mu$ Disappearance Neutrino Oscillations with the NOvA Experiment.* Ph.D. thesis, Caltech (2018).

[57] et al., A. N. Performance of the nova data acquisition and trigger systems for the full 14 kt far detector. *Journal of Physics: Conference Series* 664, 082041 (2015). URL https://iopscience.iop.org/article/10.1088/1742-6596/664/8/082041.

[58] Campanella, M., Ferrari, A., Sala, P. R. & Vanini, S. First Calorimeter Simulation with the FLUGG Prototype (1999).

[59] Böhlen, T. *et al.* The fluka code: Developments and challenges for high energy and medical applications. *Nuclear Data Sheets* 120, 211–214 (2014). URL https://www.sciencedirect.com/science/article/pii/S0090375214005018.

[60] Ferrari, A. *et al.* Fluka: A multi-particle transport code (2005). URL https://www.osti.gov/biblio/877507.

[61] Agostinelli, S. *et al.* Geant4 simulation toolkit. *Nuclear Instruments and Methods in Physics Research Section A: Accelerators, Spectrometers, Detectors and Associated Equipment* 506, 250–303 (2003). URL https://www.sciencedirect.com/science/article/pii/S0168900203013688.

[62] Aliaga, L. *et al.* Neutrino flux predictions for the numi beam. *Phys. Rev. D* 94, 092005 (2016). URL https://link.aps.org/doi/10.1103/PhysRevD.94.092005.

[63] Aurisano, A. *et al.* The NOvA simulation chain. *J. Phys. Conf. Ser.* 664, 072002 (2015).

[64] et al., A. The genie neutrino monte carlo generator. *Nuclear Instruments and Methods in Physics Research Section A: Accelerators, Spectrometers, Detectors and Associated Equipment* **614**, 87?104 (2010). URL http://dx.doi.org/10.1016/j.nima.2009.12.009.

[65] Hagmann, C., Lange, D. & Wright, D. Cosmic-ray shower generator (cry) for monte carlo transport codes. vol. 2, 1143 – 1146 (2007).

[66] Aurisano, A. A description of the light model that includes cherenkov light. Tech. Rep. NOVA-doc-23228 (2017).

[67] Brun, R. & Rademakers, F. Root - an object oriented data analysis framework. *Nuclear Instruments and Methods in Physics Research Section A: Accelerators, Spectrometers, Detectors and Associated Equipment* **389**, 81–86 (1997). URL https://www.sciencedirect.com/science/article/pii/S016890029700048X. New Computing Techniques in Physics Research V.

[68] Behera, B. *et al.* Dpf proceeding: Event reconstruction in the nova experiment. Tech. Rep. NOVA-doc-23813.

[69] Baird, M. *et al.* Summary of new and retuned reconstruction and pid modules in production 5. Tech. Rep. NOVA-doc-43162.

[70] Baird, M. *et al.* Event reconstruction techniques in NOvA. *Journal of Physics: Conference Series* **664**, 072035 (2015). URL https://doi.org/10.1088/1742-6596/664/7/072035.

[71] Pershey, D. *et al.* Tdslicer technote. Tech. Rep. NOVA-doc-27689.

[72] Prim, R. C. Shortest connection networks and some generalizations. *Bell System Technical Journal* **36**, 1389–1401 (1957). URL https://onlinelibrary.wiley.com/doi/abs/10.1002/j.1538-7305.1957.tb01515.x. https://onlinelibrary.wiley.com/doi/pdf/10.1002/j.1538-7305.1957.tb01515.x.

[73] Fernandes, L. A. & Oliveira, M. M. Real-time line detection through an improved hough transform voting scheme. *Pattern Recognition* **41**, 299–314 (2008). URL https://www.sciencedirect.com/science/article/pii/S0031320307001823.

[74] Baird, M. D. Tech note for the multi-hough transform. Tech. Rep. NOVA-doc-8241.

[75] Ohlsson, M. Extensions and explorations of the elastic arms algorithm. *Computer Physics Communications* **77**, 19–32 (1993). URL https://www.sciencedirect.com/science/article/pii/0010465593900339.

[76] Yang, M.-S. & Wu, K.-L. Unsupervised possibilistic clustering. *Pattern Recogn.* 39, 521 (2006). URL https://doi.org/10.1016/j.patcog.2005.07.005.

[77] Krishnapuram, R. & Keller, J. M. A possibilistic approach to clustering. *IEEE Transactions on Fuzzy Systems* 1, 98–110 (1993).

[78] Raddatz, N. J. Kalmantrack technical note. Tech. Rep. NOVA-doc-13545.

[79] Rebel, B. Window tracking algorithm for cosmic ray muons. Tech. Rep. NOVA-doc-15977.

[80] Alion, T. Calibration technotes. Tech. Rep. NOVA-doc-13579.

[81] Collaboration, N. NOvA Official Plots Database. https://nusoft.fnal.gov/nova/blessedplots (2021).

[82] Harris, D. Overview of Neutrino-Nucleus Interactions. https://indico.cern.ch/event/835190/contributions/3576882/attachments/1940878/3218672/NNN19_Harris_v4.pdf (2019).

[83] Aguilar-Arevalo *et al.* Measurement of ν_μ and $\overline{\nu}_\mu$ induced neutral current single π^0 production cross sections on mineral oil at $E_\nu \sim$ ● (1 gev). *Phys. Rev. D* 81, 013005 (2010). URL https://link.aps.org/doi/10.1103/PhysRevD.81.013005.

[84] Abratenko, P. *et al.* Measurement of neutral current single π^0 production on argon with the MicroBooNE detector (2022). 2205.07943.

[85] Pickard, L. J. *Neutrino induced neutral current single π^0 production at the near detector of the T2K experiment.* Ph.D. thesis, University of Sheffield (2016).

[86] Doyle, D. D. *et al.* Derivation of the relative cross-sectionuncertainty figure of merit for selection criteria cross section analyses. Tech. Rep. NOVA-doc-49166.

[87] Cedeno, A. J. *Semi-inclusive Neutral Current Neutral Pion Production Selection at the NOvA (NuMI Off-axis Electron Neutrino Appearance) Near Detector Using Prong Level Convolutional Neural Networks.* Master's thesis, Wichita State U. (2018).

[88] Doyle, D. D. Identifying final state particles in the nova detectors with cnn. Tech. Rep. NOVA-doc-44920.

[89] Cremonesi, L. *et al.* Summary of single particle cvn training for prod5.1. Tech. Rep. NOVA-doc-51176-v1.

[90] Hoecker, A. *et al.* Tmva - toolkit for multivariate data analysis (2007). URL `https://arxiv.org/abs/physics/0703039`.

[91] Kuruppu, C. Determining vertex activity in noνa. Tech. Rep. NOVA-doc-47585-v1.

[92] Collaboration, N. NOvA Test Beam Wiki. `https://cdcvs.fnal.gov/redmine/projects/novatestbeam/wiki` (2019).

[93] Sousa, A. Noνa test beam plenary summary - 2018 austin collaboration meeting. Tech. Rep. NOVA-doc-27134.

[94] Huang, J. Test beam: Simulating the new beam line setup. Tech. Rep. NOVA-doc-27644.

[95] Huang, J. *et al.* Test beam: Estimation of photon count of a cherenkov counter. Tech. Rep. NOVA-doc-27446.

[96] Proga, M. Cherenkov counter. Tech. Rep. UTKL-doc-2060-v2, 2102-v1 and 2098-v1.

Vita

Beatriz Tapia Oregui was born in , , on .

She received Bachelor of Science and Master of Science degrees in Physics from the University of Heidelberg in Germany in 2011 and 2015, respectively. The academic year of 2012-2013 she attended courses at the University of Durham, UK, thanks to the Erasmus Exchange Program. After her Masters she did an internship at Robert Bosch GmbH's Automotive Electronics Division at Kusterdingen, Germany. She started the Physics Ph.D. program at the University of Texas at Austin in August, 2016.

Permanent address:

This dissertation was typeset with LaTeX† by the author.

†LaTeX is a document preparation system developed by Leslie Lamport as a special version of Donald Knuth's TeX Program.